A DAMAGE-BASED TIME-DOMAIN WEAR-OUT MODEL FOR WIRE BOND INTERCONNECTS IN POWER ELECTRONIC MODULE

LI YANG

Thesis submitted to the University of Nottingham

For the degree of Doctor of Philosophy

Department of Electrical and Electronic Engineering

The University of Nottingham

May 2013

ABSTRACT

In the Physics-of-Failure based approach to reliability design and assessment, which aims to relate lifetime to the identified root-cause of the potential failures, the development of effective failure mechanism models is a crucial task.

The extent and rate of wire bond degradation depends on both the magnitude and duration of exposure to the loads. In the existing physics-of-failure models for wire bond interconnects, lifetime is accounted for by loading amplitude alone and is usually derived based on a regular thermal cycle of a known duration. They are not ready to predict life of arbitrary mission profiles and the effects of time at temperature on the wear-out behaviour are not addressed, leading to substantial errors for thermal cycling regimes with high peak temperatures.

In this thesis, a new lifetime prediction model for wire bonds is proposed based on some phenomenological considerations, which accounts not only for the damage accumulation processes but also the damage removal phenomena during thermal exposure. The methodology discards the usual cycle-dependent modelling methodology and is instead based on a time domain representation so that it can more accurately reflect the observed temperature-time effects and related phenomena.

This new time-based presentation allows estimation on the bonding interface damage condition at regular time intervals through a damage based crack propagation model which includes the effect of temperature and time dependent material properties. Meanwhile, bond degradation state is indicated in the form of crack growth and shear force reduction that are predicted by the total interface damage as a function of time. The model is calibrated and validated by the experimental results from wire material characterization tests and accelerated thermal cycling which demonstrates the advantages over the cycle-based methodologies.

ACKNOWLEDMENTS

In order for a project of this multi-disciplinary nature to reach a successful conclusion, the input of many people is required and consequently, in this small space it is difficult to do everybody justice.

The first thank you is given to my supervisor Prof. Mark Johnson for offering me the opportunity to study for a PhD and for his insightful ideas, academic guidance, as well as the help in my personal welfare throughout the course of my study at the University of Nottingham. It is impossible for me to hold on to the end without his support. I would also like to extend appreciations to my second supervisor Prof. Greg Asher for his input.

The packaging lab has been a very enjoyable place to work during my time at Nottingham, and so thanks are due to everyone else in the group for the help and support. I would like to express my special acknowledgements to Dr. Pearl Agyakwa for providing valuable technical suggestions and excellent work concerning material characterization on wire bond samples and Dr. Martin Corfield for assistance with tuning the environmental chambers.

I am grateful to Dynex Ltd. for providing wire bond samples and conducting accelerated tests, also to Prof. Li Ran in Durham University for allowing me to use the equipments for my experiment and the kind help in sorting out accommodations during my stay in Durham.

Finally, thank you to my family for their love, support and encouragement over the years, especially to my daughter who has been a little accompany for me and has always been tolerant of my negligence. The days we spent together in Durham when I did my experiment will be in my memories forever.

The last corner is reserved for the special person Prof. Alan Jack, who is the beacon lighting up my way. It's a great honour to make the acquaintance of him in my life.

CONTENTS

LIST OF FIGURES

LIST OF TABLES

LIST OF ABBREVIATIONS

AMB	active metal brazing
CTE	coefficient of thermal expansion
DBC	direct bonded copper
EBSD	electron backscatter diffraction
f.c.c	face-centred cubic
FEA	finite element analysis
FIB	focused ion beam
IGBT	insulated-gate bipolar transistor
IMC	intermetallic compound
MIL-HDBK	military handbook
MTBF	mean time between failures
MOSFET	metal oxide semiconductor field effect transistor
PHM	prognostics and health management
PoF	physics of failure

CHAPTER 1

INTRODUCTION

1.1 STRUCTURE OF THE THESIS

Chapter 1: Introduction

An introduction is given to the role of Physics-of-failure modelling in the reliability design and assessment for power semiconductor modules. The primary shortcomings of the existing PoF based lifetime prediction models for wire bond interconnects are discussed which motivates the proposal of a novel time-domain model. The plan of the model implementation, calibration and validation is briefly presented as well.

Chapter 2: Physics-of-Failure Approach to Reliability Assessment for Power Electronic Modules

The assembly structure and main packaging materials for typical power modules are described in detail. Dominant failure modes and mechanisms in a power module are analyzed, and discussed in relation to subsequent reliability issues.

This chapter also introduces the evolution of reliability assessment methodologies, including the transition from traditional failure rate prediction

to physics-of-failure approach and then prognostics and health management for power modules based on PoF models.

Chapter 3: Physics-of-Failure Models for Wire Bond Interconnects

In this chapter, the procedures for deriving physics-of-failure models are briefly introduced.

A literature review of the commonly adopted physics-of-failure lifetime prediction models for wire bond interconnects is presented and the limitations to these commonly adopted models are discussed in detail.

Chapter 4: A Time-Domain Damage Based Crack Propagation Model

A new time-domain damage based crack propagation model is proposed for the lifetime prediction of wire bonds. The details of the model development and implementation are provided in this chapter.

Chapter 5: Model Verification and Calibration

In this chapter, the damage model is calibrated by quantitatively linking damage parameters to physical material deformation indicators i.e. plastic strain energy, which is derived from uniaxial tensile tests under a variety of loading conditions. Subsequent model parameters are justified by bond shear force degradation data under extended thermal cycling tests.

Chapter 6: Simulation of Bond Wear-out Performance and Lifetime Predictions

In this chapter, the development of damage and shear force degradation rate are predicted by operating the calibrated model under a variety of loading

temperatures. Simulation results corresponding to the designed temperature profiles are illustrated.

Chapter 7: Model Validation by Accelerated Tests

This chapter introduces accelerated tests usually used for reliability prediction and qualification assessment. Intention and design of the passive thermal cycling and active power cycling for the collection of the lifetime data are described. Experimental results are presented and discussed. Shear degradation rate is also predicted via the damage based crack propagation model. Model validation is then accomplished through the comparison between simulation and experimental results.

Chapter 8: Conclusion and Future Work

This chapter summarizes the experimental work covered in this thesis and suggests future work.

1.2 OVERVIEW AND MOTIVATIONS

Power electronics is an enabling technology for electrical power conversion and control throughout the energy supply chain. It delivers control and modification of voltage, current and frequency output from any electrical power input and consequently has extensive applications from small self-contained converters used for providing local power supplies in electronic systems through to large-scale installations capable of controlling the flow of power between continents [1].

The application of power electronics technology offers a huge range of benefits, some related to performance, others to economy [2]. For example, in the transport sector, electric and hybrid electric vehicles that are gaining an increasing market share are only possible with efficient and intelligent power electronics [3]. Its application in power supplies, motor drives, lighting and domestic appliances helps improve overall efficiency and reduce energy consumption. And in aerospace applications, weight savings through power electronics will reduce fuel to weight ratio over a typical flight cycle.

In more recent times, green energy revolution has been strongly advocated in order to guarantee energy security and protect the environment for future generations [4]. Low carbon energy generation technologies such as large-scale wind turbines and photovoltaic based solar panels are becoming the dominant form of energy generation. In all of these low-carbon energy systems, power electronics play a key role as an interface of integrating renewable energy sources into the existing electrical network. Figure 1.1 shows a schematic drawing of a power electronic enabled renewable energy system.

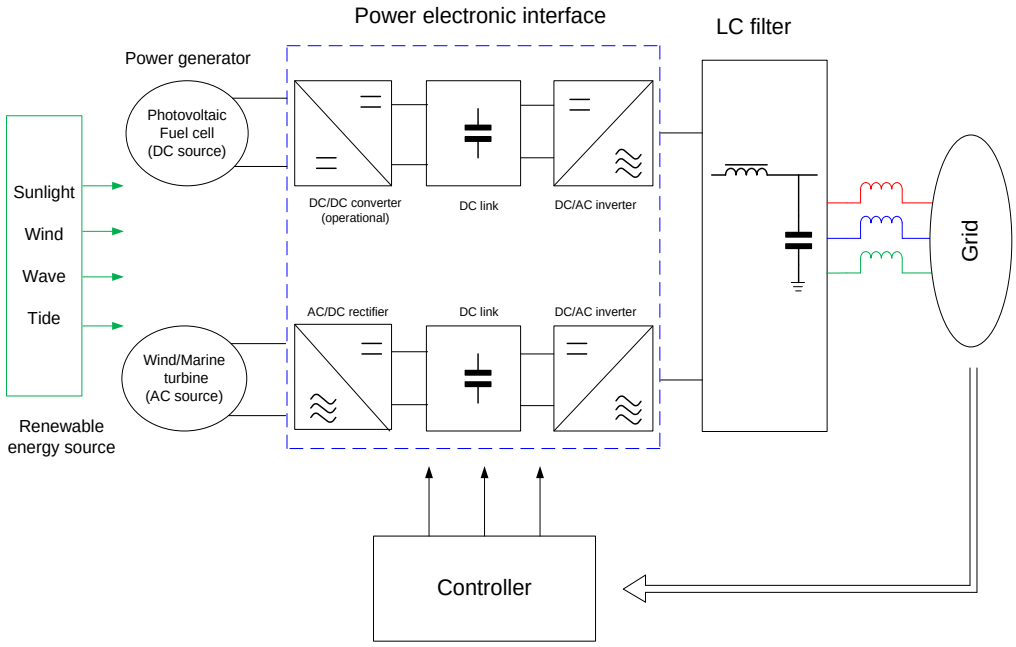

Figure 1.1 Application of power electronics in renewable energy systems

Power electronics has developed rapidly due to the fast evolution of power semiconductor switching devices, control algorithms and microprocessor technology. A typical power electronic system consists of a power converter, a load/source and a control unit. A simple power electronic system, a 3-phase DC-AC converter, is shown in Figure 1.2, along with the multiple components and sub-assemblies that are used in its realisation. Power semiconductor devices are the core components in all power electronic systems to fulfil the functions of power converters and the failures of these devices are responsible for a significant proportion of overall system faults [5].

The reliability of these power devices is crucial to the overall performance and life-cycle cost of a power electronic system and of the power system as a whole. Therefore a detailed understanding of the factors influencing the reliability of power semiconductor devices is becoming an increasingly important topic.

Thermo mechanical breakdown of device packaging is also a major source of reliability concern in power semiconductor modules. The packaging techniques for integrating power semiconductor devices has made impressive progress from single-chip discrete devices to multi-chip power modules to match the growing demand of high current handling capability, increasing power density and effective thermal management. Each generation has evolved to include more components into the modules. Today, power modules integrate semiconductor devices, gate drives, and even passive components required for a complete power conversion solution. This provides tremendous system advantages such as easy instalment, high power density and reduction on weight and space. However, the packaging of these power modules adversely gives rise to relevant reliability issues. Therefore a sound understanding of the physics underlying the potential failures within a power electronic module is a prerequisite.

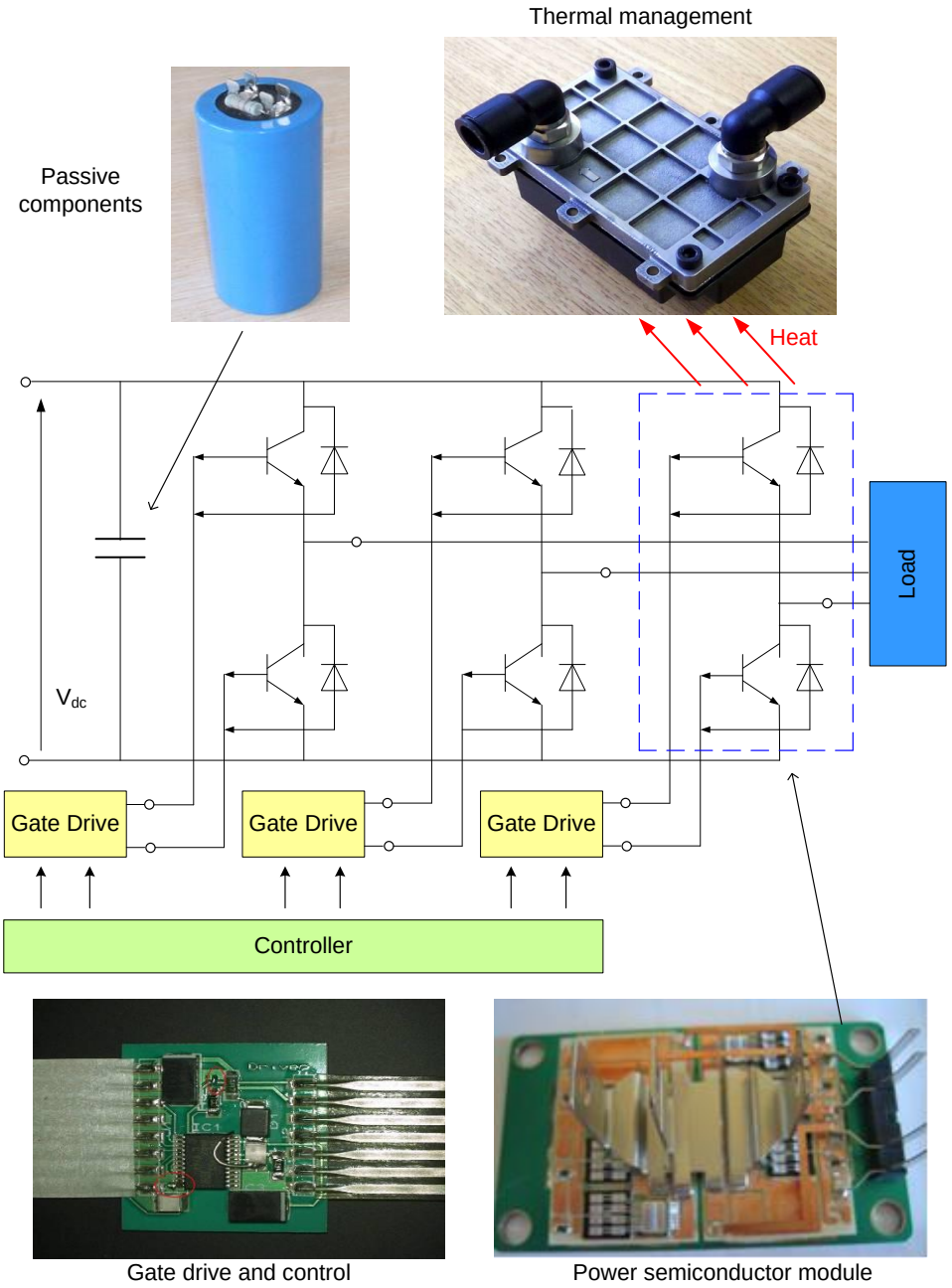

Figure 1.2: Typical power electronic system and subsystems

A key feature of power module packaging is the multi-layer structure, typically including semiconductor die, metalized ceramic substrate and copper base plate (heat spreader) which are typically connected together by the use of conventional solder techniques, and then connected to the external circuit

through metal bonding wires and bus bars, as shown in Figure 1.3(a). The different thermal expansion coefficients (CTE) in the packaging materials cause thermal mechanical stress in adjacent layers under time-temperature exposure.

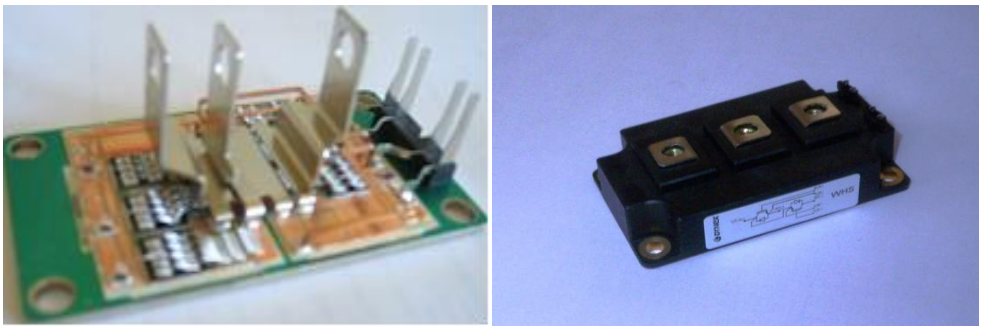

(a) Power module assembly (b) Completed package

Figure 1.3: A half-bridge IGBT module assembly

High temperatures and large temperature swings, imposed by harsh environment and operational conditions are the main loading sources that power modules encounter in all applications. During operation, power devices switch on and off at high frequencies. Heat is generated as a result of conduction and switching losses and the assembly parts are subjected to temperature variations due to device turn-on and turn-off shifting. As mentioned previously, the packaging materials in a typical power module have different coefficient of thermal expansion, and as temperature changes assembly layers expand and contract at different rates. Repeated heating and cooling of the materials causes repetitive mechanical stress in the connections between adjacent layers which can eventually lead to fatigue failures. Therefore, the interconnections within power modules become the major potential failure sites, where time to failure of these assembly parts determines the reliability of the power module as a whole.

Reliability assessment and improvement have long been highly desired to reduce the maintenance cost and to make the product more competitive in the market place. The selection of robust reliability prediction methods in the

design and operation of electronics components has been an evolutionary and controversial process [6]. Traditionally, the electronic industry relies on handbooks such as well known MIL-HDBK-217 for reliability models to determine the failure rate of the components and thus facilitate the calculation of the mean time between failures (MTBF) [7]. These models are statistically obtained by curve-fitting field failure data to a mathematical model, although without physical justification, and where most available data is out-of-date [8]. Although these life estimation standards give failure rate values and acceleration factors for different environmental parameters, root causes of the failures are not addressed in these models; moreover; because these parameters relate to constant failure rates under constant conditions, they cannot be applied to variable service conditions which invariably result in failure rates that change over time. Therefore, the handbook-based method has long been criticized for providing inaccurate information and misleading predictions.

More recently, reliability assessment based on physics-of-failure models is finding widespread application in power electronic products. This method endeavours to indentify the root-cause and fundamental physics of the potential failures in a power module under real time application environmental conditions through stress analysis and the response of the packaging materials to specified loading conditions [9]. Once the potential failure site, failure modes and failure mechanisms are identified, the specific failure mechanism models are then employed to predict the time to failure for each individual component. In this way, the effect of material properties, assembly geometry and any possible damage mechanisms are also addressed which thus allows the explanation of the impact that design, manufacturing and operation has on reliability.

In the Physics-of-Failure (PoF)-based methodology, the development of an effective model makes as critical a contribution to an accurate reliability prediction as the identification of the failure mechanisms themselves [10]. Physics-of-Failure modelling has been increasingly seen as a useful design tool to provide a scientific basis for evaluating new materials or packaging

techniques, as well as to help detect and prevent failures associated with the manufacturing and operation of a product.

Another valuable use of PoF models is the application in prognostics and health management so that the on-going health state of a power module can be monitored and the future health state under its actual life-cycle conditions can be estimated [11-13]. In the implementation of the prognostics and health management (PHM) a PoF model is loaded with real-time temperature profiles obtained by a compact thermal model which is derived by investigating the correlation between device power losses and temperature in a power module. Then, the prognostics information is used to give advance warning of impending failures and helps to take appropriate scheduled maintenance actions without affecting the mission profile of the whole power conversion system, which is a highly desired mission for any renewable energy generation system.

To this end, extensive research has been carried out to develop physics-of-failure models for these joining components/technologies with a focus on wire bonds and solder joints as they are perhaps the most common source of end-of-life failure in power modules. In this thesis a new physics-of-failure model for wire bond interconnects has been proposed which is also expected to be able to predict other interfacial crack propagation behaviour within a power module.

Physics-of-failure models are generally based on established principles of physics, chemistry, mechanics and materials. Input parameters to these models account for characteristics of the investigated materials and parts layout in a power module, which are able to reflect the progressing changes in the materials corresponding to the loading conditions. Then the number of cycles to failure is defined as a function of these parameters. In wire bond lifetime prediction models, accumulated plastic strain, strain energy and crack growth rate are the most frequently used measures of the degradation in the bonding materials, usually resulted from experimental data or finite element analysis. The material constants in the models can be obtained by curve fitting accelerated test data.

In the literature, all of the existing lifetime models for wire bond interconnects have been developed under the assumption that the bonds are subjected to regular cyclic loading, which is not factual in reality. They share the common view that wire bond failure is the outcome solely of damage accumulation during repeated heating and cooling, and the effect of duration of exposure to the temperature loads is not addressed. Therefore the lifetime predictions made by these models lead to a common result that the number of cycles to failure decreases as the loading temperature range increases.

However, more recent findings on the reliability of aluminium wire bonds during extended thermal cycling ranges have raised a number of interesting issues in relation to wire bond lifetime modelling. The experimental observations revealed that when the maximum peak temperature is high enough, the bonds exposed to the larger temperatures range either showed little difference or a slower deterioration rate compared with those exposed to smaller temperature ranges [14-16]. This apparently contradicts the predictions made by the existing models. Indentation hardness and fine-scale microstructural data have also provided evidence that annealing occurs during thermal cycling which is more significant at regimes with higher maximum temperature values, resulting in the removal of some of the build-up damage [17].

These phenomena are not accounted for in the existing lifetime models for wire bonds and consequently highlight the need for an altogether new approach to wire bond life prediction models which can account for the combined effect of damage removal and accumulation processes. In addition, for the thermally activated processes, exposure time is a crucial parameter that determines the restoration degree of the strained material.

These considerations have motivated the proposal of a new time-domain damage-based model which is presented in this thesis. It discards the usual cycle-dependent modelling methodology and is instead based on a time domain representation. In the damage model, the bonding interface damage condition is estimated at regular time intervals through a damage model which

includes the effect of temperature and time dependent material properties. Thus the impact of time at temperature and other rate sensitive processes on the bond degradation rate can be accurately represented. In addition, the model accounts not only for the damage accumulation processes but also the damage removal phenomena. The total damage and the rate of change of damage determine the crack growth rate which leads to the reduction of bond shear strength. In this way, the damage parameter can be related to a measurable deteriorate indicator.

The model is implemented in MATLAB which provides a general modelling environment and is able to obtain a very swift simulation time. A quantitative link is made between damage parameter and strain energy dissipated under loads which contributes to the damage of the material. In addition, uniaxial tensile tests were performed under a variety of loading conditions to quantify the fundamental mechanical properties of the bonding wires and derive the values of strain energy. The results are used to calibrate model parameters through the comparison between strain energy density and saturation value of damage under constant temperatures.

Once satisfactory estimation of the parameters for the model is obtained, the model is operated for various temperature loading conditions to verify that it is able to adequately perform functions as intended. To this end, simulation temperature profiles are specified to characterize the anticipated effects.

Model validation is the essential part of model development process. Accelerated lifetime tests are designed and conducted to collect lifetime data. Wire bond samples are destructively sheared at regular intervals (temperature cycles) to measure the mechanical strength of the bonds. The shear force degradation rated obtained from the experimental data will be compared with simulation outcomes from the proposed model to accomplish the model validation procedure.

CHAPTER 2

PHYSICS-OF-FAILURE APPROACH TO RELIABILITY ASSESSMENT FOR POWER ELECTRONIC MODULES

2.1 Introduction

Reliability issues for power devices have been of serious concern in critical applications and are catching attention in all the power electronic enabled systems. Power semiconductor modules are the core components in construction of power convertors playing a key role in delivering flexible and efficient energy conversion. It is of utmost importance to understand the reliability behavior of these integrated components during service period and gain an insight into the underlying factors that affect reliability. This information contributes significantly in improving reliable operations and reducing the cost of unscheduled maintenance or even may be vital in system safety.

With the urgent need to minimize the cost, weight and volume of the power converters, power device packaging technologies have evolved rapidly, which however raises reliability issues in return. This makes the ultimate system performance and reliability strongly depend on the packaging techniques and materials used to fabricate the individual modules. Therefore it is necessary to perceive explanations for the reliability constraints that limit power module performance and then make use of the knowledge to evaluate the lifetime of the devices.

Meanwhile the selection of reliability assessment method for electronic components plays as important a role as understanding reliability behavior in the whole reliability management. Traditionally, reliability prediction is either based on standard handbook or based on statistical field data and accelerated test data. Until late 1970's, the constant failure rate model had been the only model used for describing the useful life of electronic components [18]. A major drawback of these empirically-based methods is the fact that root causes of failures are not taken into account. Furthermore, the inherent limitations such as the assumption of constant failure rate and the update problem have brought about dissenting voices.

As a result, physics-of-failure (PoF) based models are becoming more widely used in the lifetime prediction of electronic parts. The PoF approach aims to identify the root-cause of the potential failures and set up links between failure mechanisms and degradation behavior under operation environment, through the use of stress and damage models. Then lifetime prediction can be made for new packaging materials, manufacturing processes or new configurations and the information can be used as the feedback to the optimization of the design process. In addition, the application of PoF in prognostics and health management allows the remaining life of an individual power module to be predicted in the real-time operational environment and thus benefit the system reliability and maintenance.

In the subsequent two sections, it firstly talks about the primary wear-out phenomena within a power module through the illustration on the structure of typical wire bonded power modules. The physics behind possible failures are described as well. Then the introduction of PoF approach to reliability prediction of power electronic modules and its application in service health management and prognostics is presented.

2.2 Power electronic modules

2.2.1 Power module assembly

The increasing demand for improving power converter performance, power density [18], reliability and cost reduction has been the driving force to the development of power device packaging technologies. This has resulted in the evolution from the single-chip discrete packaging to multi-chip power modules which integrate multiple power switching devices into one highly efficient package [19-21]. Each generation has evolved to include more components into the modules. Today, power modules integrate diodes, switching devices, gate drives, current sensors, voltage sensors, and temperature sensors. This presents a packaging solution to minimize the size of the power converters whilst provides a physical containment for power electronic devices and offers the potential of better thermal management capability.

Typical power electronics modules have a multi-layered structure consisting of different materials which are able to provide mechanical support, electrical interconnection as well as good thermal conduction. A schematic representation of the structure of an IGBT power module is represented in Figure 2.1. The electrical connections between the terminals of IGBT chip and diode chip are demonstrated in the figure as well. The top side of the chip is connected to a common electrode by ultrasonic wire bonding technology and the opposite side of the chip is electrically connected to another common electrode via soldering process.

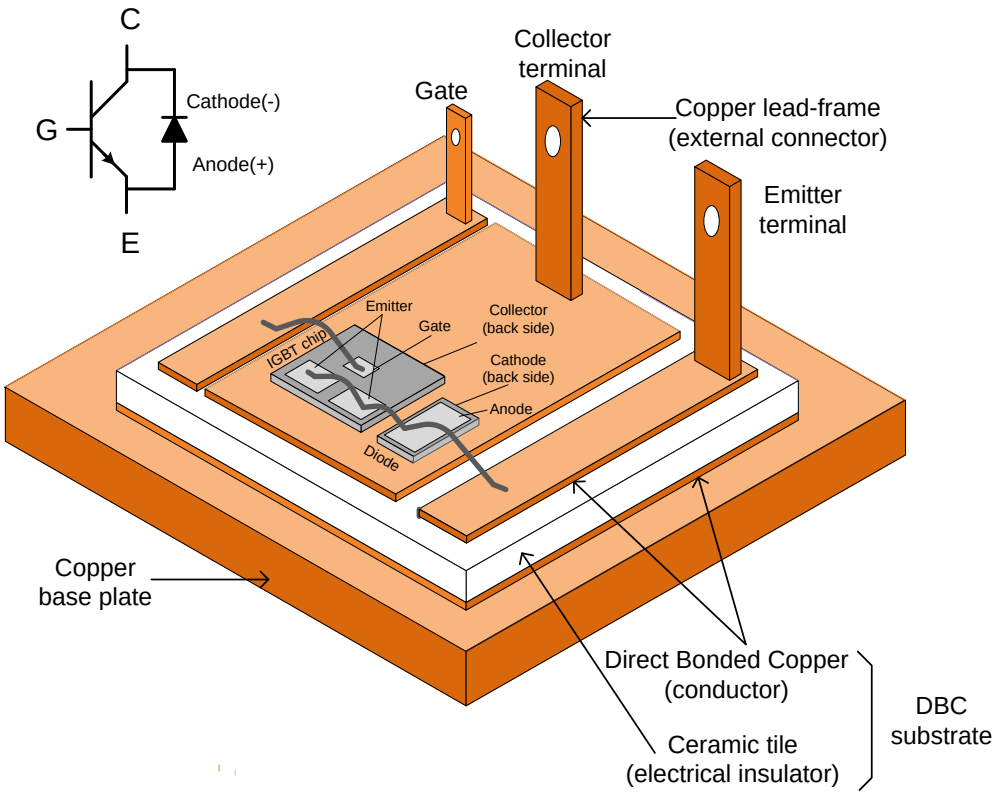

Figure 2.1: Anatomy of a typical IGBT power module

In such a module, semiconductor dies are solder-mounted on electrically insulating substrates, which are in turn soldered to a base plate with high thermal conductivity. Electrical connections are made to the bottom terminal of the semiconductor devices via a conducting metallization layer on top of the ceramic substrates. Metal wires are ultrasonically bonded to connect the top terminals of the semiconductor devices to external bus bars. Heat is removed to a cooling unit via base plate and heat sink. This assembly forms a total of nine separate layers and eight interfaces between the die and coolant in the module. The illustration in Figure 2.2 shows a cross section of a typical Direct Bonded Copper (DBC) ceramic substrate power module, which provides a clear view of the layers. The approximate thickness of each assembly layer is indicated in the figure.

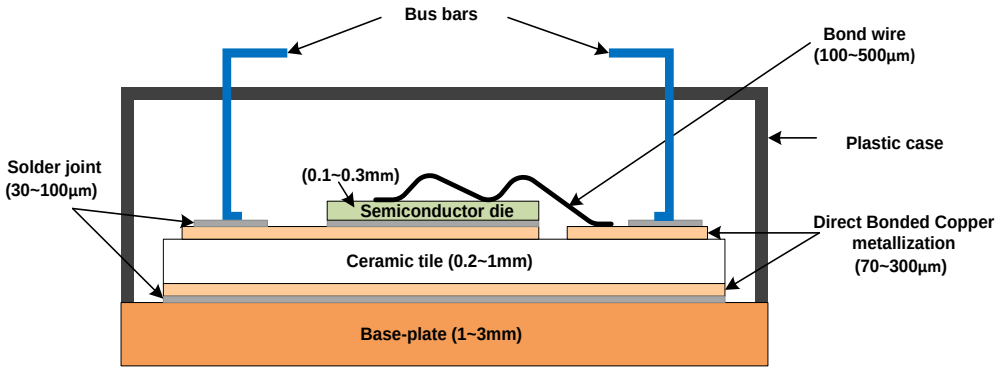

Figure 2.2: Cross-section schematic of a power module

The primary components in a power module assembly include semiconductor device, bond wire, solder alloy, DBC substrate and base plate. Their fundamental materials properties differ widely which bring about the reliability issues. In the following paragraphs, some of the materials that are frequently adopted in power packaging assembly and the relevant physical properties are briefly introduced.

2.2.1.1 Semiconductor device

Silicon is the standard semiconductor material for fabrication of power electronic devices which are not ordinarily operated above 125°C. Increased power density requirements for aerospace, automotive applications mean that higher junction temperatures are to be encountered in power electronics. Consequently, wide-band gap semiconductors (with bandgaps greater than 1.7eV) like silicon carbide (SiC) and gallium nitride (GaN) are currently being introduced to switching power applications as they offer the potential to overcome the restraints of silicon on the operation temperature, power rate and switching frequency due to their superior physical characteristics [22]. Some of the relevant physical properties of three semiconductor materials are listed in Table 2.1[23].

The wide bandgap energy of these materials allows them to maintain

semiconductor behavior at much higher temperatures than silicon, which in turn permits the devices based on these materials to function at extremely high temperatures. The consequent high electric breakdown field enables the devices to withstand higher voltage and the resultant lower on-resistance and faster switching frequencies can significantly improve power efficiency [24-26].

However, the commercial availability of wide bandgap semiconductor wafer imposes big challenges to the development of the related power devices to some extent. And the implementation of these higher temperature devices requires compatible interconnect technologies. On the other side, the qualification and reliability investigation based on Si device technologies has seldom been performed above Military Standard stipulated temperature of 125°C [60]. If the same standard or method is applied to the power devices based on wide bandgap semiconductors, it may result in inconsistent lifetime prediction.

Table 2.1: Selected physical properties of semiconductor materials

Properties	**Si**	**Si-C (4H)***	**GaN**
Band Gap (eV)	1.1	3.2	3.4
Electric breakdown field (kV/cm)	300	2200	2000
Electron mobility (cm^2/V·s)	1500	1000	1250
Hole mobility (cm^2/V·s)	600	115	850
Thermal conductivity (W/cm·K)	1.5	5	1.3
CTE (ppm/°C)	2.6	3.7	5.6

*The "4H" in SiC-4H refers to the crystal structure of the SiC material

2.2.1.2 Bond wire

Aluminum (Al), copper (Cu) and gold (Au) are the most widely used bonding wire materials in power electronic assemblies as good thermal and electrical conductors [27]. Sometimes, alloys based on these metals (e.g. with 1%Si or 1%Mg) are preferred to pure wires to improve corrosion resistance and provide better strength so as to meet necessary breaking loads and elongation parameters [28]. Al wires are typically selected for ultrasonic wedge bonding. Light weight and low cost gives more merits to this material as a choice for bonding wire.

Gold wires are particularly suitable to thermosonic ball bonding. But the relatively high cost is a restriction to its application. Moreover gold material has a high tendency to form brittle gold-aluminum intermetallic compounds with the aluminum metallization on the bond pad, which is prone to induce bond failure by fatigue or stress cracking in the presence of thermo-mechanical loading [27].

Compared with aluminum and gold, copper has a better thermal conductivity so copper wires dissipate heat within the package more quickly and efficiently [29]. Also its significantly lower electrical resistivity results in less amount of heat generation implying the good current carrying capacity for a given wire diameter. These properties make copper a preferred bonding wire material for high current devices. And the mechanical properties of Cu such as higher yield strength and less thermal expansion show promise of better reliability [30]. However, copper wire is harder than both gold and aluminum therefore bonding parameters must be kept under tight control to avoid damage to the chip surface. Furthermore the formation of oxides is inherent with this material, so bonding has to be processed in an inert atmosphere and even storage and shelf life becomes an issue.

Table 2.2 lists some of the physical and mechanical properties of these three frequently used wire bond materials.

Table 2.2: Bond wire material properties

Material Properties	**Aluminum**	**Copper**	**Gold**
CTE (ppm/°C)	23.1	16.5	14.2
Thermal conductivity (W/m·K)	237	398	317
Electrical resistivity (10^{-6}Ω/cm)	2.7	1.7	2.2
Melting temperature (°C)	660	1083	1063
Young's modulus (GPa)	75	130	88
Yield strength (Mpa)	7-11	70	112
Tensile strength (Mpa)	100-200	210-370	120-220

2.2.1.3 Solder alloy

In the process of power module assembly, solder paste or preform is applied via reflow soldering process to attach semiconductor chips to the substrate and mount substrate onto the copper base plate. Tin-lead (Sn-Pb) and their alloys have been the most extensively used solder materials. Sn63Pb37 was among the principal selections not only due to the well known advantages of its eutectic composition but also because it exhibits excellent mechanical strength and thermal/electrical conductivity [31]. However, due to the environment and health concerns, leaded solder has been banned since July 1, 2006, which has forced a move to lead-free solders. Tin-silver-copper (SnAgCu) solder family is accepted as the most popular replacement so far [31, 32]. Table 2.3 lists some material properties of three eutectics or near eutectic solder alloys.

Table 2.3: Solder alloys material properties

Material Properties	**$Sn_{63}Pb_{37}$***	**$Sn_{95.5}Ag_{3.8}Cu_{0.7}$**	**$Sn_{96.5}Ag_{3.5}$***
CTE (ppm/°C)	24	17.6	21.5
Thermal conductivity (W/m·K)	50	60	55
Electrical resistivity($10^{-6}\Omega$/cm)	0.145	0.132	0.123
Melting point (°C)	183	217	221
Tensile strength (Kgf/cm^2)**	525	600	580

* Eutectic composition

**1Mpa=10.2Kgf/cm^2

Apart from the price of the alloy metal, selection of a suitable solder material mainly depends on the particular application requirements. The content and the amount of each constituent element vary the chemistry and physical properties of the bulk solder alloy, which affects the solderability and reliability performance in different loading environments [33]. On the other side, formation of the intermetallics (IMC) phases during soldering is a fundamental aspect of joint formation; however, the joint characteristics of the solder changes over time due to the instability and evolution of these IMC phases.

2.2.1.4 Substrate

Direct Bonded Copper (DBC) substrates are widely used as an excellent solution for electrical isolation and thermal management of high power semiconductor modules. A DBC generally consists of a ceramic tile onto which a sheet of pure copper metal is attached to one or both sides by a high-temperature oxidation process. In this process, the pure copper and ceramic substrate are heated in a nitrogen atmosphere with low oxygen partial pressure

under carefully controlled temperature and time. Direct bonding is achieved by the formation of a copper-oxygen eutectic composition between copper and the ceramic substrate [34].

The most commonly used materials for base ceramics include alumina (Al_2O_3), aluminum nitride (AlN) and silicon nitride (Si_3N_4). In this structure, copper layer provides the capability to carry high current and the ceramic provides high voltage insulation. Furthermore, the thermal expansion coefficient of the global substrate is closer to that of a semiconductor die, and this reduces the effect of fluctuating stress at the interface between the chip and the substrate, thus ensuring good thermal cycling performance.

Several related physical and mechanical properties of three DBC substrates are listed in Table 2.4. It can be seen that AlN has the highest thermal conductivity but its fracture toughness is lower than that of Al_2O_3 and Si_3N_4 which implies a low resistance to brittle fracture of the AlN during thermal cycling. Si_3N_4 has the lowest CTE and superior fracture toughness. Al_2O_3 is the most widely used in power module due to its low cost although it is not a very good thermal conductor [35-38].

Table 2.4: Substrate ceramic material properties

	Al_2O_3	**AlN**	**Si_3N_4**
CTE (ppm/°C)	6.7 ~ 7.1	4.2 ~ 4.5	2.8 ~ 3.2
Thermal conductivity (W/m·K)	20-27	150 ~ 230	30 ~ 90
Fracture toughness ($MPa \cdot m^{\frac{1}{2}}$)	3.3 ~ 3.7	2.7	5 ~ 6.5
Young's modulus (MPa)	380	330	310

Besides DBC substrate, active metal brazing (AMB) metallization technique is also used to join copper foil and ceramic substrate. This is a high-temperature high-vacuum process in which a braze alloy is brought slightly above its melting temperature and forms an interlayer between the ceramic and copper.

In some cases, active elements, often Ti (titanium), are added in the braze alloy to improve the wetting on the ceramic surface [38].

2.2.2 Dominant failure modes, sites and mechanisms in power modules

It is well known that the reliability of power semiconductor modules is mainly constrained by fatigue and creep processes which bring about the wear-out of packaging materials leading to interconnect failures. Fatigue is a progressive structural damage caused by a repeated oscillating stress below the yield stress of a material. The process starts with dislocation movements, forming persistent slip bands that act as stress risers and nucleate microscopic cracks. In the end, macroscopic cracks will be initiated in the areas of stress concentration which is followed by incremental crack propagation and leads to final fatigue failure.

Creep is a time-dependent deformation behavior that occurs when a material is subjected to a constant load at high temperature (homologous temperatures above 0.4). Homologous temperature expresses the temperature of material as a fraction of its melting point temperature using the Kelvin scale. The rate of this deformation depends on the applied stress, exposure time and temperature to the load as well as the material properties. Creep rate increases with temperatures and is more severe in materials subjected to the heat for long periods. Damage accumulation in module packaging materials usually occurs through both fatigue and creep processes and it is likely to include fatigue-creep interactions.

High temperatures and large temperature swings, imposed by harsh environment or arising from the semiconductor device power dissipation, are the main loading sources that power modules encounter in applications. During operation, the power devices contained in a power module will have conduction losses when a device is ON and suffers switching losses that occur during switching transitions. Heat is generated as a result of these losses and therefore the module assembly parts are subjected to temperature variations

due to device turn-on and turn-off shifting. As the temperature changes, package materials expand and contract at different rates because of their different coefficient of thermal expansion (CTE) which induces mechanical strain-driven stress at joining interfaces in the assembly and eventually causes fatigue failure [39].

On the other hand, some packaging materials such as solder alloys have relatively low melting points. This means that their homologous temperature can be about 0.6 at room temperature. Therefore in addition to fatigue, creep plays a dominant role in the deformation behaviour of the solder joints.

The package-related failure modes that are most frequently observed in power modules include solder joint degradation, substrate delaminating, wire bond lift-off and bond heel cracking [39, 40]. The failure mechanisms with regard to these failure modes are introduced in the following subsections.

2.2.2.1 Wire bond lift-off

Bonding wires are normally ultrasonically bonded onto the metallization pads on the silicon semiconductor devices. Ultrasonic bonding is usually carried out at room temperature and is achieved by pressing the metal wire onto the bond pad metallization on a semiconductor and vibrating it using high frequency ultrasound, generating frictional energy. The energy applied onto the bond pad breaks down the surface oxide film, allowing the formation of metallurgical bonds between the wire and the bond pad [41, 42]. The ultrasonic vibration and thermal energy applied to create the wedge bonds induce stresses on the wire heel making it a dominant failure site. While the detailed bonding mechanism involved in the process is still not well understood, it is believed that bonding variables, such as ultrasonic power and bonding force have decisive influence on bond reliability [43]. Lift-off bond footprints reveal that after the ultrasonic bonding process, joining occurs only at the periphery of the bonding area while in the middle, the wire is not in contact with the metallization [44, 45]. As

ultrasonic power or bonding time is increased, bonding area expands towards the centre so that the bond gets stronger [45, 46]. However, too high a power can however lead to wire failure or induce chip damage [46].

As-bonded wires often contain pre-existing heel cracks due to the wire flexure during loop formation as well as pre-existing interfacial voids/oxide particles which compromise the integrity of the bond achieved.

Wire bond lift-off predominantly is the result of horizontal crack growth near bonding interface, which arises out of material fatigue caused by shear stresses generated between the bond pad and the wire due to their CTE mismatch [47, 48]. It is observed that cracks are usually initiated at the edge of the bond foot. In some cases, crack progress within the bulk wire. There are also experimental observations showing crack propagation along chip-metallization interface or along the plane just above the wire-metallization interface. The optical micrographs of these are demonstrated in Figure 2.4.

The oxide debris produced during the ultrasonic bonding process and impurities on the bonding pad due to inadequate cleaning expedites cracks at the bonding interface leading to bond lift-off.

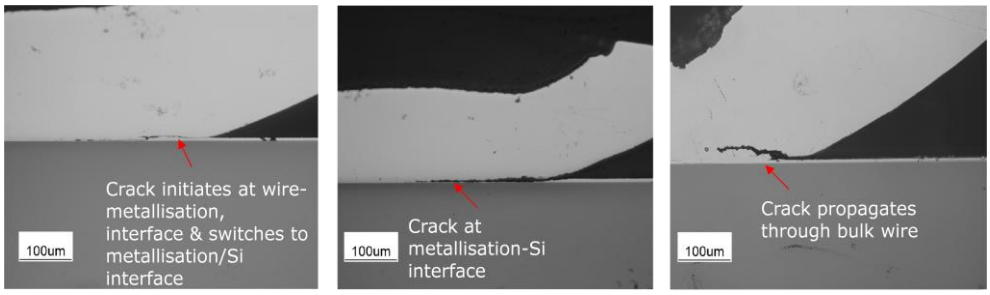

Figure 2.4: Crack propagation in wire bonds

2.2.2.2 Wire bond heel /arch cracking

Bond wire heel crack is caused by mechanical bending stress originating from wire loop formation. During operation, bond wires undergo temperature

excursion dominated by ohmic self-heating and power dissipation from the semiconductor device during turn-on and turn-off. The temperature swing generates displacement at the top of the loop which produces a change in the bending angle leading to mechanical bending stress at the heel. This kind of failure is strongly dependent on the loop geometry. In some cases, reinforcement solutions such as the application of glob top [49] to encase the bond foot or soldering a thin molybdenum plate as a strain buffer on the Si chip [50] are used in order to improve the lifetime of the wire bonding connections. However this may likely transfer the flexural stress from the bond heel to loop arch and leads to arch crack. Two optical micrographs of such heel crack and loop arch cracks are shown in Figure 2.5.

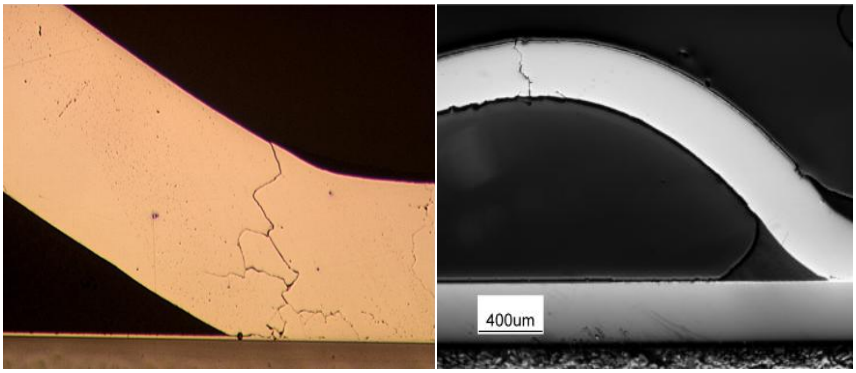

Figure 2.5: (a) Wire bond heel crack (b) loop arch crack

2.2.2.3 Solder joint cracking

Solder joint failures can be mostly attributed to three major mechanisms: fatigue failure due to cyclic thermo mechanical stresses; creep failure induced by the continuous stresses at elevated temperatures for a long period of time; and the growth of intermetallic compounds formed during the soldering process.

Solder joint fatigue failure primarily results from cyclic shear stresses induced

by CTE mismatch between solder alloys and attached components under temperature swings. A large part of the mismatch is accommodated by plastic deformation within the solder joints as the materials of the attached elements (substrate and semiconductor dies) are comparatively rigid. Repeated shrinkage and expansion due to temperature changes produces cyclic stress in the solder bulk which initiates crack in the area of stress concentration (generally at the corner of the joining interface) followed by incremental crack propagation toward the center, and eventually leads to solder fatigue failure.

Creep becomes significant at homologous temperatures close to and above 0.5 if the loading rate is slow enough for creep deformation to occur. Common solder alloys have low melting point temperatures in the range of 120 ~ 320°C [51]. Therefore creep plays a very important role in deformation behavior of solder joints throughout the service period, as device operating temperatures can be within this range. During creep stages, solder undergoes progressive inelastic deformations over time. High temperature and accumulated strain facilitate vacancy diffusion which results in creep voids forming and coalescing and eventually leading to creep failure [52].

In Figure 2.6, three optical micrographs have shown fatigue and creep cracking of the solder layer between silicon device and DBC substrate in the course of thermal cycling ranging from -60°C to 170°C. It can be seen that the crack formed at the edge and propagated towards the centre.

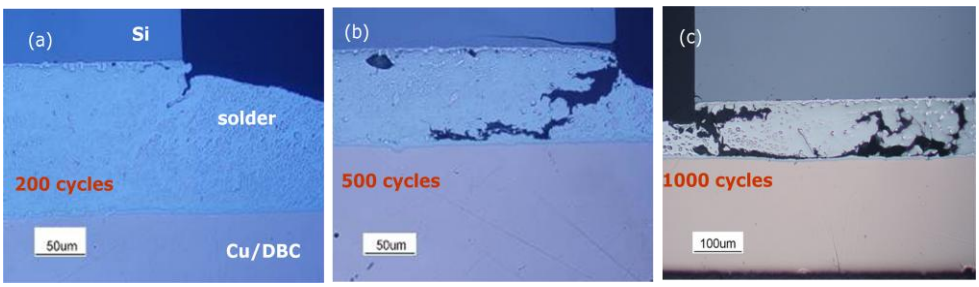

Figure 2.6: Crack initiation and growth in die-attach solder joints

The formation and growth of the intermetallic compounds (IMC) during soldering process is another major cause of solder failures. Although a thin IMC layer between solder bulk and soldered materials is an indication of good metallurgical bonding, it makes solder joints more susceptible to crack growth. Because the IMCs are harder and more brittle than the bulk solder matrix and the CTEs are different from the solder alloys, internal stress are produced in vicinity of these secondary phases which will become the nucleation sites for voids and micro cracks during the exposure of fluctuating temperature loads. Over the period of storage or application of the assembly, the IMCs increase in thickness and also precipitate within the bulk especially if the temperatures are near melting point of the solder alloy [53, 54]. In Figure 2.7, the generation of the IMCs layers and the effect of the IMCs particles on crack growth are shown clearly.

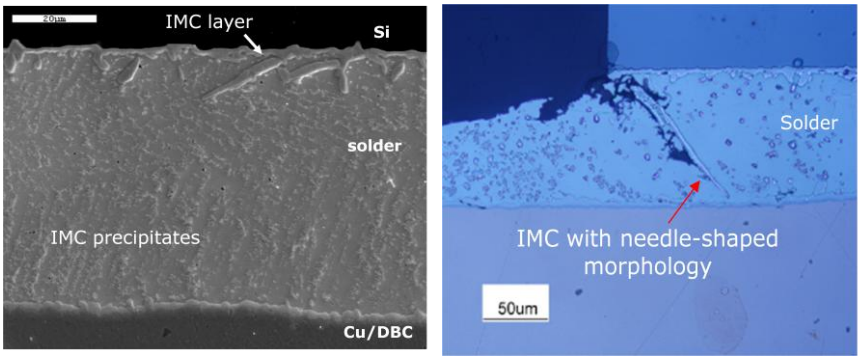

Figure 2.7: (a) Tin-silver forms IMC layers at solder interface and precipitates within the bulk (b) Effect of IMCs on crack propagation

2.2.2.4 Substrate delamination

Substrate failure is primarily driven by CTE mismatch between copper and ceramic layers which leads to brittle fracture of the ceramic material itself or copper layer delaminating [55]. Ceramic fracture occurs as a result of progressive cracking in ceramic layer. It is usually initiated by the cracks at the outside edge of the copper foils which propagate down into the ceramic

material by an angel from the copper-ceramic interface. As the crack reaches about one third of the way through the ceramic layer, the crack direction turns parallel to the substrate surface causing conchoidal fracture [55-57]. A picture of conchoidal fracture within ceramic layer is shown in Figure 2.8 (a).

Copper layer delamination is mainly associated with the substrates of high fracture toughness. Fracture toughness refers to stress resistance of a material to propagate a preexisting crack, i.e. the highest stress intensity that the material can withstand without fracture. When the fracture toughness of the ceramic is comparatively high, such as Si_3N_4 ceramic, its resistance to a brittle fracture is larger. Therefore for the substrates made up of materials with high fracture toughness, a fatigue crack is more prone to propagate along the copper/ceramic interface instead of working its way into the ceramic layer. There is usually no apparent cracking of ceramic. Figure 2.8 (b) has shown a picture of copper layer peeling off the ceramic substrate.

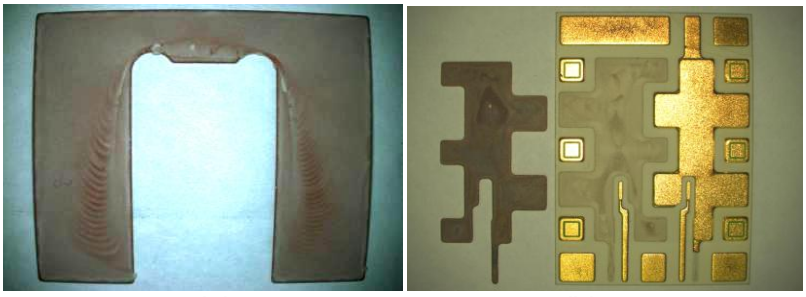

Figure 2.8: Substrate failures: (a) Conchoidal fracture within ceramic layer (b) Copper layer peeling-off from the ceramic substrate

2.3 Physics of failure approach to reliability assessment

Following the rapid development in device packaging technology, reliability issues in the design and operation of electronics components have been paid even more attention. Selection of the methods for the reliability prediction of

electronic products has been in an evolutionary and controversial process. It evolves from predicting reliability based on statistically curve fitting field failure data to design-for-reliability enabled by root-cause failure analysis [58]. Currently assessing reliability of a power electronic device module at real-time operation conditions is achievable by a technique called prognostics and health management.

In this section, reliability prediction methods used for electronics components are presented including the transition from relying on reliability handbooks to the employment of science-based physics of failure reliability modeling as well as the application of PoF in prognostics and health management for power modules.

2.3.1 Handbook-based reliability prediction method

2.3.1.1 Introduction

"Reliability is the probability that an item will perform its intended function for a specified period under stated conditions". [59] A failure is said to occur when an item does not perform a required function. In classical reliability theory, failure rate is used as a standard of reliability measurements.

Traditionally, electronics industry has relied on reliability handbooks for constant failure rate models to perform reliability prediction for electronic components. The first brick of the handbook-based reliability prediction methodologies was laid with Military-Handbook-217 (MIL-HDBK-217) published in 1965. It was based on curve fitting a mathematical model to historical failure data from field operation or from laboratory tests to determine the constant failure rate of parts for military systems and equipment. In the last version of MIL-HDBK-217F, straightforward failure rate equations were presented for nineteen major electronic component categories used in modern military systems ranging from microcircuits and discrete semiconductors to passive components such as resistors and capacitors [60].

The models usually have a constant base failure rate modified by including several π factors to take into consideration the effect of part quality, temperature and environmental stress (Equation 2-1). The MTBF can then be determined by taking the inverse of the failure rate.

$$\lambda_p = f(\lambda_b, \pi_i) \tag{2-1}$$

Where:

λ_P: calculated constant part failure rate

λ_b: base constant part failure rate

π_i: a set of adjustment factors

Military-Handbook-217 (MIL-HDBK-217) soon became the industry standard for reliability prediction. It was subsequently updated several times to keep pace with technology advancement as well as the changes in prediction procedures. Meanwhile several companies and organizations decided to develop their own prediction handbooks more suitable for their own products and systems. In most cases, they adapted the MIL-HDBK-217 philosophy of curve-fitting field failure data to some models in the form of Equation (2-1).

2.3.1.2 Limitations

Although these constant rate models are still employed for lifetime prediction by electronic industries, there have been many voices of disapproval due to some of the concerns regarding technical assumptions and the intrinsic problems associated with the development of the models [61].

A well recognized drawback of this handbook-based approach to reliability prediction is that these models do not identify the actual origin of failures or provide explanation on the underlying physics behind the wear-out phenomena. The effects of structure geometry and material properties, etc. on reliability behavior are not addressed so that the reliability cause-and-effect relationship

is not captured. Therefore these handbook-based methodologies cannot give accurate guidance for design or manufacturing.

The update on the handbooks is another problem to reckon with. Most of the models are out of date by the time they are applied and more recent technologies are not included or defined in the published models. As a result, the extension of these models to state-of-the-art products is inadequate and even heavily penalizes new materials and new technologies [8].

Furthermore, almost all the reliability predictions made by handbook models are based on the assumption of the constant failure rate, implying that the reliability of a component is independent of age [62]. However, components during service period frequently show wear-out effects which means that failure rate increases with time. And constant failure rate leads to exponential failure distributions which does not account for the impact of failure mechanisms on the failure distribution during the whole lifetime.

Above all, reliability assessment based on handbooks and statistically collected data can hardly be successful. It is essential to go below the macroscopic level to the microscopic level of the physical failure mechanisms to obtain more meaningful and accurate predictions. This has brought about the employment of the physics-of-failure approach to reliability prediction for electronics components [63].

2.3.2 Physics-of-failure based reliability prediction approach

Physics of failure is a science-based approach to reliability assessment and improvement. It endeavors to reveal the fundamental processes and mechanisms that induce failures so as to relate the underlying physical behavior of the constituent materials to the reliability performance of the end-items [64].

2.3.2.1 Introduction

The PoF approach has been used successfully for decades in the design of mechanical, civil and aerospace structures. Comparatively, the introduction of this approach into electronics was slow and lagged behind because unlike mechanical and structural items, most electronic failures are not directly observable and the characterization of electronic materials is more difficult as well.

Physics-of-Failure was formally conceptualized for electronics at the First Annual Symposium on Physics of Failure in Electronics, held in September 1962. The goal of this symposium was to call for a thorough understanding on mechanisms and physics of failures to meet the high reliability requirement posed by advanced electronic systems. Through the 1970s and 1980s, several failure mechanisms and mathematical models were developed for a wide range of electronic components such as capacitors, semiconductors, resistors, and interconnect. By the late 1980s and early 1990, the use of the PoF approach for reliability assessment was vigorously advocated within electronics industry as opposed to the traditional part counting technique and thus initiated the application of PoF in electronics packaging and interconnections [65].

The PoF approach is not only employed for reliability prediction it also applies reliability analysis early on in the design process and thus enables the evaluation of design and manufacturing alternatives in specific applications, which realizes the transition from predicting reliability to designing reliability [59]. PoF focuses on understanding the cause-effect relationships of the physical processes under loading conditions and identifying mechanisms that cause degradation of materials and components. It is based on the analysis of loads and generated stresses in an application environment and evaluating the impact of these on the materials based on the physical and mechanical properties of the materials. The obtained knowledge and information related to failure physics can then be used in reliability improvement and product qualification test [66].

2.3.2.2 Implementation

Figure 2.9 depicts a broad feature of the procedures that are followed to implement Physics-of-Failure approach for predicting the reliability of electronic components.

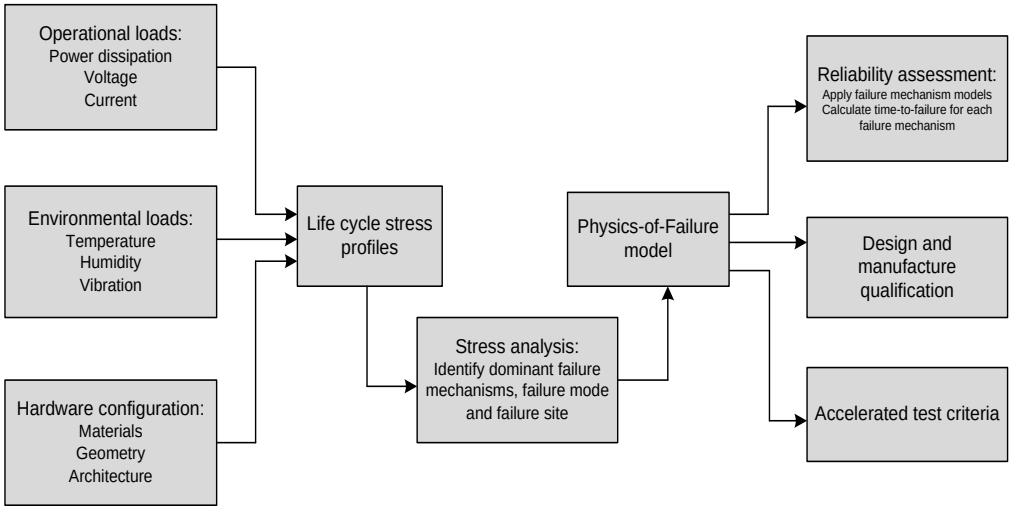

Figure 2.9: Implementation of Physics-of-Failure approach

The first step is to investigate the environmental and operational loading conditions to which the product will be subjected to, and at the same time examine the hardware configuration and properties of the constituent materials. Then the information can be obtained with regard to the stresses that the specified loading conditions impose on the electronics assembly as well as the reaction of the packaging materials to the stresses. In the next step, the stress distribution analysis is combined with the accelerated test data to identify the failure location, the form in which failure occurs (failure mode) and how failure might take place (failure mechanisms).

After the underlying failure mechanisms have been determined, the appropriate physics-of-failure models are selected for the identified failure mechanisms. In most cases, available theoretical models are employed. Consequently many

efforts have been put into developing effective lifetime models which are usually semi-empirically derived using statistically designed experiments based on fundamental principles of physics, mechanics and materials.

Once the models are established, the time to failure is estimated for each potential failure mechanism. The output from this assessment can be used to determine whether a product will survive for its intended application life, or provide feedback to the design, test and manufacturing processes for increasing robustness against the dominant failure mechanisms and failure sites.

2.3.2.3 Advantages and disadvantages

Physics-of-Failure approach proactively incorporates reliability into the design process that enables reliability assessment of newly designed electronic products before their actual manufacture. PoF methodology also establishes a scientific basis for evaluating new materials and new packaging technologies as it explicitly addresses the factors like material properties and assembly geometry, which strongly influence the reliability of end-products.

Therefore it is not only a tool to allow reliability prediction but also a reliability enhancement technique. The knowledge of the root cause of device degradation behavior can be used to prevent failures and thus to improve reliability through robust design and manufacturing practices [63, 67].

Unavoidably, however, PoF methodology has disadvantages. Many wear-out mechanisms are still not well understood and physics-of-failure models may not be effectively available under all the circumstances. Materials are inhomogeneous in nature and therefore material failures are probabilistic which makes it difficult to capture the uncertainty. These challenges inevitably hinder the application of the Physics of Failure approach. Also, the PoF method is still not able to account for human factors in design and manufacturing.

2.3.3 Prognostics and Health Management based on physics-of-failure

2.3.3.1 Introduction

The employment of PHM to power modules is another important milestone, which has revolutionized the perception of reliability and has resulted in a broad range of applications [11]. PHM seeks to optimize overall system utility and reduce life-cycle cost by detecting anomalies, diagnosing problems, predicting time to failure and managing subsequent maintenance.

Some of the traditional approaches [68, 69] applied in failure prognostics for electronics such as simple notification by embedding sensor devices and failure precursor monitoring may not be practical for power electronic modules. For the method of using sensor devices, the failure site and failure mode within a power module is usually not a single point and failure mechanisms vary in accordance with the loading conditions which bring problems in selecting and embedding appropriate fuse or canary devices. On the other side, recalibration of such 'canary' devices with the age condition of the module after replacement is a considerable disadvantage. As for the precursor monitoring method, determination of measurable precursors imposes difficulty as the physical degradation of the packaging materials may not necessarily cause any loss of electrical performance or induce significant change in the early stage. System complexity and coupling effects makes monitoring and reasoning of failure precursor even harder. These lead to a result that the monitored precursor can not necessarily indicate the failure that it is supposed to predict. For example, increase of forward voltage is usually used as the precursor to indicate wire bond lift-off failures. However in the case of applying glob tops on the bond feet, cracks may develop through the bond while electrical contact still remains; so the read from forward voltage cannot actually tell the bond interface failures. In addition, the correlation between the variables and failures is typically obtained with respect to the expected or accelerated loading profiles but it is difficult to characterize the precursor parameters under all possible loading scenarios in highly varying life cycle conditions.

2.3.3.2 Physics-of-failure based PHM

Alternatively, the Physics-of-Failure approach has been widely employed to implement PHM for power electronic devices where fatigue/creep induced wear-out is the major failure mechanism. When combined with PoF models, it is possible to make continuously updated predictions based on actual environmental and operational condition monitoring of each individual components. It thus allows accurate assessment of remaining lifetime for each assembly part under real time by assessing the extent of degradation due to the cumulative load exposure life-cycle loads at any point of the application [11-13]. It also enables customers to monitor the on-going health state of a power module under its actual operational condition and to estimate the future health state based on current and historical health conditions. Then the prognostics information can be used to give advance warning of impending failures in the whole power electronic conversion system and help to take appropriate scheduled maintenance and logistics actions without affecting the success of the mission, which consequently reduces the life cycle cost.

In the process of the implementation of this method, there are two main tasks: (1) determination of the real-time device temperature under operation and (2) estimate of the damage accumulation due to repeated thermo mechanical stresses in the packaging materials [12, 13]. The first task is accomplished by a compact thermal model which can be obtained by investigating the correlation between device power dissipation and resulting temperature changes within a power module. The real-time loading profiles can then be captured for junction temperature and the temperatures of each layer inside power modules. Meanwhile physics-of-failure based models are needed to enable the prediction of the accumulated damage in the packaging materials under different loading conditions. The combination of the real-time life-cycle loading profiles with the physics-based models allows the life-consumption level of the components to be monitored and thus the remaining life can be estimated under real operational environment. Figure 2.10 provides an overview of the concepts of PHM for power devices in an electronic system and also shows the

implementation of physics-of-failure based prognostics for power modules through in-service life consumption estimation.

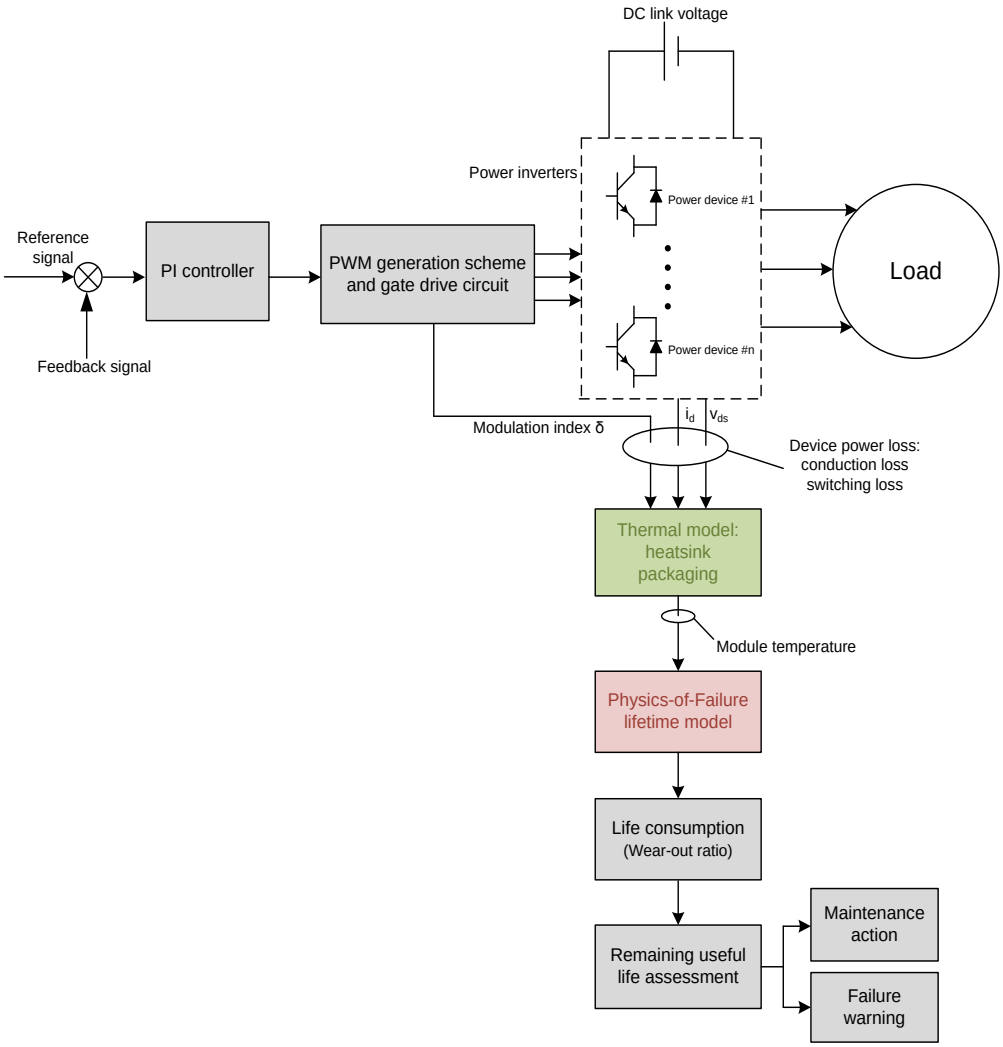

Figure 2.10: Physics-of-Failure based Prognostics and Health Management

2.4 Summary

Power semiconductor modules play a key role in delivering flexible and efficient energy conversion. Their applications in increasingly harsh environments and demanding operation regimes require them to work to the current limits whist remaining extremely high reliability standard. The rapid progress in miniaturization and high complexity imposes an even larger challenge on the reliability issues. As a multi-layer integrated product, failures occurred in package elements are of the major concerns that influence the performance of the power device modules.

Physics of failure is a scientific approach to reliability design, assessment and enhancement for power modules by identifying the root cause of the failures instead of simply relying on statistical failure data. The obtained information can be combined into parameter optimization, material selection and new packaging technique in the design stage and manufacturing processes. The application of physics of failure in prognostics and health management enables the reliability of power modules to be estimated under their actual operational conditions, which is greatly beneficial to the maintenance of the electronic sub-system and the whole power system.

The development of effective PoF models is indispensable to the successful implementation of physics of failure methodology. In the study on the reliability of power modules, attentions have been mainly put into solder joints and wire bonds as the dominant failure sites. The work in this thesis concentrates on the development of a physics-of-failure based lifetime model for wire bond interconnects in power modules. In Chapter 3, the processes of deriving a physics-of-failure model are introduced and a review on the models for wire bonds in the literature is presented.

CHAPTER 3

PHYSICS-OF-FAILURE MODELS FOR WIRE BOND INTERCONNECTS

3.1 INTRODUCTION

Physics-of-failure approach is now finding widespread applications in the reliability prediction, qualification test and health management of power electronic devices. It has a large number of advantages over the traditional handbook methods which are based on the statistics of field failure data, in that physics-of-failure aims to identify the root cause of the potential failures by understanding the physical processes that cause degradation and failure of the materials and components under application conditions. The lifetime under operation environment can be related to relevant failure mechanisms through the use of stress and damage model.

In the PoF-based reliability assessment methodologies, development of an effective physics-of-failure model is essential to a meaningful prediction. At the same time it is one of the main challenges for electronic products as most failures occurred in electronic packaging and interconnections are microscopic and not visible to the naked eye. Over the last two decades, great progress has been made in characterization of packaging material properties with the aid of the fast development in computer science and advanced technologies. This speeds the development of PoF modelling technology in the area of semiconductor packaging.

3.2 PROCEDURE FOR DEVELOPMENT OF PHYSICS-OF-FAILURE MODELS

Physics-of-Failure models are usually obtained semi-empirically by the relationships or equations derived from basic principles of physics, materials and chemistry [10]. Knowledge of the failure mechanism and the intended operational conditions are essential inputs to physics-of-failure models, allowing the behaviour of the electronic devices to be described at structural level. Familiar empirical relations in which strain or stress amplitude and the rate of crack growth per cycle are model parameters are usually employed to relate lifetime to the identified factors that govern failures.

The process of deriving a physics-of-failure model begins with a thorough understanding of the failure mechanisms that could be activated in the power electronic modules under specific loading conditions. The preliminary step is to find out the environmental and operational conditions to which the power module is subjected to. Anticipated service environment, e.g. application in aerospace, automotive, marine/wind energy generation system or home appliance, provides the broad information about the imposed external lifecycle loads like temperature, humidity, vibration. Operational condition refers to electrical loads including current, voltage, power loss and switching frequency and so on.

Then the stress analysis is carried out combining with the knowledge about the geometry, layout and properties of the packaging materials in the power modules to determine (1) how the applied life-cycle loads are transmitted and distributed throughout the electronic assembly; (2) how a failure might manifest itself; (3) what the underlying root cause might be based on expected conditions. The answers to these questions can be found out by the synthesis of computer simulation, field failure information and accelerated test data , which provide information about failure sites, failure mode and failure mechanisms.

Once the dominant failure mechanisms are identified, a specified physics-based failure model can be developed to evaluate the time to failure for assembly parts. The model is usually based on the well recognized relations that are able

to capture the effect of the loading stresses on the damage accumulation in assembly parts. For example, Coffin-Manson relation is widely used in the lifetime prediction of wire bonds and solders joints, which characterizes the material performance in low-cycle fatigue situation. Paris' power law and Arrhenius equation is also frequently employed to describe the fatigue crack growth and account for the thermally activated mechanisms respectively.

Model parameter calibration makes just as critical a contribution to the development of an effective PoF model as the model expression. To achieve this end, it is necessary to characterize the evolution of the materials via conducting fundamental material tests with regard to the deformation elements included in the model. In the models, some deformation measures such as strain range and strain intensity factor can only be obtained with the aid of computer simulations. Alternatively, some damage metrics are linked to the parameters that can be directly measured. For example, in the physics-of-failure models for wire bonds and solder joints based on Coffin-Manson relation, loading temperature range is usually employed to account for the lifetime instead of strain range since the strain generated in the bonding materials is induced by the temperature variation when a power module is exposed to temperature swings.

Meanwhile accelerated tests are usually carried out for the collection of relevant lifetime data as well as the wear-out information. Through the comparisons of the input-output pairs between model simulation results and experimental data, the constants and exponents in the model can be justified by optimal curve fitting. Passive thermal cycling and active power cycling is the most frequently used reliability tests for evaluating lifetime of electronic components and validation of the physics-of-failure models.

The above procedures of development of PoF models for power electronic modules are illustrated in Figure 3.1.

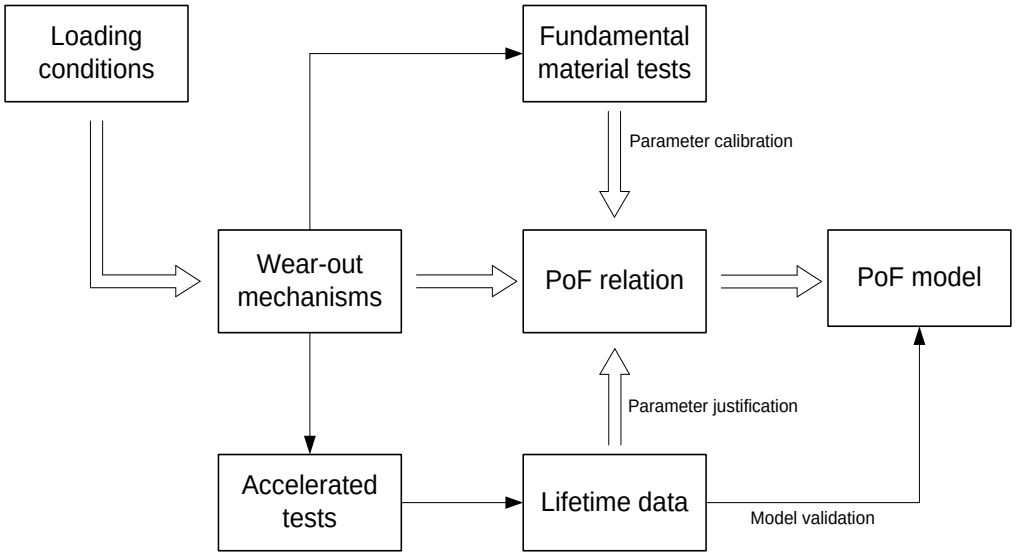

Figure 3.1: Procedures of the development of Physics-of-Failure models

Derivation of appropriate failure mechanism models is a prerequisite step for the successful implementation of PoF based reliability prediction and health management for power modules.

In the realm of reliability study for semiconductor device, physics-based approach has been used for many years with regard to the reliability physics of silicon devices. As a result, original PoF models characterize various failure mechanisms in the silicon devices such as hot carrier degradation, gate dielectric breakdown, electromigration and excessive intermetallization [70].

With the rapid evolution of the packaging technique for power semiconductor devices, stress-induced failures in the packaging materials make a significant contribution to the consequent reliability issues [71]. Understanding the performance of the packaging materials and interconnectors in these integrated components during operating life is crucial to the reliability design and assessment of the whole power module device. Therefore, more and more attention has been paid to the development of PoF models in the area of semiconductor packaging.

The primary reliability concern in power modules arises from the fact that they consist of materials with different thermal expansion coefficients, which causes thermal mechanical stress in adjacent layers under time-temperature exposure. In Chapter 2, it has been introduced that the most frequently observed package-related failure modes in power modules include solder joint degradation, substrate delaminating, wire bond lift-off and bond heel cracking. PoF modelling for power module interconnectors mainly focuses on solder joints and wire bonds as the critical reliability concerns.

This thesis concerns the development of PoF models for the lifetime prediction of wire bond interconnects. Firstly, an overview of the commonly adopted physics-of-failure models for wire bond interconnects in power semiconductor modules is presented in the following section. Some of the identified shortcomings are addressed based on some unusual observations, with a view to highlighting areas which require further understanding and investigation. Lastly, necessary modifications to existing methods are discussed raising the need for a new way of approaching wire bond lifetime assessment.

3.3 REVIEW OF THE PHYSICS-OF-FAILURE MODELS FOR WIRE BOND INTERCONNECTS

Wire bond failure is largely attributed to thermo mechanical fatigue caused by (1) repeated flexure of the wire (2) shear stress between bond pad and wire. These consequently induce vertical heel cracks or horizontal cracks at bonding interface. Crack propagation leads to the reduction in the joining area and hence the decrease of bond strength.

In the reviewed PoF based lifetime prediction models the change of strain/stress amplitude and the rate of crack growth are the frequently used physical parameters to indicate degradations. Accordingly, they are grouped under two broad categories which indicate their basis, i.e. thermal fatigue models and fracture mechanics based models. The strengths and weaknesses of

these categories are discussed, with the view to highlighting areas which require further understanding and investigation.

3.3.1. Thermal fatigue models

3.3.1.1 Plastic strain-based thermal fatigue models

The first thermal fatigue model developed for wire bond interconnects in power modules is based on plastic strain induced by temperature variation and CTE mismatch between wire material and semiconductor chip [72]. The model origins from Coffin-Manson relationship which defines a power-law relation between number of cycles to failure and the plastic strain induced per cycle for low cycle fatigue [73, 74]:

$$N_f = C_1(\Delta\varepsilon_{pl})^{-C_2} \tag{3-1}$$

Where:

N_f	is the number of cycles to failure
ε_{pl}	is the plastic strain induced per cycle
C_1 and C_2	are experimental constants

The value of plastic strain is usually estimated by finite element analysis or by numerical calculation as a function of wire loop curvature. This approach can provide a useful tool for comparative evaluations and parametric studies of different materials and geometries. But the corresponding model validation might be difficult as the plastic strain is not a straightforward parameter to measure in experimental tests. In [75], the predicted lifetime of gold wire bonds was compared with the experimental results in [76] although the temperature input to the FEA model was different from the test temperature range. In [77], a temperature cycling experiment was conducted by means of

liquid-to-liquid thermal shock to obtain a temperature variation from -40°C to 125°C. Here, strain was calculated for different bond loop geometries and a lifetime predicted for each case. Although the model produced the right trend, the cycles to failure it predicted were several orders of magnitude larger than the experimental results. The authors attributed the discrepancy between the lifetimes based on the calculated strains and actual wire bond lifetimes to the model not accounting for twisting and thinning of wires which would occur in real life. Furthermore, it was thought that the use of a power-law-based calculation led to further over-estimation of life.

In other instances, accelerated mechanical stress tests have been performed to simulate the equivalent strain induced stress generated by temperature fluctuation [78, 79]. Mechanical stress was applied by cyclic lateral displacement of one bonding foot while fixing the other. However, this is obviously an inadequate representation of the actual loading conditions during operation because thermo mechanical stress is not the only result from the temperature loads and the temperature induced effects are not taken into account.

3.3.1.2 Thermal fatigue models based on stress range

The above Coffin-Manson relation (Equation 3-1) is generally employed to characterize low-cycle fatigue where the stress is high enough for plastic deformation to occur. In certain applications where wire bonds suffer stresses below their yield stress (i.e. in the high cycle regime), the lifetime prediction is usually based on Basquin's equation [80, 81], in which stress range is used as damage metric instead of plastic strain amplitude as shown in Equation (3-2):

$$N_f = C_3 \cdot (\Delta\sigma)^{-C_4} \tag{3-2}$$

Where:

N_f is the number of cycles to failure

$\Delta\sigma$ is the stress induced per cycle

C_3 and C_4 are the material dependent constants

Hu and Pecht [82] presented four such stress-based lifetime prediction models for various failure mechanisms. A probabilistic approach has been employed to solve the uncertainty of temperature variation. However, the models are yet to be validated and only examples illustrating the application in the determination of dominant failure mechanism have been provided.

A similar model in [80] was validated by ultrasonic mechanical fatigue tests. Here, mechanical shear stress obtained by an ultrasonic resonance fatigue testing device working at a frequency of 20K Hz was believed equivalent to those induced during temperature/power cycling or operational life. The modeling results were compared with the lifetime prediction of wire-bonds proposed in [83] despite that the lifetime regime they dealt with was very different. Also the comparison was made between mechanical shear fatigue results and power cycling data. The mechanical fatigue results were in the region of 10^5 to 10^9 cycles to failure corresponding to an equivalent ΔT value between 30K and 60K while the minimum ΔT in the power cycling tests was about 70K. Although the lifetime curves have shown a good correlation, the deviations of the fatigue response in these two accelerated tests have been addressed. It has been pointed out that the factors such as temperature and strain rate dependent material properties could modify the fatigue response of materials and should be taken into consideration in the total fatigue lifetime modeling. Further investigation on the microstructural evolution of ultrasonically bonded aluminum wires has verified the difference of power cycling and accelerated mechanical loading.

In [81], modules were stressed with a pulsed DC current of up to 2.5A. Pulse length was between 10ms and 100ms at a duty cycle of 50%. Stress amplitude values were obtained from a 3D FE model. However, it is worth noting that the simulated temperatures under the given current loading conditions reached as

high as 700°C. This would suggest error at some level with the simulations.

3.3.1.3 Thermal fatigue models based on loading temperature range

Getting to the root, the thermo-mechanical stresses that wire bond interconnectors undergo during application are resulted from the strain when they are subjected to temperature swings imposed by harsh external environments, power dissipation in the silicon die as well as the ohmic heat generation in the wire itself. The strain is induced by mismatched coefficients of thermal expansion between the wire and the material to which it is bonded. The resulting thermal stress and equivalent strain can be expressed as a function of temperature swing.

$$\varepsilon = (\alpha_w - \alpha_c)\Delta T \tag{3-3}$$

Where:

ε	is mismatched CTE induced strain under temperature change
α_w and α_c	are the CTE of wire and semiconductor chip material respectively
ΔT	is the temperature swing

Accordingly, to relate fatigue lifetime to the loading temperature range ΔT, Equations (3-1) and (3-2) becomes:

$$N_f = C_5(\Delta T)^{-C_6} \tag{3-4}$$

Where:

N_f	is the number of cycles to failure
ΔT	is the temperature swing

C_5 and C_6 are the material dependent constants

In general, workers have found this model to accurately predict the lifetime of bond wires under thermal cycles where maximum temperature does not exceed 120°C [84]. In [85], IGBT devices with a single emitter bond wire were subjected to power cycles with a cycle period of 3 seconds. The degradation of the wire bonds were characterized by on-line monitoring V_{CE} during switching-off transient. Failure criterion was defined by 10% increase of V_{CE} with respect to the initial value. The maximum junction temperature was set below 100°C and ΔT was between 50K and 70K. Under this condition, the experimental data was fitted by Equation (3-4) with reasonable dispersion.

In [86], power cycling tests were conducted on power MOSFET devices. The minimum and maximum temperature varied from 30°C to 90°C and from 90°C to 150°C respectively. The obtained temperature swings were between 60K and 120K. Cycling period is in within 3 seconds and heat-up time was fixed to 1.8 seconds. Failure criterion was defined as 50% decrease of the initial shear force. Model parameters were derived by curve fitting experimental data to the Equation (3-4), which were stated only valid for the wire bonds under this investigation.

Therefore it is commonly accepted that larger thermal cycling ranges result in shorter lifetimes. This theory has been widely used to predict the lifetime of wire bonds and also applied as a basis for bonding reliability improvement [87, 88]. One such example is in [88], where it was suggested that rearranging the position of bond wires on the chip interface could reduce their ΔT and thus improve wire bond reliability.

3.3.1.4 Thermal fatigue models including mean temperature

It was proposed in [89] that in addition to ΔT, the absolute mean junction temperature T_m also had considerable influence on the lifetime characteristics of power modules. In this paper, power cycling tests were carried out at three mean temperatures (60°C, 80°C, 100°C) and ΔT values from 30K to 80K were presented (Figure 3.1). A Coffin-Manson relationship was used to describe the dependence of number of cycles to failure on temperature difference. The parallel shift for different mean temperature was assumed to be a simple thermally activated mechanism and was therefore expressed by an Arrhenius approach. The combination of two relations gave the Equation (3-5):

$$N_f = A \cdot \Delta T^{\alpha} \cdot \exp\left(\frac{Q}{R \cdot T_m}\right) \tag{3-5}$$

Where:

N_f	is the number of cycles to failure
T_m	is the absolute mean temperature
ΔT	is the temperature difference
A and α	are the experimental constants
Q	is the activation energy
R	is the gas constant

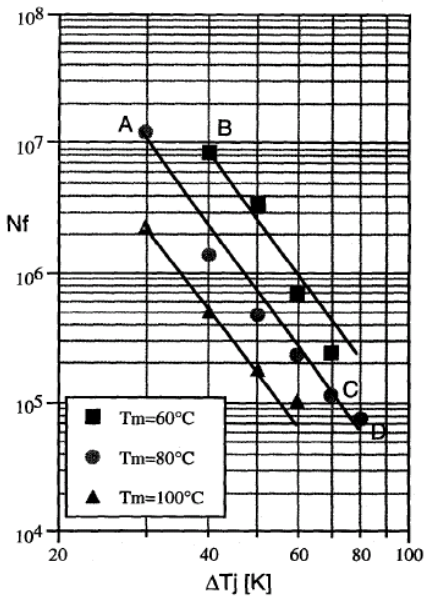

Figure 3.2: Number of cycles to failure as a function of ΔT_j with T_m as a parameter [89]

The model in [89] was originally developed to evaluate the reliability of the whole module, and has since been employed in the reliability assessment of whole modules made with advanced packaging technologies for extended temperature ranges [90-92]. Moreover, their analysis indicated that bond wire lifting occurred before thermal fatigue of solder joints if ΔT was less than 130 K, and hence wire bond failure was regarded as the dominant failure mechanism during power cycling. Therefore this relationship has been adopted by many researchers to evaluate the thermal fatigue lifetime for wire bonds [13, 93]. In [93], experimental validation was provided for equation (4) through fast thermal cycling tests with temperature swings from 50K to 110K.

Goehre *et al* [86] argue plausibly that this approach is not best suited to wire bond lifetime prediction as the investigation on the degradation of wire bonds is not separated from other failure mechanisms. This is because their own experimental results showed that shear force degradation rate was mostly dependent on the amplitude of the temperature cycling and a significant effect arising from different mean temperatures could not be identified [86].

3.3.1.5 Thermal fatigue models incorporating electrical stress

In addition to thermal loads, power devices inevitably suffer electrical stress during applications [94, 95]. In [95], failure mechanisms of a DMOS silicon device under thermal and electrical overload conditions were investigated.

The devices were stressed in a life test furnace with periodic overload current pulses. Furnace case temperature ranges from 85°C to 170°C. Peak power dissipation was in the range of 50~200W/mm^2. Pulse width was varied from 100 μs to 2000μs and repetition rate from 20ms to 2s, to obtain peak junction temperatures between 200°C and 350°C. Severe degradation of the metallization and wire bond lift-off was observed. Individual failure was characterized by drain-source breakdown or open circuit. FIB (focused ion beam) cross sections across the failed devices showed that failures generally occurred at the edge of the bond wedge which is the location of the highest (critical) current density in the metallization layer. For the lifetime prediction, Coffin-Manson Equation was modified to account for the failure mechanism which is based on metal degradation and bond lift-off driven by thermomechanical stress as well as electromigration, resulting in local overheating at the remaining bonded area. The modified model is expresses as Equation (3-6):

$$NTF = \frac{A}{S_{crit}^{2.2} \cdot \Delta T_j^{7.1}} \cdot \exp\left(\frac{0.58eV}{k \cdot T_{jave}}\right) \tag{3-6}$$

Where:

NTF	is the median number of cycles to failure
S_{crit}	is the critical current density
ΔT_{j}	is the change of junction temperature
T_{jave}	is the average junction temperature
A	is the material constant

This approach combines electro-migration contributions with mechanical fatigue. However, in practice devices are rarely subjected to the kind of extreme overload conditions described in [95]. On the other hand, it was indicated in this paper that static electrical stress at currents and temperatures comparable to those applied during periodic simultaneous overload pulses (12A, 220°C) caused no visible traces of electromigration and metal degradation after 72 hours. It was then concluded that the observed metal degradation during periodic overload operation of DMOS power switches is the result of electrical and dynamic thermal stress.

3.3.2 Fracture mechanics based models

Another lifetime modeling method for estimating the thermal fatigue life of wire bonds is based on fracture mechanics. Fracture mechanics quantifies the conditions under which a load-bearing body can fail due to the growth of a dominant crack. Previous application of this engineering discipline is to address the fracture behavior of large dimensional scale such as bridge and machine parts. Then it is employed in the PoF reliability modeling for newly emerging material systems, for example, microscale electronic components, by evaluating the growth rate of the crack.

3.3.2.1 Fracture mechanics models based on strain intensity factor

An early attempt to apply macroscopic fracture mechanics to life prediction of micro scale electronic components was made in [96]. Prediction was made on the fatigue crack growth in wire bonds. Crack growth per cycle is regarded to be governed by a stress or strain intensity factor, which controls the magnitude of the stress near the crack tip.

Experimental results of the lifetime of wire bonds subjected to on/off current cycling were compared with predictions made using macroscopic fracture

mechanics. The scatter in the experimental results was explained by variations in the initial defect size and thus suggested that the fracture mechanics predictions are a reasonable representation of the experimental results. The conclusion made in this paper was that fracture mechanics using macro material properties is valid for damage tolerance analysis on the microscale.

In this kind of fracture mechanics models based on strain intensity factor, Paris' Law is generally employed to relate crack growth rate to strain density factor:

$$\frac{da}{dN} = C(\Delta K_\varepsilon)^n \tag{3-7}$$

Where:

$\frac{da}{dN}$	is the crack growth per cycle
ΔK_ε	is strain density factor range
C and n	are material constants

The constants can be determined by comparing calculated and measured crack length. The strain density factor range is calculated with respect to temperature load by finite element method. A critical crack length is selected as the criterion to estimate the number of cycles to failure. This type of model is mostly applied to crack propagation along the bonding interface.

In a more recent paper [97], the fatigue lifetime of IGBT modules under small temperature ranges was investigated by this method. Temperature swings from 30K to 100K were set up in power cycle tests. The experimental results showed that the remaining bonded length reduced more rapidly for the bonds subjected to larger temperature ranges. The simulated thermal fatigue lives for these temperature ranges agreed well with the experimentally measured ones. The experimental results showed that the remaining bonding length decreased not significant (from the original 1000μm to 600μm) after 1.5×10^6 cycles at

ΔT=30K. It was then extrapolated that fatigue lives for loading cycles with ΔT values less than 30K, would be virtually infinite. However, this assumption was not experimentally verified and would seem unlikely.

3.3.2.2 Fracture mechanics models based on rupture driving energy

In [98], a fracture mechanics model was derived based on the opinion that crack growth rate depended on the energy balance between the elastic strain energy released during crack growth and the energy required to create new crack surface area. The driving force for de-bonding was expressed in the form of strain energy release rate as a function of wire material parameters and loop geometry.

$$G = \frac{3}{8} E h^3 \left(\frac{\Delta H_L^2}{a^4}\right) \tag{3-8}$$

Where:

G	is the strain energy release rate
E	is the elastic modulus of the wire material
h	is the wire diameter
α	is half the length of the bonding wire loop
ΔH_L	is the local out-of-plane deformation of the wire bond under applied loads measured at loop midpoint

The range of energy release rate ΔG is calculated with respect to the load range. The relationship between the rate of crack growth per power cycle $\frac{da}{dN}$ and ΔG was obtained from the literature [9] which was originally achieved for the study of interface fatigue crack growth for Al/Al_2O_3. The prediction by this model was made only for one loading condition (ΔT_j = 15°C) and this single

prediction point was the only one on the experimentally determined lifetime trend line.

3.3.2.3 Fracture mechanics models based on dissipated energy density

In [100], heel crack failure in aluminium ribbon has been studied. An approach based on the estimation of the plastic strain energy was proposed to predict the ribbon lifetime during power cycling.

$$N_f(I) = \frac{w_{pl}^{cr}}{w_{pl(I)}} \tag{3-9}$$

Where:

$N_f(I)$	is the life time
w_{pl}^{cr}	is the plastic strain energy density accumulated in a ribbon during its life
$w_{pl}(I)$	is the dissipated energy for one ribbon corresponding to the current (I) in a stabilized cycle

The electro-thermal response of the ribbon was studied for current levels ranging from 30A to 80A per ribbon (200mm×2μm). Electro-thermal FEA was carried out to derive the temperature profiles. The temperature variation on the top of the ribbon loop was about 300°C for an 80A current. The dissipated energy density per power cycle was also obtained from FEA. Then the estimated lifetime results were compared with Coffin-Manson predictions and the authors deemed there to be good agreement between the two. However, although the approach produced a similar trend as the Coffin Manson model, there were significant deviations between the predicted lifetime points. Furthermore, the energy-based estimations were not experimentally validated.

3.4 SOME PHENOMENOLOGICAL CONSIDERATIONS FOR WIRE BOND LIFETIME MODELLING

On the whole, in the existing models discussed, lifetime is generally accounted for by the loading amplitude alone, although this is represented in various forms. They share the common view that wire bond failure is the outcome solely of damage accumulation during repeated heating and cooling and the effect of duration of exposure to the temperature loads is not addressed. Therefore the lifetime predictions made by these models lead to a common result that the number of cycles to failure decreases as the loading temperature range increases.

However a few findings on the reliability of aluminium wire bonds during extended thermal cycling ranges have raised a number of interesting issues of wire bond lifetime modelling.

In [15, 17], the wear-out behaviour of high purity aluminium wire bonds under passive thermal cycling exceeding 125°C was reported. Measurements of the bond shear strength showed that the bonds subjected to higher maximum cycling temperature ($T_{\max}$) had slower wear-out rates despite having been exposed to larger temperature ranges (ΔT) (Figure 3.3). Investigations of the fine scale microstructure and hardness of the bond wires showed noticeable softening and subgrain coarsening during thermal cycling regimes with high T_{max} values. In [17], the effect of peak temperature is considered by comparing 5N wire bonds subjected to two different thermal cycling regimes, namely -55°C to 125°C and -60 to 170°C. Nanoindentation hardness measurements have been made on a number of bond interfaces. A series of 15 hardness values was obtained for each wire bond. Statistical analyses were performed to determine the influence of temperature range and peak temperature on softening behaviour. H_{50} values are determined as 0.53 GPa and 0.47 GPa respectively after 1000 cycles (see Figure 3.4). This means that the wire bonds which were subjected to the lower T_{max} cycle (-55°C to 125°C) are notably harder than those cycled from -60°C to 170°C. Softening is the first stage of

annealing process. The comparison result has indicated that the more significantly annealed wire bonds exhibited a slower wear-out rate.

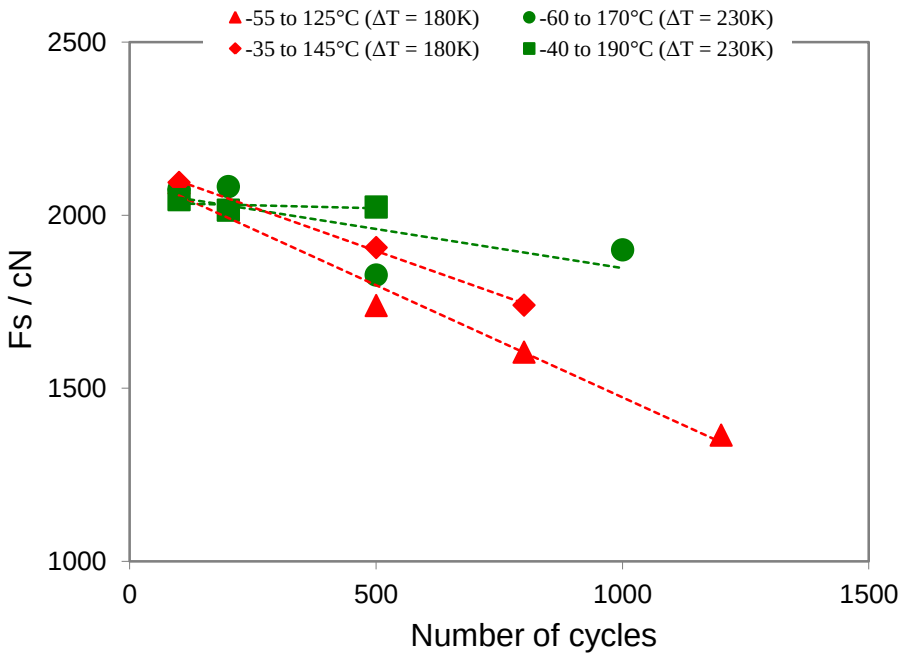

Figure 3.3: Effect of increasing number of cycles on mean shear force [17]

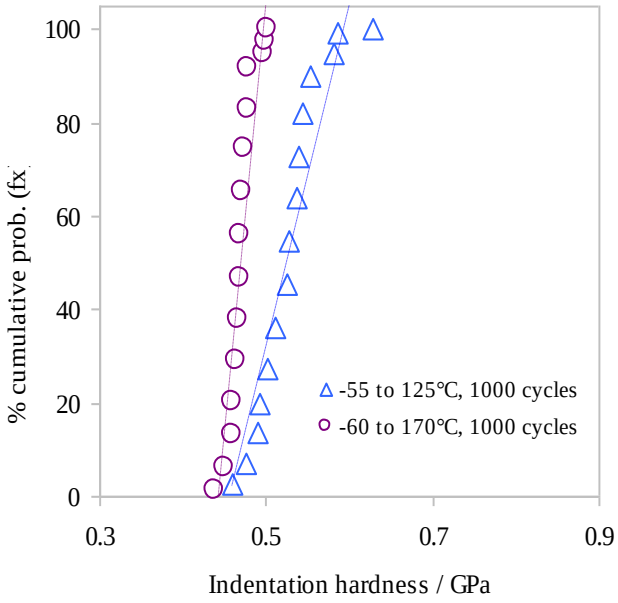

Figure 3.4: Nanoindentation of interfacial region of Al wire bonds — effect of ΔT and T_{max} [17]

In [17] Focused ion beam (FIB) channelling images of 5N pure aluminium wire are provided for the bond interface of an as-bonded wire and wires subjected to thermal cycling under the regimes of -55°C to 125°C and -40°C to 190°C (Figure 3.5~ 3.7). The bonds subjected to the low T_{max} value of 125°C show comparatively refine grains after 500 cycles compared with those subjected to a T_{max} of 190°C.

Coincidentally, the bonds subjected to the low T_{max} value of 125°C wear out faster than the bonds subjected to a T_{max} of 190°C. It was explained that a maximum cycling temperature of 125°C might be too low to offset these hardening phenomena significantly. These experimental observations have demonstrably shown the influence of the high temperature phenomena on the bond degradation behaviour.

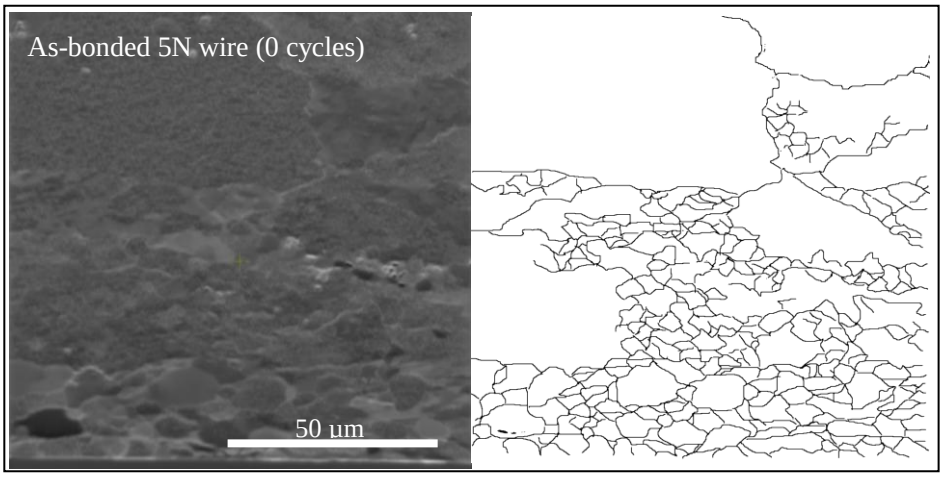

Figure 3.5: FIB channelling image (and corresponding transcribed grain boundary outline) of a 5N pure Al wire bond interface prior to thermal cycling (as-bonded) [17]

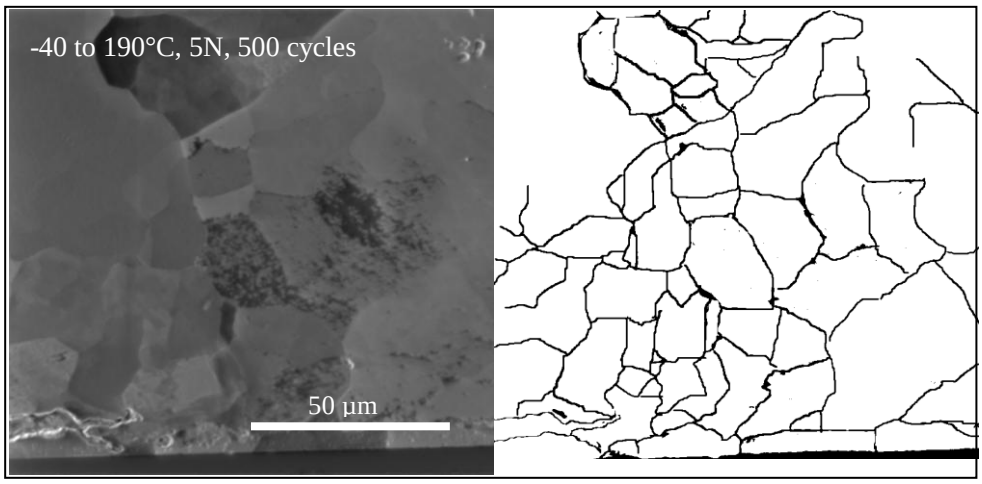

Figure 3.6: FIB channelling image (and corresponding transcribed grain boundary outline) of a 5N pure Al wire bond interface subjected to 500 thermal cycles from -40 to 190°C [17]

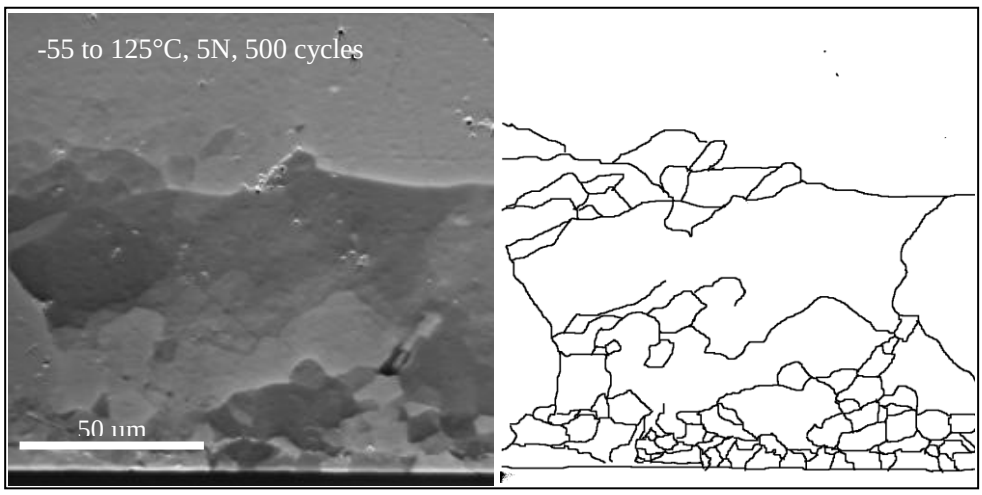

Figure 3.7: FIB channelling image (and corresponding transcribed grain boundary outline) of a 5N pure Al wire bond interface subjected to 500 thermal cycles from -55 to 125°C [17]

Findings in [16] on the reliability of thick aluminium wire bonds under three extended thermal cycling ranges, namely -40 to 150°C, -40 to 200°C and -40 to 250°C are also in agreement with these observations. Here, their experimental results showed that despite large differences in temperature range of thermal cycle tests, the residual bond lengths of Al wires bonded on Si chips appeared almost the same (Figure 3.8); in other words, the rate of crack propagation was unaffected by ΔT.

Moreover, EBSD (Electron Backscatter Diffraction) images of wire material revealed that recrystallization and grain growth had progressed during the thermal cycling tests. Compared with the highly deformed and refined grains in the as-bonded condition, the grains coarsened noticeably in the course of thermal cycling and the extent of recrystallization was particularly pronounced in those exposed to higher peak temperatures. Recrystallized microstructure at elevated temperature has also been reported by other investigators. In [80], a certain degree of recovery of coarse grains within the bonded area was observed when bond specimens were subjected to isothermal shear mechanical loading at 80°C.

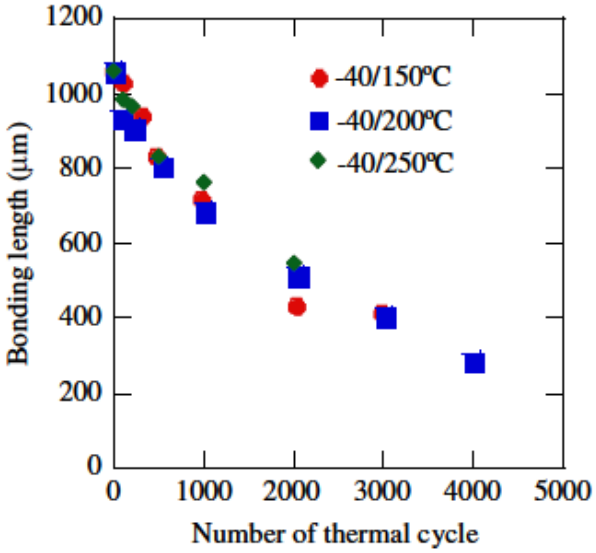

Figure 3.8: Residue bonding length of Aluminium wires during thermal cycling [16]

Also in [14], the effect of maximum temperature was investigated by varying it from 105°C to 300°C whilst keeping ΔT at a constant 80K. Although a decrease in lifetime was observed for T_{max} values between 105°C and 200°C, no major change in fatigue characteristics of wire bonds was observed for T_{max} values between 200°C and 300°C (Figure 3.9).

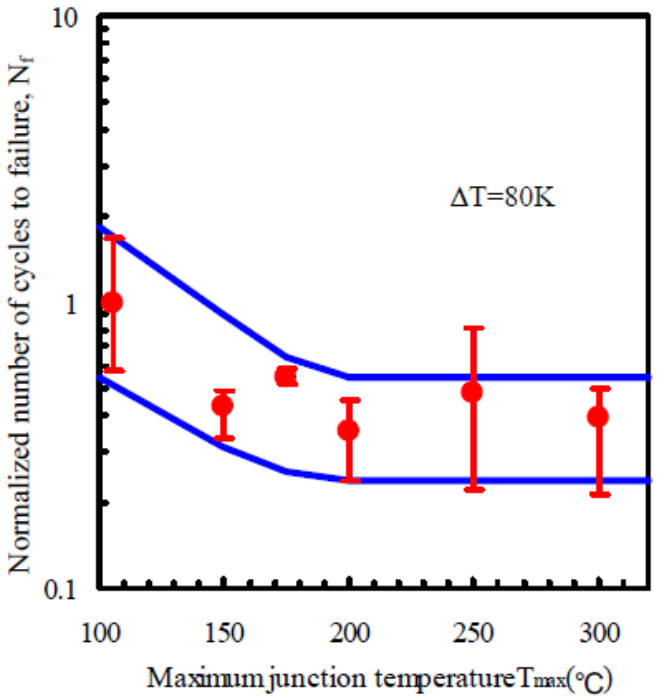

Figure 3.9: Relationship between N_f and maximum junction temperature [14]

It is not difficult to extract several common findings from these unusual observations: (1) when maximum peak temperature is high enough, the bonds exposed to the larger temperatures range either showed little difference [14] [16] or a slower deterioration rate [15] compared with those exposed to smaller temperature ranges. This apparently contradicts Coffin-Manson predictions. (2) Evidently, thermally activated processes occur during thermal cycling and are more significant at higher temperatures [15] [16] [80].

Since grain coarsening might be attributed to dislocation annihilation [101], and softening is caused by a reversal of plastic strain [102], it was concluded by the authors in [15] that 'damage removal' and damage accumulation occur in tandem during thermo mechanical cycling, and that the seemingly anomalous trend in bond degradation observed could be due to a dominance of the former at high enough temperatures. A logical conclusion, then, would be that physics-of-failure models for wire bonds which only account for damage accumulation are not adequate for all mission profile scenarios.

With this in mind, a damage-based prediction methodology was put forward in [15] to predict degradation rate of the bond shear force by introducing a variable D_1 to account for damage removal during exposure to elevated temperatures:

$$\beta = \frac{D_1}{A\Delta T^{-M}} \tag{3-10}$$

Where:

β	is degradation rate of the bond shear force
D_1	represents the proportion of damage remaining after a single thermal cycle
A and M	are numerical constants usually determined experimentally
ΔT	is loading temperature variation

Although this model innovatively attempts to take account of the aforementioned damage removal effects on the bond degradation rate, the Coffin-Manson expression still forms the basis of its calculation of the damage which builds up during temperature cycling. Moreover, since the derived expression for D_1 is only valid for one particular temperature-time profile, this model cannot be readily extended to an arbitrary temperature-time profile.

Thus far, all of the models reviewed have been developed under the assumption that the bond wire is subjected to regular cyclic loading. In reality, however, power modules are usually subjected to irregular time varying loads, either as a consequence of environmental changes or load cycling. Although the Rainflow counting method can be used to convert irregular time series into a sequence of cycles, this counting algorithm uses just the extreme points of the loads [103]. In [82] a probabilistic approach was employed to include the uncertainty of the temperature variation, but it just used a probability density

function to statically account for the temperature range history. In essence, cycle-based modelling methods are too simplistic and cannot readily describe the impact of time-at-temperature on the bond wear-out behaviour.

3.5 SUMMARY

In this chapter, the procedure for developing physics-of-failure models has been presented. It also included a literature review of the existing physics-of-failure based life prediction methodologies. The review has been focused on wire bond interconnects in power modules. Some of the identified shortcomings and limitations of the existing cycle-based lifetime prediction models are addressed by reference to some unusual observations from both our own experiments and those reported in the literatures.

These phenomenological considerations highlight the need for new approaches to wire bond life prediction models and thus bring about the onward development of time-domain models that can more accurately reflect the observed temperature-time effects and related phenomena. The new time-domain damage model is expected to be able to account for the combined effect of damage removal and accumulation processes and also can represent the impact of time-at-temperature on the bond wear-out rate. A proposal for this new damage-based crack propagation model is presented in the next chapter.

CHAPTER 4

A TIME-DOMAIN DAMAGE BASED CRACK PROPAGATION MODEL

4.1 INTRODUCTION

The extent and rate of wire bond degradation depends on both the magnitude and duration of exposure to the loads. In the existing physics-of-failure based models for wire bond interconnects, lifetime is usually accounted for by loading amplitude alone. Even in cases where the mean temperature is taken into account, the models are derived based on a regular thermal cycle of a known duration. The effects of irregular loading and time at temperature effects are not addressed, leading to substantial errors under extended thermal cycling at high temperature. Accurate modelling of all of the relevant effects requires a phenomenological approach which can provide an insight into the microscopic mechanisms that act to cause a change in the macroscopic mechanical properties in wire materials.

In this chapter, a time-domain damage based crack propagation model is proposed and described in full details. The new approach which discards the usual cycle-dependent modelling methodology in favour of a time domain representation is believed to address some of the discussed limitations. This modelling methodology is intended to estimate the bonding interface damage condition at regular time intervals through a damage model which includes the effect of thermally activated processes on the bond degradation behaviour. Other underlying factors which vary for different materials and which

influence the build-up of damage, such as stacking fault energy are also taken into account implicitly by the incorporation of a work hardening term. Thus the impact of time at temperature and other rate sensitive processes on the bond degradation rate can be accurately represented. This way, the model accounts not only for the damage accumulation processes but also the damage removal phenomena and is able to catch the wear out characteristics under the loading conditions with arbitrary temperature-time profiles.

4.2 OVERVIEW OF PROPOSED MODEL

Figure 4.1 (a) shows a schematic graph of an as-bonded wedge bond. Prior to thermal cycling, bonded wires contain a certain amount of damage that is brought about by deformation-induced work hardening as a result of the ultrasonic energy and force used in the formation of the bond [118, 119]. During service period, wire bonds are subjected to the temperature fluctuation due to harsh environment exposure and power dissipation in the semiconductor device. The mismatch in thermal expansion coefficient between the wire material and semiconductor device on which they are bonded facilitates the accumulation of plastic strain that generates thermo mechanical stress at the bonding interface leading to crack initiation and growth. As-bonded wires often contain pre-existing heel cracks because of the wire flexure due to loop formation during ultrasonic wedge bonding. Stress is concentrated in the area around crack tip. As the stress increases, plastic deformation occurs by the movement of dislocations that are the linear defects in crystals. The dislocation density increases drastically during plastic deformation and there is accumulation of material damage at the atomic level, through the pile-up of dislocations.

During repeated heating and cooling, damage accumulates at the crack tip and moves into the wire material to form a plastic zone (see Figure 4.1(b)). The plastic zone moves along the interface as crack propagates. Failure results

when cumulative damage at the sites of stress concentration exceeds the endurance limit of the material.

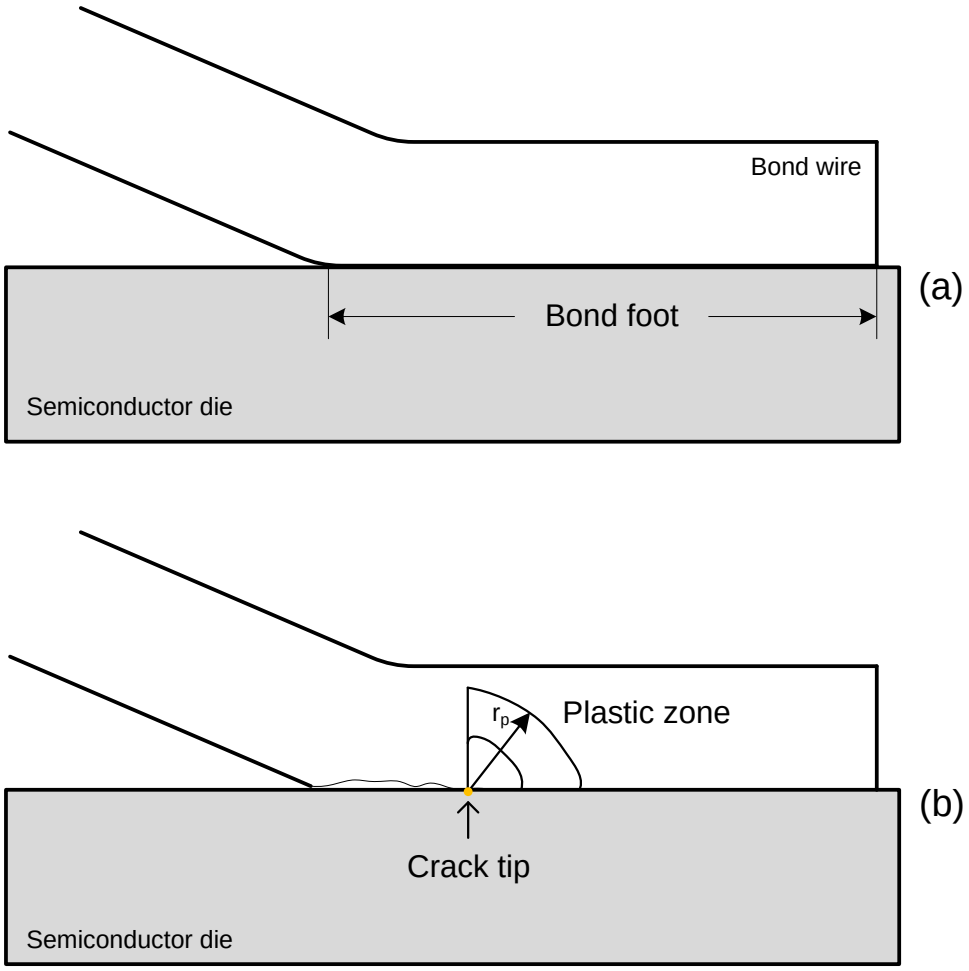

Figure 4.1: Schematic graph of a wire bonded on a semiconductor die (a) As bonded wire (b) With a crack propagating along the interface

In the proposed model, a variable *D* is used to represent the 'damage' condition in wire materials, i.e. the build-up plastic deformation. It is defined as a function of time and position through a differential equation which includes the effects of time and temperature-dependent material properties.

Strain hardening due to accumulation of dislocations and softening due to recovery and recrystallisation occurs concurrently in bonding wire materials

during temperature fluctuation [104]. Work hardening behaviour of the material is represented by a damage accumulation term. Moreover, work hardening is influenced by temperature [105] and dynamic recovery which takes place during thermal cycling [106, 107], evidenced by softening and subgrain growth. Such thermally activated processes are also represented in the model via a damage removal term.

The differential damage model assumes that the incremental damage $\delta D(y, \delta t)$at any point along the interface can be described by the following general expression. The position at the bonding interface is represented by *y*.

$$\delta D(y,\delta t) = \underbrace{f(D,\varepsilon,T)}_{\text{Damage accumulation}}\delta T - \underbrace{\alpha(D,T)}_{\text{Damage removal}}\delta t \qquad \textbf{(4-1)}$$

Where:

D	is the damage condition in the wire material
y	is the distance from the bond origin
ε	is the local strain and is a function of position and time
T	is the loading temperature as a function of time
t	is the time

The first term expresses the accumulation of damage that occurs as the result of an incremental change in loading temperature which is the driving factor. The second term accounts for diffusion driven processes such as annealing and creep. For these thermally activated processes, exposure time is a crucial factor therefore a time derivative is included.

The total interface damage at each time instant can be calculated by the integration of the damage for all the points along the bonding interface from the crack tip. The boundaries of the integration interval are defined by the

length of the initial bond foot L and the crack length l, which indicates the residual bond length.

$$D_T(t) = \int_{y=l}^{y=L} D(y,t)dy \tag{4-2}$$

The accumulation of damage in wire material which takes place under temperature loads manifests itself macroscopically through crack growth. Therefore crack growth rate can be represented by a function of total interface damage, and the rate of change of total damage, i.e.:

$$\frac{dl}{dt} = f(D_T) + g\left(\frac{dD_T}{dt}\right) \tag{4-3}$$

Where

D_T is the total interface damage

l is the crack length

Shear force is a commonly used parameter to quantify the bond degradation condition, which can be empirically obtained for a given thermal cycling range. Crack propagation along the bonding interface results in a reduction in the welded area leading to decrease of the bond shear strength. The magnitude of shear force F_s can therefore be determined by the ration of the residual bond length to the initial bond foot length.

$$F_s = \left(\frac{L-l}{L}\right) F_0 \tag{4-4}$$

Where

F_0 is the initial shear force

L is the initial bond length

The bond is regarded as failure when the shear force reduces by a certain percentage of the initial value. Then the time to failure of the wire bonds can be estimated by applying the specific failure criterion.

Above all, the development of the differential damage model (Equation 4-1) is the core of the whole damage-based crack propagation modelling methodology. The following sections describe the basic definitions of the constituent functions of the damage model and go into the implementation details as well.

4.3 DEFINITION OF THE DAMAGE MODEL

In Equation (4-1), the first term on the right side *f (D, ε, T)* accounts for the build-up of the damage and the second term *α (D, T)* represents thermally activated damage removal processes. These two continuous functions are transferred into discrete counterparts through the concept of discretization. Therefore these two terms can be written as: $f(D,\varepsilon,T) = f_\varepsilon(\varepsilon)f_D(D)f_T(T)$ and $\alpha(D,T) = \alpha_D(D)\alpha_T(T)$. Therefore Equation (4-1) can be written in the form of Equation (4-5).

$$\delta D(y,\delta t) = f_\varepsilon(\varepsilon)f_D(D)f_T(T)\delta T - \alpha_D(D)\alpha_T(T)\delta t \tag{4-5}$$

The front view and top view of a bond foot cross-section are illustrated in Figure 4.2 and basic parameter definitions are provided.

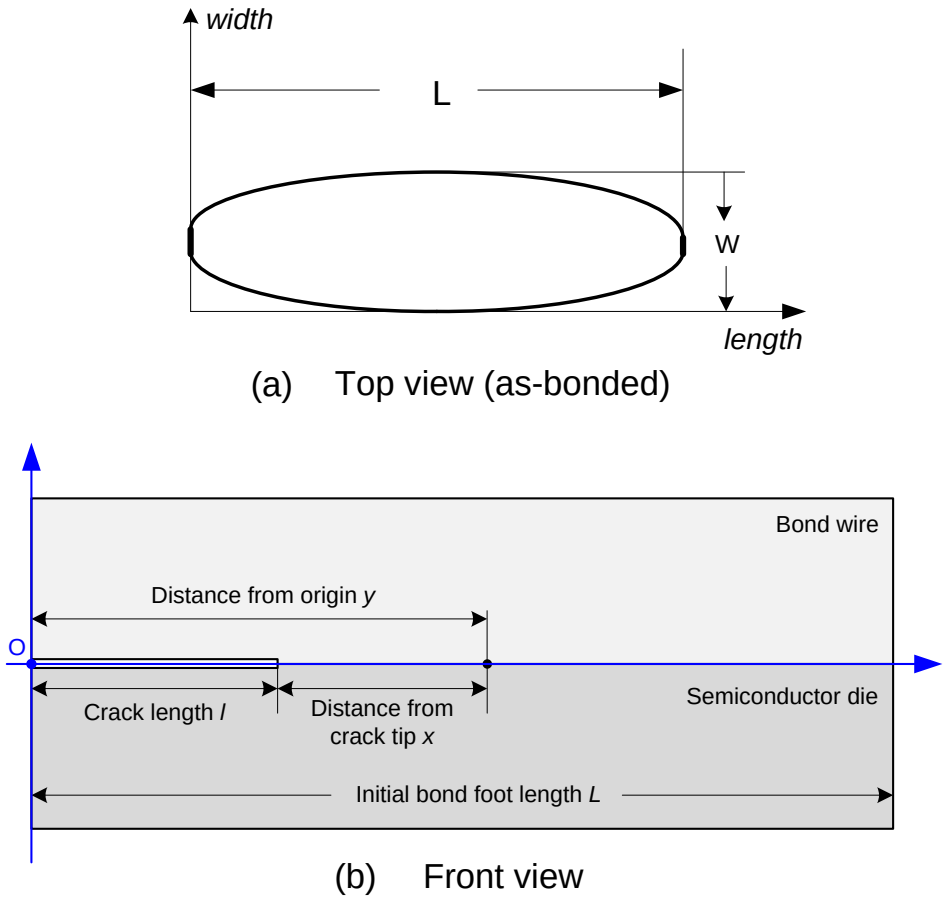

Figure 4.2: Cross-sectional diagram of a wire bond foot

4.3.1 Damage accumulation functions

- Spatial plastic strain distribution function $f_\varepsilon(\varepsilon)$

The spatial plastic strain distribution in the plastic zone is expressed by function $f_\varepsilon(\varepsilon)$ as: $f_\varepsilon(\varepsilon) = g\left(y - l, \varepsilon_p\right)$. The term $\varepsilon_p(t)$ represents plastic strain history, which is determined by the growth of the plastic zone. The extent of the plastic zone is assumed to be determined by interfacial displacement and a shape function that defines the stress/strain concentration. Propagation and development of the plastic zone as a function of time under cyclic and random loading will be described in the following paragraphs.

From the definition of the model parameters provided in Figure 4-2, it is known that $x = y - l$ is the distance from the crack tip. A weighting function $g(x, \varepsilon_p)$ is employed to represent the strain concentration factor with reference to the position along the bonding interface. Strain concentration is very high at the crack tip and decreases gradually away from the tip point [108, 109]. Thus the exponential decay function is applied to describe the strain distribution along the bonding interface.

That is,

$$f_\varepsilon(\varepsilon) = g(x, \varepsilon_p) = G_0 exp\left(-\frac{x}{\sqrt{LW}|\varepsilon_p|}\right) \quad (4\text{-}6)$$

Where:

L	is the initial bond foot length
W	is the initial bond foot width
G_0	is the damage coefficient
ε_p	is the plastic strain
x	is the distance from the crack tip

The term $\sqrt{LW}$ defines the approximate bond foot size scale. Parameter x defines the position at the bonding interface with respect to the crack tip.

- Work hardening function $f_D(D)$

$f_D(D)$ is a work hardening term which describes the damage accumulation in the wire material during thermal exposure. Work hardening refers to strengthening of a metal through plastic deformation. It is also called cold working because this is caused by plastic deformation at temperatures low enough that atoms cannot rearrange themselves. When metal wires are

plastically deformed at temperatures well below its recrystallization temperature which is typically below $0.3T_m$ (T_m represents the melting temperature in Kelvin), the number of dislocations increases drastically due to the formation of new dislocations. The more dislocations within a material, the more they will interact and become pinned or tangled. This will result in a decrease in the mobility of the dislocations and strengthening of the material. The increase of dislocation density leads to work hardening which hardens the wire material and meanwhile decreases its ductility. The ability to which the wire material can undergo plastic deformation before fracture is weakened. In other words, the work-hardened wire is more prone to failure. Increase in the number of dislocations is a quantification of work hardening.

Power law relationship is a common mathematical description of the work hardening phenomenon [120]. Accordingly, Equation (4-7) is applied to express the multiplication of damage by means of describing the cold work effect on the wire material.

$$f_D(D) = 1 + h(D) = 1 + \alpha_H D^{\beta_H} \tag{4-7}$$

Where:

α_H is the work hardening constant

β_H is the work hardening exponent

- Temperature hardening function $f_T(T)$

$f_T(T)$ is a temperature dependent damage term which defines the dependency of accumulated damage in the wire material on the loading temperature. Work hardening, i.e. the extent of plastic deformation, is influenced by the temperature to which the specimen is subjected. During cold working plastic deformation the multiplication of dislocations occurs at a faster rate than they are annihilated by dynamic recovery. The effects of cold working by accumulation of dislocations and the grain structure formed at high strain can

be eliminated by appropriate heat treatment (annealing) which promotes the recovery and subsequent recrystallisation of the material.

Equation (4-8) determines the ratio at which the damage changes in response to the loading temperature, assuming that generation and annihilation of dislocations reach equilibrium at temperature T_{eq}.

$$f_T(T) = \left(\frac{T_{eq}}{T}\right)^{\beta_T} \tag{4-8}$$

Where:

β_T is the temperature hardening exponent

T is the loading temperature

This function is interpreted in Figure 4.3. When the loading temperature T is below T_{eq}, the value of $\frac{T_{eq}}{T}$ is bigger than 1 so the temperature load at this time instant has the cumulative effect on the value of the damage. On the contrary, when T is above T_{eq}, the value of $\frac{T_{eq}}{T}$ is smaller than 1 that results in the damage removal effect. Therefore by tuning parameter β_T, the fluctuation rate of the damage can be adjusted.

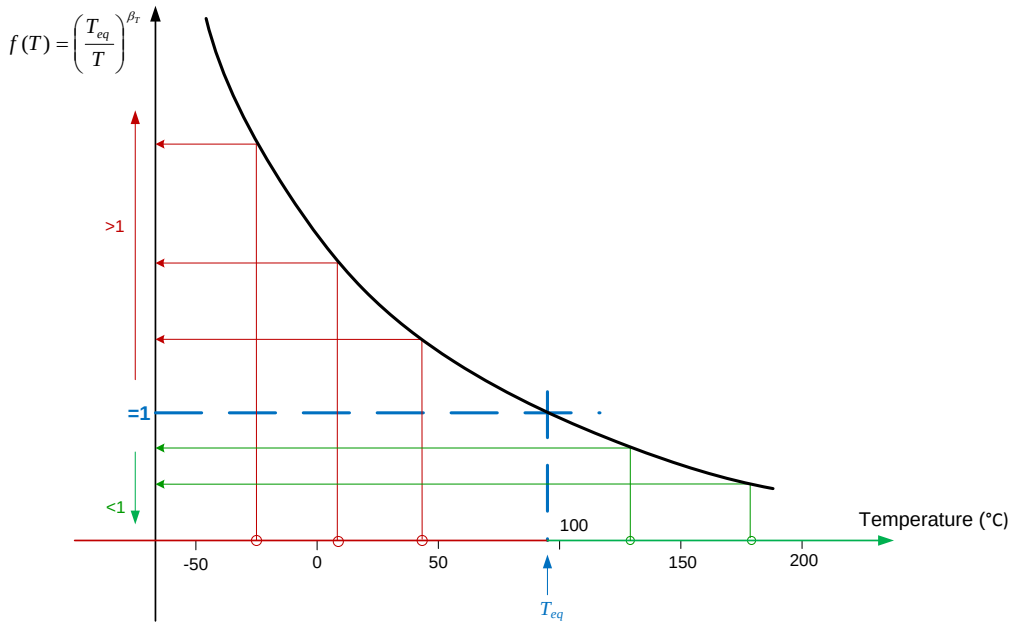

Figure 4.3: Illustration for temperature hardening function

- Temperature driven deformation function δT

In terms of the final expression of the damage model, δT is represented by temperature driven displacement strain ε_d due to the mismatched thermal expansion coefficient of the two bonded materials, assuming that the two bonded materials had the same length at the equilibrium temperature T_{eq}, i.e.:

$$\delta\varepsilon_d = \Delta CTE\left(T - T_{eq}\right) = (\alpha_{Al} - \alpha_{Si}) \cdot \left(T - T_{eq}\right) \tag{4-9}$$

Where:

α_{Al} is the thermal expansion coefficient of aluminium

α_{Si} is the thermal expansion coefficient of silicon

For the implementation, the absolute value of incremental displacement strain $|\Delta\varepsilon_d| = |\Delta CTE(T - T_{eq})|$ is used since damage accumulates irrespective of the direction of change in plastic strain.

4.3.2 Damage annihilation functions

When strain hardened materials are exposed to elevated temperatures, it facilitates the return of the cold worked metal. There are three stages in the annealing process. The first recovery phase results in softening of the metal through removal of crystal defects (primarily the linear defects i.e. dislocations) and the internal stresses which they cause. The second phase is recrystallization, where new strain-free grains nucleate and grow to replace those deformed by internal stresses [110]. If annealing continues after recrystallization has been completed, the grains begin to grow in size, in which the microstructure starts to coarsen.

Investigations on indentation hardness and fine scale microstructure of aluminium bond wires showed noticeable softening and subgrain coarsening during thermal cycling regimes with high maximum temperatures [17]. Hardness (i.e. resistance to deformation under a constant load) can be correlated with microstructural parameters such as dislocation density, grain size, and secondary phase particles, and therefore creep behaviour [111]. It was thus believed that these annealing phenomena annihilated some build-up dislocations, thus relieving the bond area of stress/strain and offsetting the overall rate of damage accumulation.

The degree of restoration depends on the temperature, the amount of time at this temperature and also the amount of work hardening that the material experienced. Therefore two terms are included to describe the damage annihilation processes.

- $\alpha_D(D)$ represents the amount of existing damage in the bonding material

- $\alpha(T)$ is an annealing term to describe the damage healing processes, i.e. annihilation of the dislocations by dynamic recovery. Arrhenius equation is widely adopted to represent the temperature effect on the reaction rate which is applied to express the temperature dependence of the damage annihilation rate.

$$\alpha(T) = k_2^{'} exp\left(-\frac{Q}{RT}\right) \cdot \delta t \tag{4-10}$$

Where:

Q is the activation energy

R is the gas constant

k_2' is an annealing coefficient

δt is the time step

With the definition of each function, the differential equation (4-5) is expressed as:

$$\delta D(y, \delta t) = G_0 exp\left(-\frac{y-l}{\sqrt{LW}|\varepsilon_p|}\right) \cdot \left[1 + \alpha_H D^{\beta_H}\right] \cdot \left(\frac{T_{eq}}{T}\right)^{\beta_T} \cdot |\delta\varepsilon_d| - D \cdot k_2^{'} exp\left(-\frac{Q}{RT}\right) \delta t \tag{4-11}$$

4.4 IMPLEMENTATION OF POSITION-DEPENDENT DAMAGE MODEL

At this point, a position-dependent damage model can be achieved, by which the interface damage is expressed as a function of both position and time. For the model implementation, the bond foot interface is divided into several x-steps. For each cell index x_i, the values of damage are propagated from one time-step to the next as follows:

$$D(x_i, t_j) = G_0\, exp\left(-\frac{x_i}{\sqrt{LW}|\varepsilon_{pj}|}\right) \cdot \left[1 + \alpha_H D(x_i + \Delta l_{j-1}, t_{j-1})\right]^{\beta_H} \cdot \left(\frac{T_{eq}}{T}\right)^{\beta_T} \cdot |\Delta CTE(T - T_{eq})| + D(x_i + \Delta l_{j-1}, t_{j-1}) \cdot \left[1 - k_2' exp\left(-\frac{Q}{RT}\right)(t_j - t_{j-1})\right] \tag{4-12}$$

In this position-dependent damage model, three terms including plastic strain ε_{pj}, incremental crack length during the last time step Δl_{j-1} and the corresponding damage value need to be solved. In this section, the implementations of these three terms are explicated.

4.4.1 Modelling plastic strain history

Upon heating and cooling, the bonding materials expand or shrink by some factor. The mismatch in thermal expansion coefficient between the wire material and semiconductor device causes shear stresses at the bond interface. Stress concentration leads to the formation of a plastic zone close to the crack tip in which damage accumulates. The value of plastic strain ε_p is calculated

from the displacement strain ε_d assuming no elastic range and a strain direction reversal model which governs the initiation and growth of plastic zones.

In the next paragraphs, propagation and development of the plastic zone as a function of time under cyclic and random loading is described first. Determination of the plastic strain that is associated with the active plastic zone follows.

4.4.1.1 Propagation and development of plastic zone

The size of the plastic zone depends on the applied load and the sign of the rate of change. Figure 4.4 illustrates the growth of the plastic zone as a function of time. It is supposed that the stresses generated by expansion and shrinkage of the bonding materials are not cancelled by each other. On the contrary, they build up strain at opposite direction. In other words, at each strain reversal a new zone is initiated at the crack tip (points A, B) which grows until it overwhelms any prior zone of opposite sign such as at point D. At this point the enlarging zone encroaches on an underlying zone of the same sign. The zones are assumed to coalesce and the zone edge "jumps" to the edge of the underlying zone as indicated at point D.

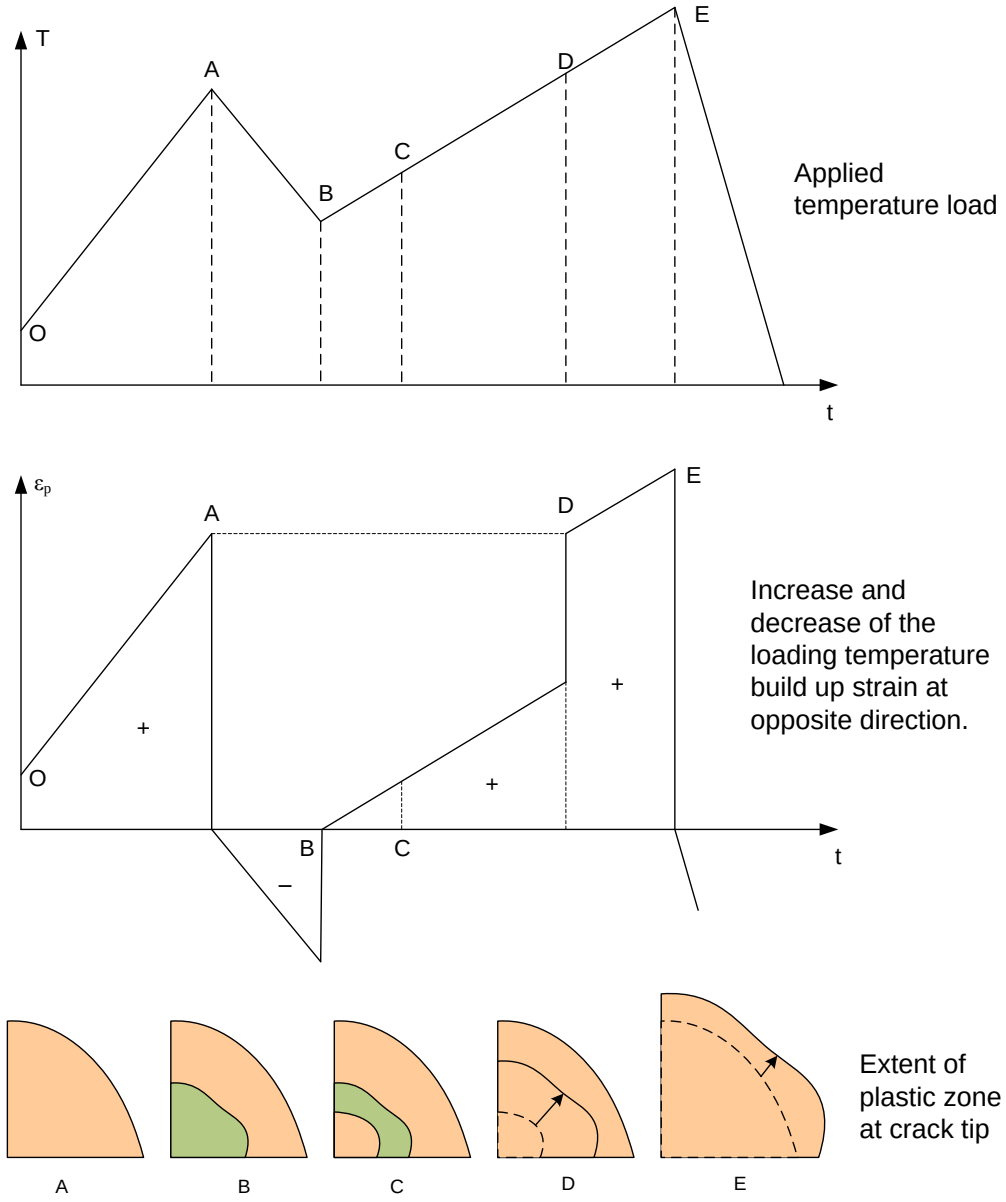

Figure 4.4: Evolution of plastic strain history assuming no elastic region

4.4.1.2 Evolution of plastic strain history

The plastic strain is obtained by reference to the development of the plastic zone with respect to each incremental strain. The implementation procedures are illustrated by the flow chart shown in Figure 4.5.

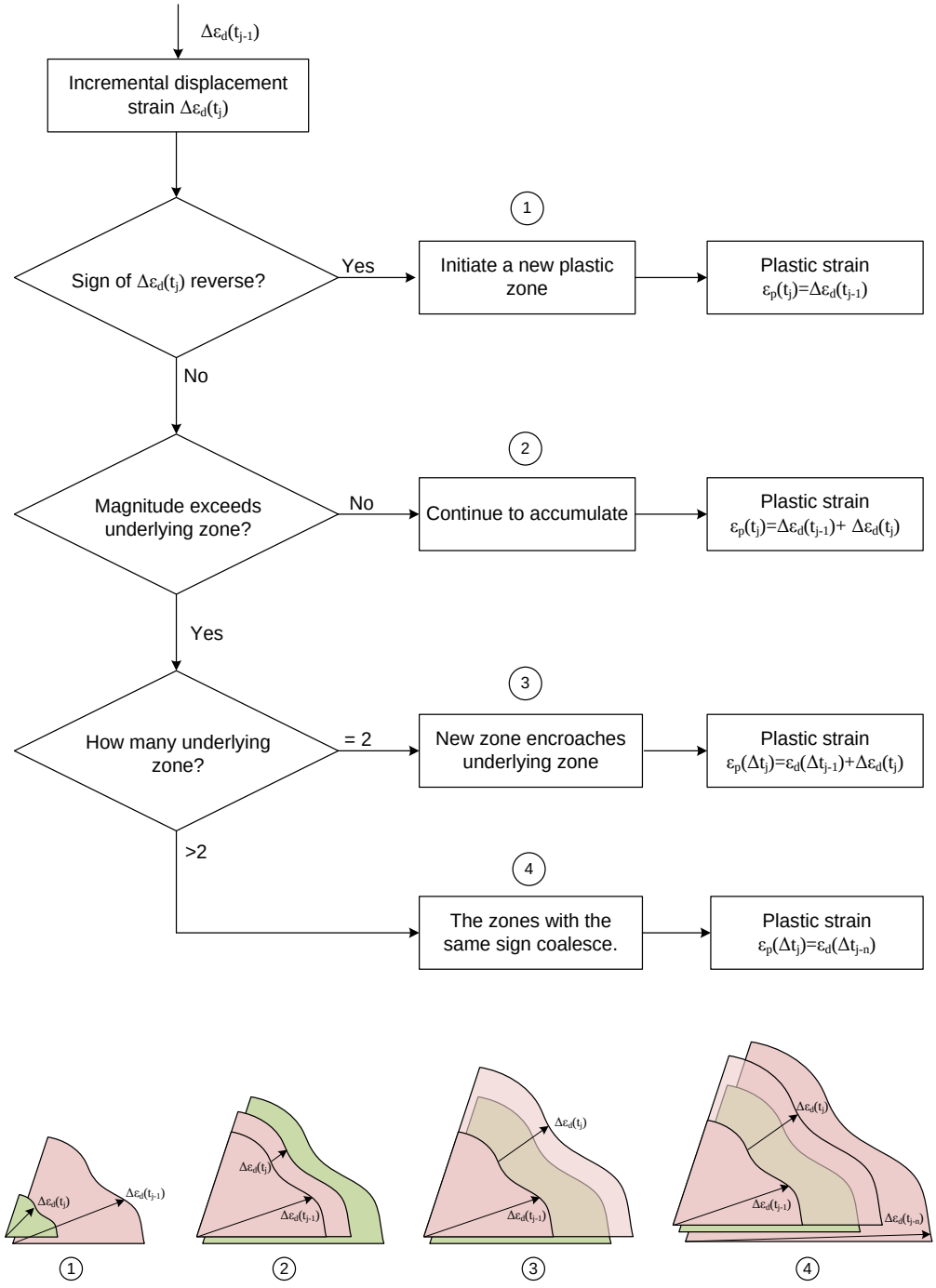

Figure 4.5: Determination of plastic strain history

For any time step t_j, the incremental displacement strain $\Delta\varepsilon_d(t_j)$ is compared to $\Delta\varepsilon_d(t_{j-1})$ during the last time step t_{j-1} which has formed a plastic zone. If the direction of the incremental stain reverses, a new plastic zone is initiated and

the plastic strain ε_p is equivalent to the displacement strain $\Delta\varepsilon_d(t_{j-1})$ that accumulated in the last time step.

If the direction of the incremental stain is not reverse but its magnitude does not exceed the magnitude of the underlying zone, the plastic zone continues to accumulate. And the equivalent plastic strain ε_p is the aggregate value of the displacement strain during these two time intervals. On the contrary, if the expanding plastic zone reaches the edge of the underlying plastic zone and the underlying zone is the outmost, the underlying zone is encroached by the expanding zone. In the other case, if the underlying zone is not the outmost, the growing zone edge will impinge on the previous zone that has the same sign. The two zones with the same sign will coalesce.

4.4.2 Definition of step length at bond foot interface

The length of the bonding interface is divided by several segments. The step lengths (d_i) are determined as an exponential series starting from the crack tip:

$$\ln(d_i) = \frac{i\cdot[\ln(d_{max})-\ln(d_{min})]}{N} \tag{4-13}$$

Where:

N is the number of steps

i is the step number

d_{min} is the minimum x-step length set to 0.02μm

d_{max} is the maximum x-step length and is expressed of maximum displacement strain caused by temperature and CTE mismatch, i.e. $d_{max} = \varepsilon_{max} \cdot \left(\delta_d\sqrt{LW}\right) = \Delta CTE \cdot \Delta T \cdot \left(\delta_d\sqrt{LW}\right)$. δ_d is a resolution factor.

The model step length along the initial bonding interface is then defined as:

$$x_i - x_{i-1} = d_{min} \cdot d_i \tag{4-14}$$

4.4.3 Determination of incremental crack length

According to the spatial plastic strain distribution, the damage value along the bonding interface decreases from the crack tip. It is assumed that crack generates at the position where the damage value is beyond 1 so the incremental crack length is determined by calculating the length over which D>1. At time step t_{j-1}, the damage value is calculated for each segment point x_i along the bonding interface. There are two adjacent points x_m and x_{m+1} which have the damage values of $D\ (x_m,\ t_{j-1})>1$ and D $(x_{m+1},\ t_{j-1})$ <1 respectively. Damage value $D=1$ must fall on a point within this interval. Therefore the fraction of the cell part that has the damage value bigger than one to the whole segment cell is calculated as follow:

$$fraction_{(D=1)} = \frac{1-D(x_m,t_{j-1})}{D(x_{m+1},t_{j-1})-D(x_m,t_{j-1})} \tag{4-15}$$

The position within the interval $[x_m,\ x_{m+1}]$ that corresponds to D=1can be determined, which is regarded as the incremental crack length.

$$\delta l_{j-1} = x_m + fraction \cdot (x_{m+1} - x_m) \tag{4-16}$$

The explanation of this procedure is shown in Figure 4.6.

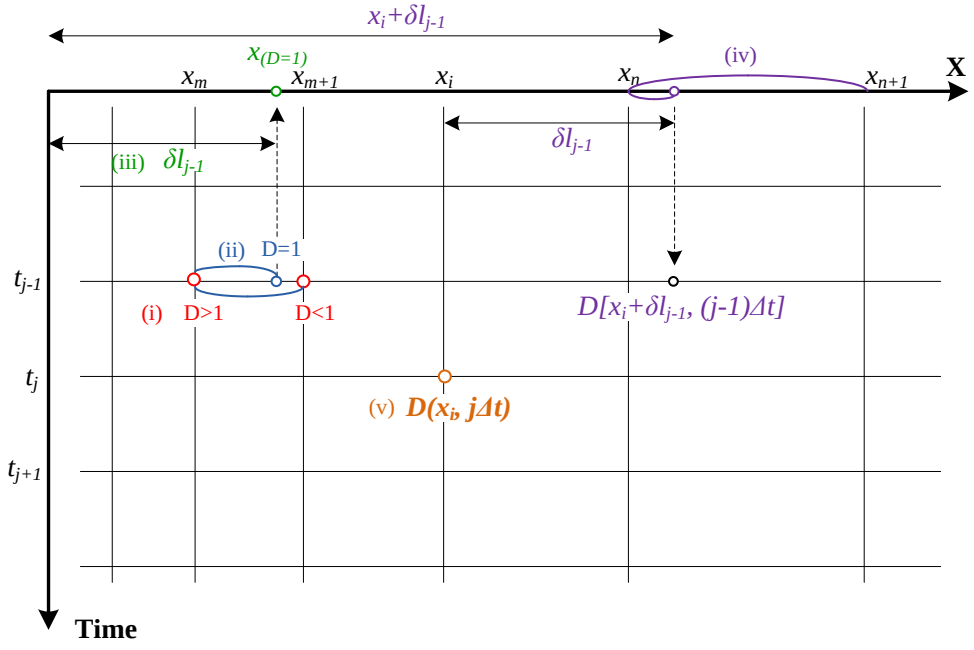

Figure 4.6: 2-D view of position-dependent damage model in x-t plane

4.4.4 Calculation of the damage value at bonding interface

To calculate the damage value for the cell index x_i at time t_j, it is necessary to know $D(x_i + \delta l_{j-1}, t_{j-1})$. The finite-difference discretization approximation is used here which is well known as one of the simplest numerical methods to solve differential equations [121]. The point $x_i + \delta l_{j-1}$ falls in an x-step interval $[x_n, x_{n+1}]$. The damage value $D(x_i + \delta l_{j-1}, t_{j-1})$ can be calculated by the same fractioning method:

$$D(x_i + \delta l_{j-1}, t_{j-1}) = D(x_n, t_{j-1}) + [D(x_{n+1}, t_{j-1}) - D(x_n, t_{j-1})] \cdot \frac{x_i + \Delta l_{j-1} - x_n}{x_{n+1} - x_n} \quad (4\text{-}17)$$

In summary, the determination of the damage value for position x_i and time t_j, i.e. $D(x_i, t_j)$ is implemented by five steps as follows:

(i) Find out the segment in which the two adjacent damage values are bigger than one and smaller than one respectively.

(ii) Calculate the fraction of the cell that has the damage value D >1 to the cell in this segment.

(iii) Using the calculated fraction determine the position in the x axis that corresponds to D=1 and thus obtain the value of incremental crack length δl_{j-1}.

(iv) Identify the position $x_i + \delta l_{j-1}$ and calculate $D[x_i + \delta l_{j-1}, t_{j-1}]$ via the same fractioning method.

(v) Calculate $D(x_i, t_j)$ by the equation (4-12).

Each implementation step is demonstrated in Figure 4.6 and the procedure order is marked in Roman numerals (i) ~ (v). The horizontal axis is the distance from the crack tip *x* and the vertical axis is time *t*.

4.4.5 Implementation in MATLAB

Implicit differentiation method is employed to implement the time stepping model, i.e. Equation (4-12)in MATLAB . Programs are attached in Appendix A. At each time step *t*, the value of interface damage is calculated for each step length along the bond foot. The materials for bond wire and semiconductor device are pure aluminium and silicon respectively. Wire diameter is 375μm and the length of the bond foot is 1000μm, which are the general dimension of an ultrasonically bonded wire foot. The bonding interface is exponentially divided into 35 segments from the bond foot origin (point O in Figure 4.2) and the mesh size for the first 25 segments is small enough (less than 100μm). Therefore in the simulation, the mesh point and step length remain the same with regard to the origin O as crack grows and the accuracy of the calculation

will not be significantly compromised. In the simulation cycling time of 3600 seconds is implemented as a general period for passive thermal cycling. Accordingly, time step is set to 18 seconds by which 200 sample points are achieved.

The temperature profile is defined by temperature extremes, cycling time and dwell time. Model parameters have been adjusted to demonstrate greater accumulation of damage at low temperatures and annealing at high temperatures. Initial parameters used in the damage model are tabulated in categories (Table 4.1).

Table 4.1 Initial parameters for the position-dependent damage model

Temperature profile:		
Amplitude	T_{max}	125°C
	T_{min}	-55°C
Cycling time		3600 second
Dwell time		0
Material and physical constants:		
Wire diameter	W	375 μm
Length of bond foot	L	1000 μm
CTE	α_{Al}	23 μm/m/°C
	α_{Si}	2.6 μm/m/°C
Gas constant	R	8.31447
Model Coefficients and Exponents:		
Damage constant	G_0	10
Work hardening coefficient	α_H,	0.5
Work hardening exponent	β_H,	20
Equilibrium temperature	T_{eq}	90°C
Temperature hardening exponent	β_T	3
Annealing coefficient	k_2'	6×10^7
Activation energy	Q	84000 J/mol

In [15], a damage-based prediction methodology was proposed to predict degradation rate of the bond shear force by introducing a variable to account for damage removal during exposure to elevated temperatures. The wear-out rates predicted by the approximations of the anneal fraction show good agreement with experimental data with the annealing coefficient $k_2^{'} = 6 \times 10^7$and activation energy Q = 84000 J/mol. The value of Q is similar to the activation of energy for boundary diffusion in aluminium [112, 113]. This annealing coefficient is applied here as an initial value and thereafter, in the implementation of the new time-domain model, the value of Q is taken as 84000 J/mol.

It is well known that engineering materials creep starts to be noticeable at homologous temperatures equal to or greater than 0.3. Homologous temperature is defined as the ratio of the absolute temperature to its absolute melting temperature in Kelvin. Here the equilibrium temperature is selected as 90°C which is a homologous temperature of 0.4 for pure aluminium so the thermally activated processes become significant from this point.

Work hardening exponent measures the ability of a metal to harden and usually lies between 0 and 1. For most f.c.c metals (e.g. pure aluminium) the value is approximately 0.5 [106, 107], where f.c.c. represents face-centred cubic crystal structure. Therefore, in the implementation of the new time-domain model, the value of work hardening exponent β_H is taken as 0.5.

Figure 4.7 shows the output from the model for a thermal cycle defined in Table 4.1. The interface damage is expressed in a 3-D mesh surface as a function of both time and position. It can be seen that for a certain time step, i.e. in the Damage-Distance plane, the damage mainly aggregates within a damage zone around crack tip. It has the maximum value at crack tip and decreases along the bonding interface. In the Damage-Time plane, the value of damage fluctuates up and down in the response of the heating and cooling regimes within a cycle indicating the damage accumulation and annihilation as the result of temperature swings.

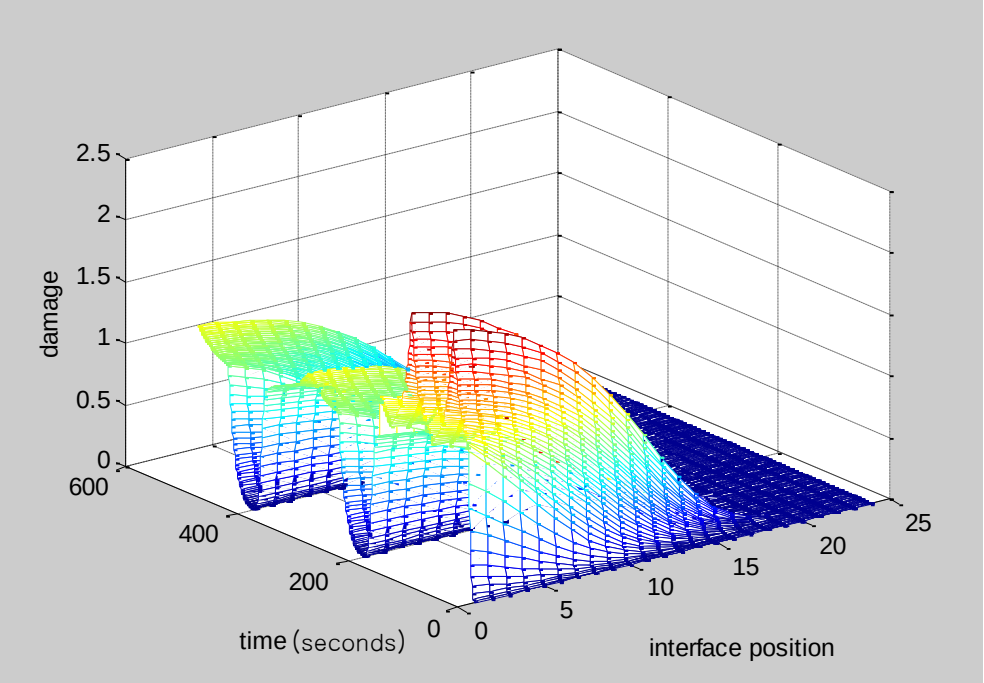

Figure 4.7: 3-D view of interface damage as a function of time and position

4.5 IMPLEMENTATION OF TOTAL INTERFACE DAMAGE MODEL

4.5.1 Based on the position-dependent model

The above position-dependent model estimates interface damage values as a function of time and position. Based on this model, the total interface damage at time instant t_j, can be obtained by summing the multiplication of the damage value for each x-step and the corresponding step size at this time instant.

$$D_T(t_j) = \sum D(x_i, t_j) \cdot x_i \tag{4-18}$$

Figure 4.8 shows development of total damage and crack propagation as a function of time (green lines). Blue line is the temperature profile. It can be seen that the model is able to demonstrate both the build-up of the damage during the low temperature regime and damage removal processes during the

high temperature phase of the cycle. Meanwhile the crack grows as time increases despite that the length is not in proportion to the actual size at this stage.

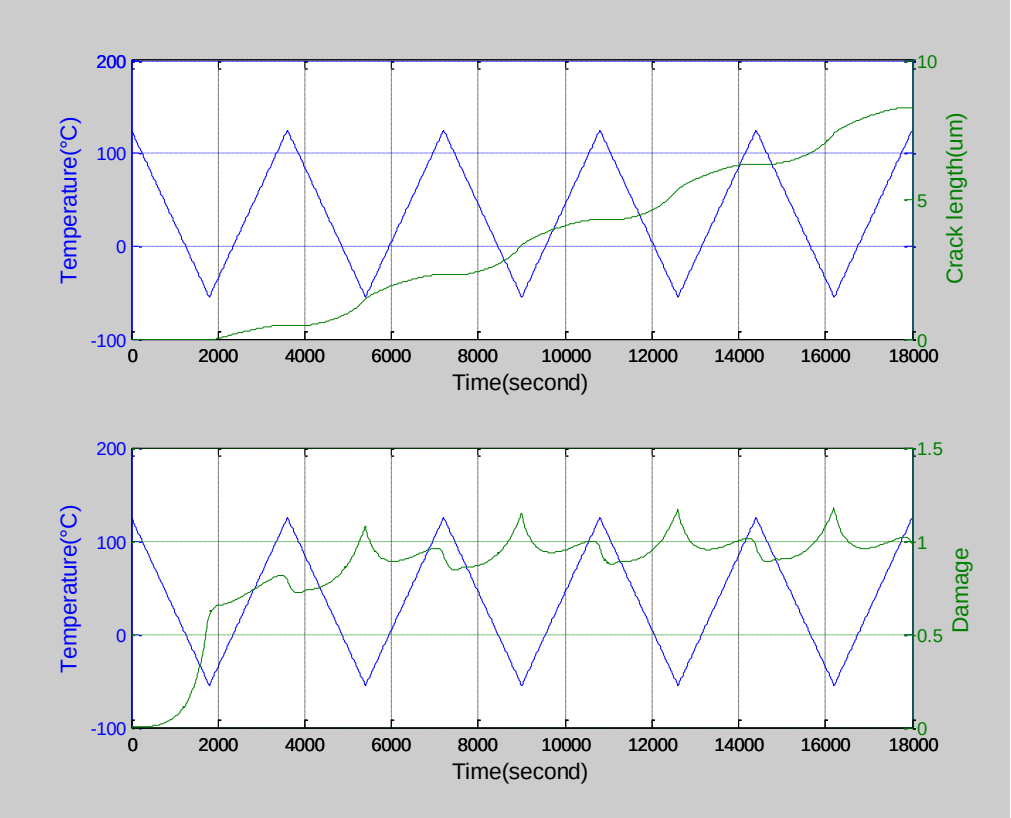

Figure 4.8: Evolution of total interface damage and crack growth as a function of time

The above approximations are based on the position-dependent damage model. The simulation has been burdened with the calculation of the damage value for each *x* step. It is a paradox that the accuracy of the approximation depends on the number of *x* step. Using more steps produces a closer approximation but will dramatically increase the amount of the calculation.

4.5.2 Based on integral of the functions

In this section, efforts are made to develop a total damage model via implicit differentiation with some assumptions.

At any time instant, the damage at any point along the interface is expressed as *D (y, t)*. Therefore the total interface damage with respect to this time instant can be found by integrating *D (y, t)* within the interval [*l*, *L*] that defines the distance from the crack tip along the bonding interface. This has been expressed by Equation (4-2) in the previous section, i.e.:

$$D_T(t) = \int_{y=l}^{y=L} D(y,t)dy \tag{4-2}$$

The time derivative of the total damage is given by Leibniz's rule:

$$\frac{dD_T}{dt} = \int_{y=l}^{y=L} \frac{\partial D}{\partial t} dy - D(l)\frac{dl}{dt} \tag{4-19}$$

The first term on the right hand side corresponds to the integral of the differential Equation (4-6), i.e.:

$$\begin{aligned}\int_{y=l}^{L} \frac{\partial D(y,t)}{\partial t} dy &= \int_{y=l}^{L} \left[f_\varepsilon(\varepsilon) f_T(T) f_D(D) \frac{dT}{dt} - \alpha_D(D)\alpha_T(T) \right] dy \\ &= \int_{y=l}^{L} \left\{ g\big(y-l,\varepsilon_p\big) f(T)[1+h(D)] \frac{|d\varepsilon_d|}{dt} - \alpha(T)D \right\} dy\end{aligned} \tag{4-20}$$

Hence Equation (4-19) can be reinterpreted as:

$$\frac{dD_T}{dt} = \int_{y=l}^{L} \left\{ g\big(y-l,\varepsilon_p\big) f(T)[1+h(D)] \frac{|d\varepsilon_d|}{dt} - \alpha(T)D \right\} dy - D(l)\frac{dl}{dt} \tag{4-21}$$

Although *f(T)* and *α(T)* are the functions of temperature alone and can be taken outside of the integral, integration of the product of functions *g* and *h* functions is difficult to solve. Therefore assumptions need to be made to obtain an equivalent form that has the same functional behaviour without significant loss of accuracy.

Apart from $g(y-l,\varepsilon_p)$ that is a function of distance and describes the damage distribution along the bonding interface, other functions are all damage-related terms. Therefore integrated form of the distribution function is used to account for the damage integration along the interface and those damage-related functions are simply taken outside of the integral representing the damage accrued in the last time step.

Therefore Equation (4-21) can be written as:

$$\frac{dD_T}{dt} == F(T)[1+H(D_T)]\frac{|d\varepsilon_d|}{dt}\int_{y=l}^{L}\left[g(y-l,\varepsilon_p)\right]dy - A(T)D_T - D(l)\frac{dl}{dt} \tag{4-22}$$

In order to solve the equation, firstly it is necessary to find out the solution for the integral of the damage distribution function. The boundaries of the integral interval, i.e. the size of the intensive damage zone needs to be decided.

From Figure 4.9 it can be seen that damage mainly aggregates within a damage zone around crack tip. In the materials under stresses, two distinct zones usually form in vicinity of a crack tip. One is the plastic zone where intensive deformation occurs. The outer surrounding zone is the damage zone where the degree of deformation is lower. The deformation outside these two zones is negligible [48]. So only the damage within the damage zone is taken into account for solving the integral of $g(y-l,\varepsilon_p)$ function. If r_d represents the size of the total damage zone, it can be reinterpreted as:

$$\int_{y=l}^{L}[g(y-l,\varepsilon_p)]dy = G_0\sqrt{LW}|\varepsilon_p| \times \left[1 - exp\left(-\frac{r_d}{\sqrt{LW}|\varepsilon_p|}\right)\right] \quad (4\text{-}23)$$

Here one time of $\sqrt{LW}|\varepsilon_p|$ is regarded as the size of the plastic zone and four times of $\sqrt{LW}|\varepsilon_p|$ as the size of total damage zone. Figure 4.8 illustrates the assumption on the damage size for the integral of damage distribution function.

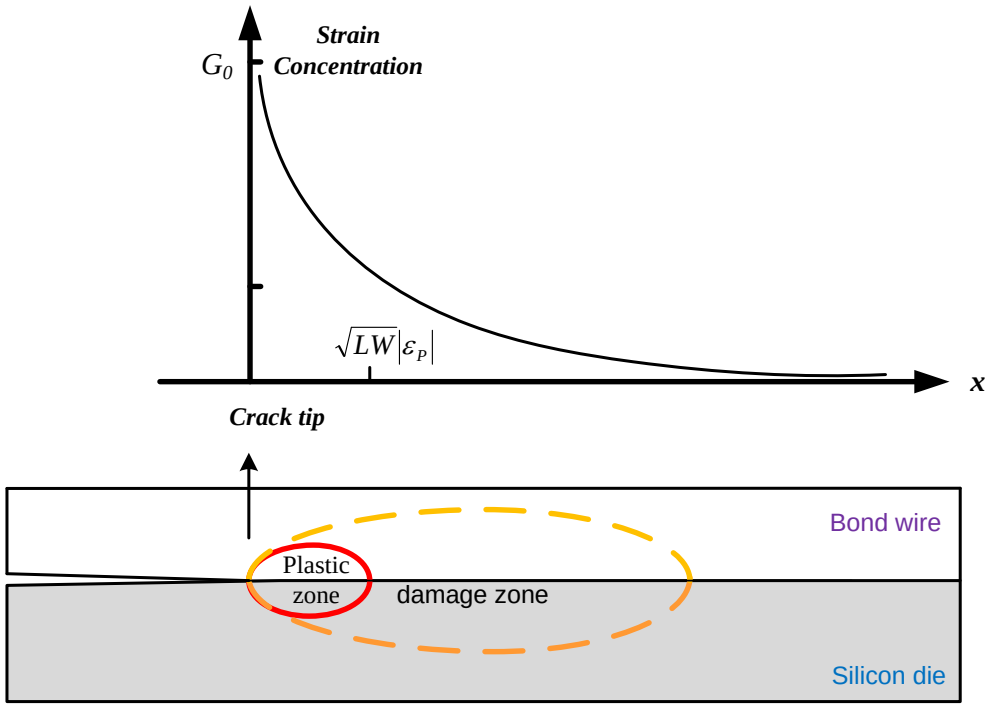

Figure 4.9: Assumption on the size of the damage zone

Secondly, the final term $D(l)\frac{dl}{dt}$ in Equation (4-22) poses a problem and must be reinterpreted in terms of total damage.

Crack growth rate can be described as a function of the amount of total damage and the rate of change of the damage. The incremental crack length is

approximated by a simple linear relation for the total damage and the change rate when it is above a threshold level and zero below that threshold level:

$$\delta l = 0, \qquad D_T < D_{th} \tag{4-24}$$

$$\delta l(t_i) = \alpha_L D_T(t_{i-1})\delta t + \beta_L[D_T(t_i) - D_T(t_{i-1})], \quad D_T \geq D_{th} \tag{4-25}$$

β_L is set to a much smaller value than α_L as the incremental crack length is mainly determined by the total damage in comparison with the changing rate.

4.5.3 Simulation of total interface damage

With the above limitations and assumptions, a time stepping model is implemented in MATLAB by Equation (4-26). The total interface damage at any time step is associated with the damage value at last time instant.

$$\begin{aligned} D(t_i) = D(t_{i-1}) &+ G_0\sqrt{LW}\left|\varepsilon_p(t_i)\right| \times \left[1 - exp\left(-\frac{\mathrm{r_d}}{\sqrt{LW}\left|\varepsilon_p(t_i)\right|}\right)\right] \\ &\times \left(1 + \alpha_H D(t_{i-1})^{\beta_H}\right) \times \left(\frac{T_{eq}}{T(t_i)}\right)^{\beta_T} \times \left|\varepsilon_d(t_i) - \varepsilon_d(t_{i-1})\right| \\ &- D(t_{i-1})k' exp\left(-\frac{Q}{RT(t_i)}\right)(t_i - t_{i-1}) - D(t_{i-1})\delta l(t_{i-1}) \end{aligned} \tag{4-26}$$

Figure 4.10 shows the simulation results of the integrated total interface damage as a function of time under -55°C ~ 125°C temperature range. It can be seen that the overall trend starts from an increase at the beginning of the temperature loading and then reaches a saturation value (Figure 4.10 a). It agrees with the expectation from the model that the damage grows around the crack tip until it reaches certain level and moves along the bonding interface as the crack propagates keeping the amount of damage. From the detail view of the damage evolution within one cycle (Figure 4.10 b), it can be seen that the

model is able to demonstrate both the build-up of the damage during the low temperature regime and damage removal processes during the high temperature phase of the cycle.

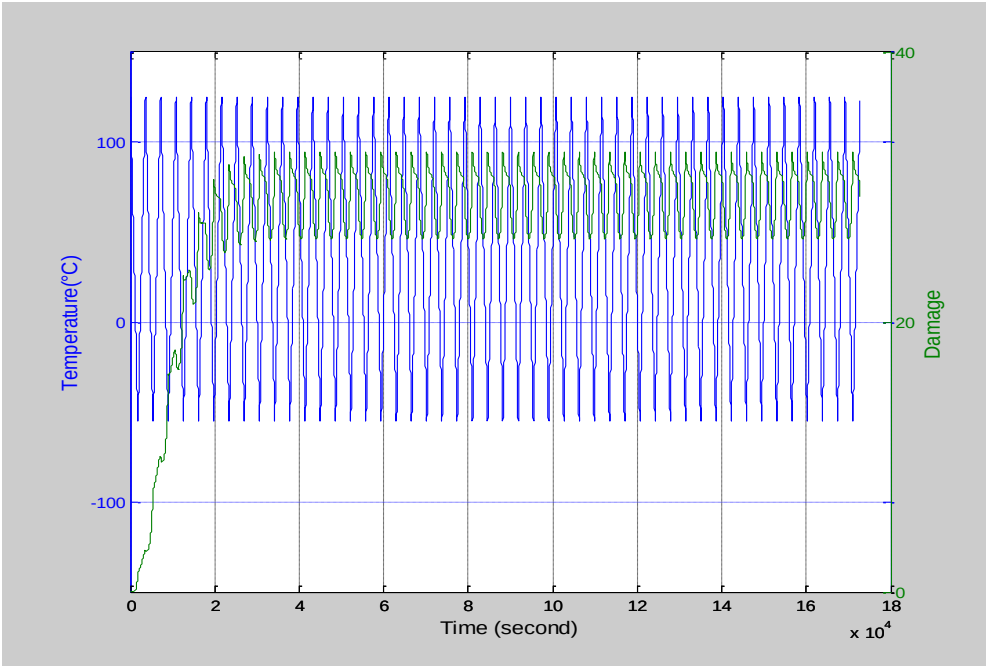

(a)

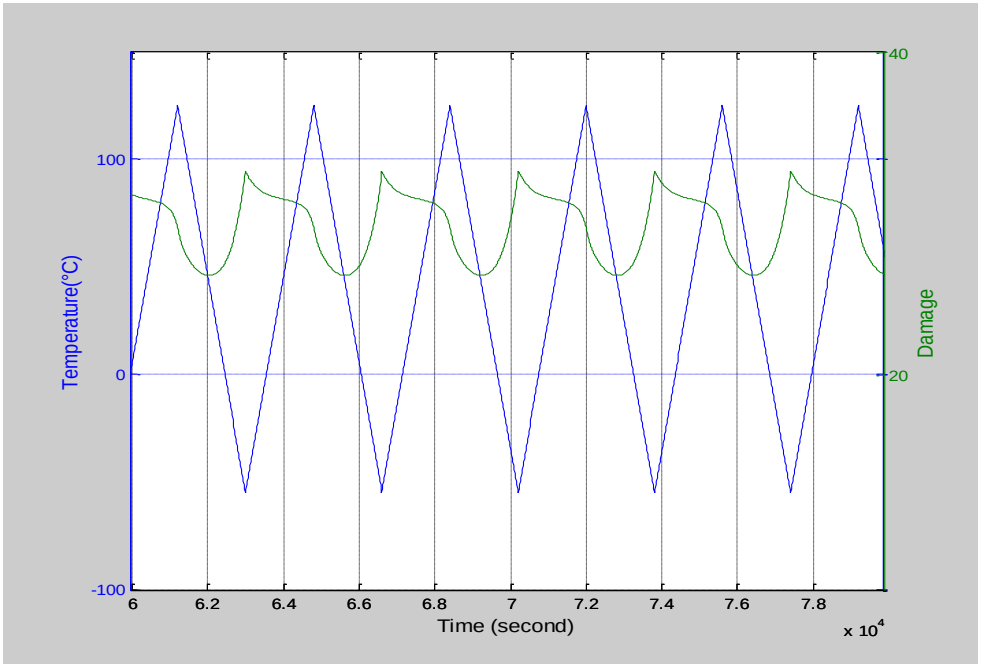

(b)

Figure 4.10: Total interface damage as a function of time

4.6 SIMULATION OF CRACK GROWTH AND DEVELOPMENT OF BOND SHEAR FORCE

Crack growth is the result of the damage accumulation in the bond wire material during temperature exposure, and the degradation in shear force can be attributed to a reduction in the bonded area as a crack grows. Therefore shear force, a much more easily measured parameter, is employed to provide a quantitative indication of the parameter damage. The simulation result of shear force and crack length is shown in Figure 4.11. It can be seen that crack grows and shear force reduces as time increases which indicates that initially the model is able to predict these experimental phenomena although they are not quantified at this stage.

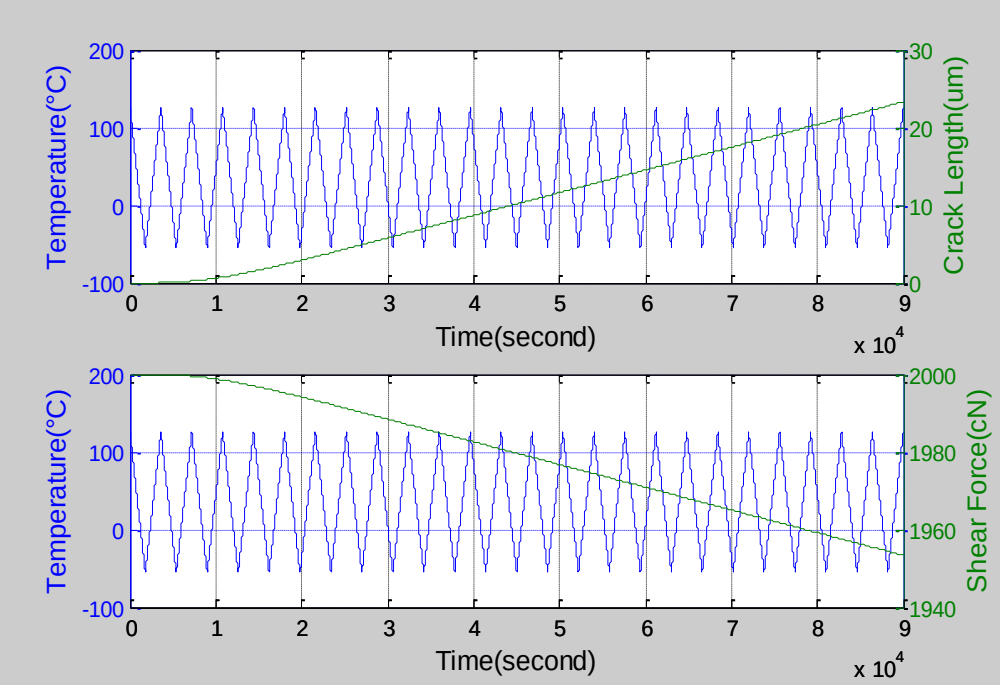

Figure 4.11: Development of crack length and shear force as a function of time

4.7 SUMMARY

In this chapter, the damage based crack propagation model is presented and the implementation procedures are described in full details. The damage model is then related to bond shear force which is an accessible physical parameter so that experimental validation can be accomplished more easily. Initial simulation results of the evolution of total interface damage, crack growth and shear force degradation from this new time-domain approach show the expected outcomes. The position-dependent damage model has the desired result on expressing interface damage as a function of time and position. And the total interface damage model can demonstrate both the damage accumulation and removal processes during fluctuating temperature loads. Finally the simulation result for shear force has shown wire bond degradation under repeated temperature cycling.

In the next chapter the proposed new model and all the parameters are justified and calibrated by the existing experimental bond shear force data during passive thermal cycling and bond wire material characterization from the fundamental isothermal tensile tests under various conditions.

CHAPTER 5

MODEL VERIFICATION AND CALIBRATION

5.1 INTRODUCTION

In Chapter 4, the development and implementation of the damage based crack propagation model has been presented in detail. Simulation results of the damage evolution and shear force degradation have shown that the model works as intended. It demonstrates both damage accumulation and damage removal processes under fluctuating temperature loads. Also the model can operate as a function of time.

Once the constitution of the model is determined, it is necessary to conceptually verify the numerical implementation of the proposed model against physically quantifiable properties and justify model parameters by reference to experimental data. In this chapter, model verification is performed by relating the damage parameter to the plastic strain energy dissipated during plastic deformation in the bonding wire material. Isothermal uniaxial tensile tests have been carried out for pure aluminium bond wires to derive the values of strain energy under different loads as well as to obtain fundamental information about mechanical properties of the wire material.

The crack propagation model is then operated to predict the bond degradation rate under passive thermal cycling conditions via estimation of the damage in the wire material so that the model parameters can be calibrated by optimum matches between model predictions and experimentally obtained data.

5.2 VERIFICATION OF THE DAMAGE MODEL

5.2.1 Model verification conception

In the proposed damage based crack propagation model, ‘damage’ is the core parameter. It is preferable to link it to a physically quantifiable property of the material which can be extracted from experimental data.

Upon heating and cooling, bonding materials expand or shrink at a certain rate. The mismatch in thermal expansion coefficient between the wire material and semiconductor device causes shear stresses at the bond interface. The plastic strain induced by expansion and shrinkage is cumulative which builds up damage in wire material.

Repeated plastic strain is the predominant cause of energy dissipation in metals as the result of deformation under load [114]. Plastic strain energy contributes to the damage of the material and can be related to fatigue crack initiation life. When the total amount of the accumulated damage energy exceeds the crack initiation energy of the material, the growth of the cracks becomes inevitable [115].

This theory is consistent with the concept of the parameter ‘damage’ in the proposed crack propagation model. Therefore the damage in the wire material can be evaluated by estimating the strain energy dissipated in the bond wire during thermal cycling and this can thus be related to the damage parameter (D) in the damage-based model.

The values of cumulated damage under certain constant temperatures can be calculated by the damage model. Meanwhile plastic strain energy can be extracted from monotonic stress-strain curves obtained by means of tension test.

In the next sub-sections, isothermal uniaxial tensile tests are introduced and relevant material properties are illuminated by experimentally obtained stress-strain curves for each loading condition which enables evaluation of strain

energy density for the tested wires. These experimental results are then compared with the damage values estimated by the damage simulation model. The comparison results are discussed accordingly.

5.2.2 Isothermal uniaxial tensile testing

Tensile testing is the most fundamental material test to determine the deformation and fracture characteristics of the material. It is accomplished by gripping opposite ends of the specimen within the load frame of the test machine. A uniaxial tension load is applied at a specific extension rate resulting in the gradual elongation and eventual fracture of the specimen. During the process, the elongation of the specimen is measured and a transducer connected with the specimen provides an electric reading of the applied load corresponding to the displacement. These load-extension data, a quantitative measure of how the wire deforms under the applied tensile force (P) can determine the engineering stress and strain values using the original wire specimen cross-sectional area (A_0) and length (l_0). The engineering stress (σ_e) is the average longitudinal stress in the specimen and engineering strain (ε_e) is the length increment (Δl) against the original unstrained length.

$$\sigma_e = \frac{P}{A_0} \tag{5-1}$$

$$\varepsilon_e = \frac{\Delta l}{l_0} \tag{5-2}$$

In practice, true stress/strain is used rather than engineering stress/strain. As the specimen dimensions experience substantial change from the original values when beyond the elastic limit, true values can give more direct measure of the material response in the plastic flow range. The relationships between true values and engineering values are:

$$\sigma_t = \sigma_e(1 + \varepsilon_e) \tag{5-3}$$

$$\varepsilon_t = \ln(1 + \varepsilon_e) \tag{5-4}$$

A tensile profile can quantify several important mechanical properties which include elastic and plastic deformation properties, such as the modulus of elasticity (Young's modulus); yield strength and ultimate tensile strength; ductility properties which can be represented as % elongation or % reduction in area; strain-hardening characteristics.

A typical stress-strain curve for a ductile material shows strains from zero up to specimen fracture including the region of elastic deformation, plastic deformation and necking (Figure 5.1). A material exhibits linear-elastic behavior till its proportional limit in which deformation is completely recoverable when unloaded is exceeded. Beyond this linear region, deformation is plastic. After the yield point, ductile materials undergo strain hardening that continues till it reaches ultimate stress. At fracture point, the material loses strength.

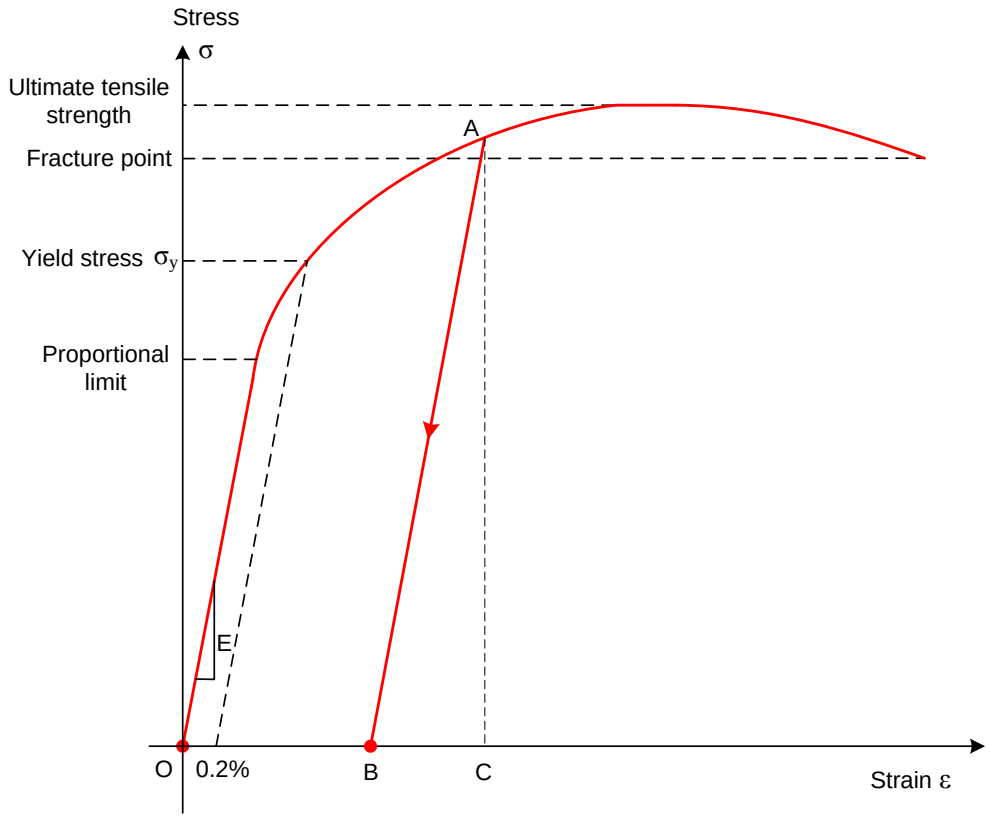

Figure 5.1: A stress-strain curve showing typical yield behaviour

If the specimen is unloaded after yielding, the material will experience a permanent residual strain that is not lost on unloading. The stress-strain relationship will follow a line with a slope equivalent to the elastic modulus E back to the strain axis because the material unloads elastically, as illustrated by segment A-B in Figure 5.1. The recovered strain is the elastic strain and the remaining part is the residual plastic strain. Thus, the elastic strain energy recovered during unloading is represented by the area of triangle ABC. The area within O-A-B-O represents energy that is lost in the process of permanently deforming the tested material. This energy is known as the plastic strain energy which contributes to the extent of plastic deformation or damage in loaded materials.

5.2.3 Experiment setup

In this project, isothermal uniaxial tensile testing was carried out to evaluate the dynamic stress-strain response of as-draw pure aluminium wire used for power module interconnects at temperatures ranging from -55°C to 190°C, with the view to elucidating the effect of temperature and strain rate on its work hardening characteristics.

During the tests, 99.999% (5N) pure aluminium wire, 375μm in diameter and wound onto an 8”dia spool supplied by SiTEST Ltd. was cut into approximately 25 mm lengths. These were mounted onto paper tabs to minimise their handling while being clamped into position. The paper tabs provided tabs which could be more easily manipulated. Each wire was clamped into place with a fixed value of torque. Testing was performed on a Dynamic Mechanical Analyzer (DMA-Q800, TA Instruments) with a maximum load capacity of 18N, and displacement and force resolutions of 1 nm and 0.00001N respectively. Isothermal uniaxial tensile tests were then performed at constant strain rate values ranging from 0.00001/s, to 0.01/s, and at temperatures ranging from -55°C to 190°C. Tests were terminated at between 8% and 10% strain.

5.2.4 Experimental results and discussions

5.2.4.1 Dynamic stress-strain characteristics

Figure 5.2 shows flow curves of tested aluminium wires at different temperatures and strain rates. A pre-load force of 0.07N was applied prior to deformation; however, this was not sufficient to straighten the wires which were slightly curved as a result of having been wound onto a spool. Evidently, straightening of the wires was still required at the start of testing; resulting in relatively large amounts of strain during the initial stage of each test and producing an s-shaped engineering stress-strain curve.

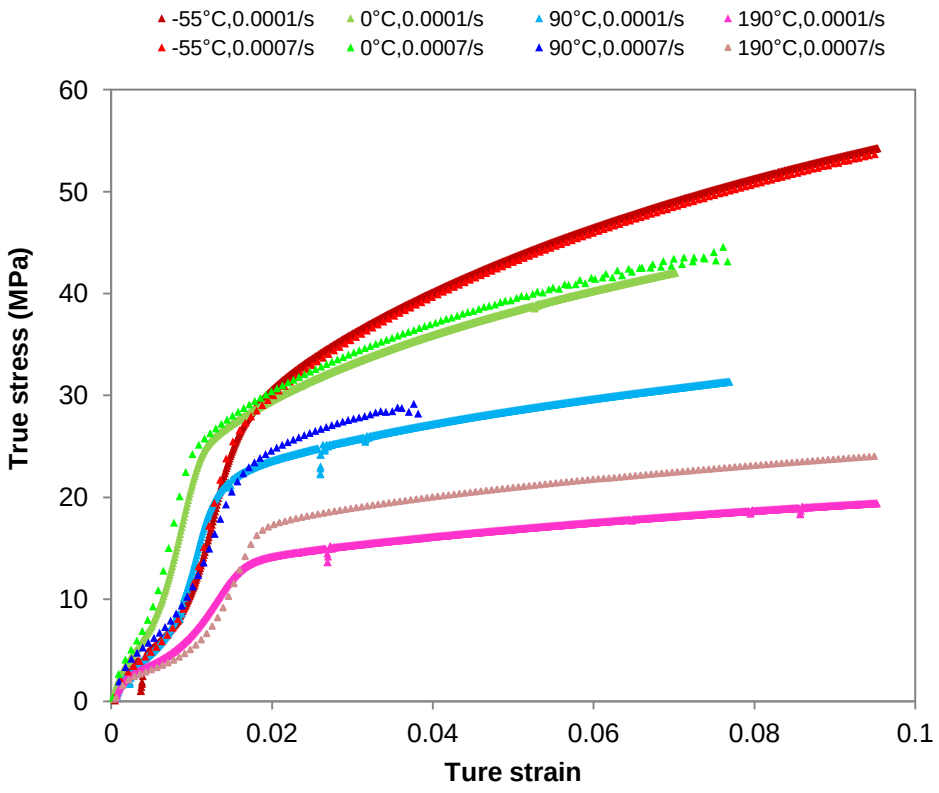

Figure 5.2: Flow curves at different deformation conditions for 5N 375µm Al wire

A decrease in yield stress and lower characteristic strain with increase in temperature is evident from the flow curves in Figure 5.2. Also evident from the figure is the effect of strain rate. At high strain rate, concurrent recovery decelerates the rate of work hardening. Consequently, flow stress tends to increase when strain rate is increased, although this effect is more pronounced at the higher end of the temperature spectrum. This is illustrated more clearly in Figure 5.3 in which the plot of flow stress versus strain rate for the six constant temperatures is shown in the log scale. It can be seen that the change of flow stress to strain rate is more sensitive at higher temperatures.

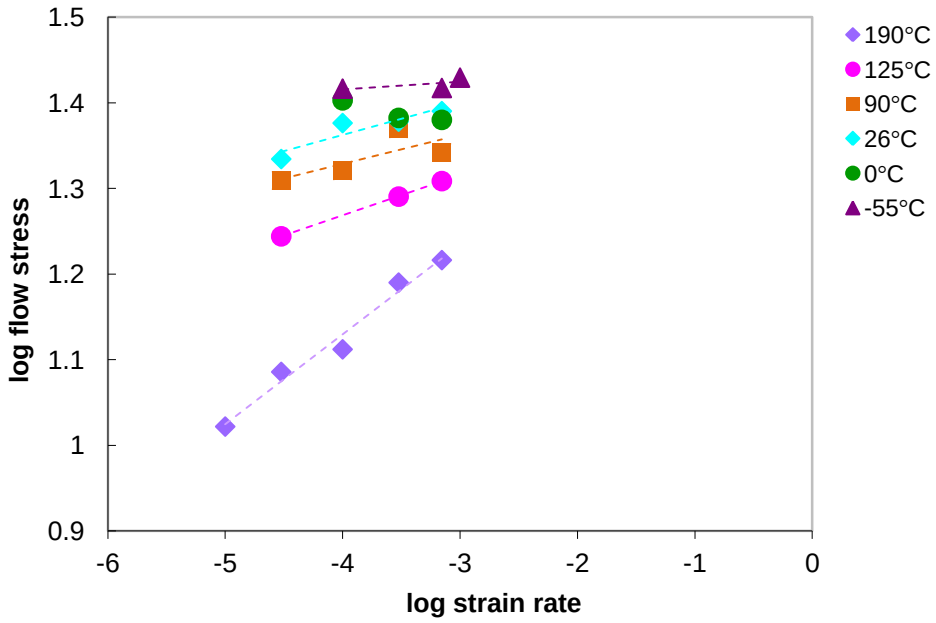

Figure 5.3: Sensitivity of flow stress to strain rate at constant temperature

5.2.4.2 Estimation of plastic strain energy density

The energy stored in a body due to deformation is the strain energy and the strain energy per unit volume is the strain energy density. Geometrically, strain energy density is the area underneath the stress-strain curve up to the point of deformation.

$$W = \int_0^{\varepsilon} \sigma d\varepsilon \tag{5-6}$$

For ductile metals (e.g. pure aluminium) the area under the flow curve can be approximated as a trapezoid shape as illustrated in Figure 5.5, where the blue broken line represents the stress-strain curve and the by the trapezoid is shaded and bounded by red lines.

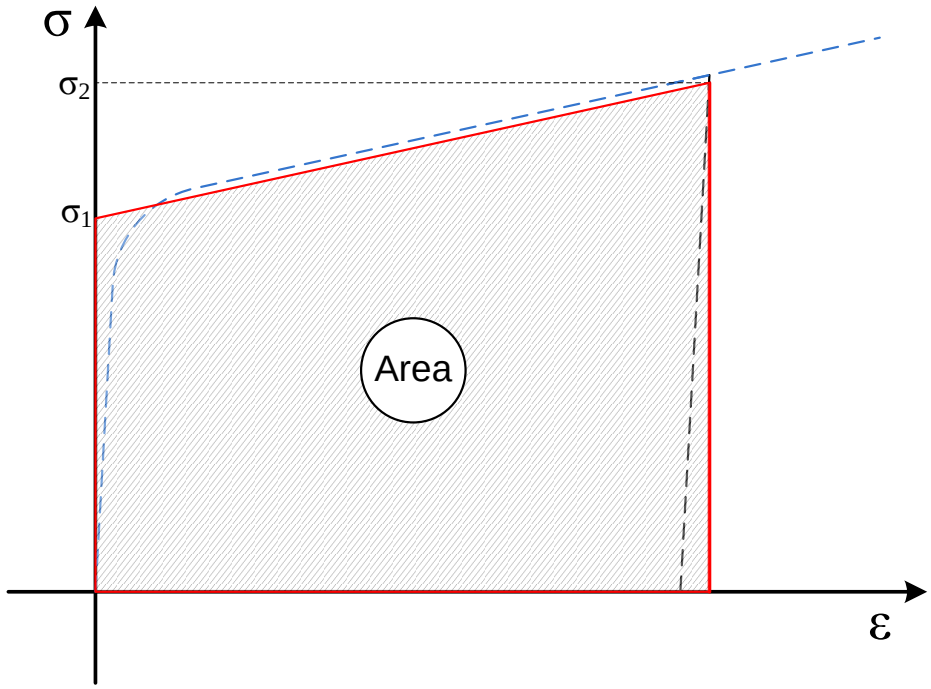

Figure 5.5: Strain energy computation based on trapezoid approximation of the area

Therefore the strain energy corresponding to a certain strain value can be calculated based on trapezoid approximation of the area:

$$W \approx \frac{1}{2} \cdot (\sigma_1 + \sigma_2) \cdot \varepsilon \tag{5-7}$$

For the purpose of estimating the strain energy at each constant temperature loading based on this approximation of the area, the stress-strain curves under

six constant loading temperatures with a selected strain rate of 0.0001/s have been corrected. The S-shape before the yield point of each original curve is corrected by a straight line extending the linear part of the beginning of the curve. Then the original curve after the yield point is shifted to the left until it overlaps with the linear part.

Figure 5.6 shows the original true stress-strain curve for a room temperature (25°C) test at a strain rate of 0.0001/s (in green), and its corresponding corrected curve (red dashed line).

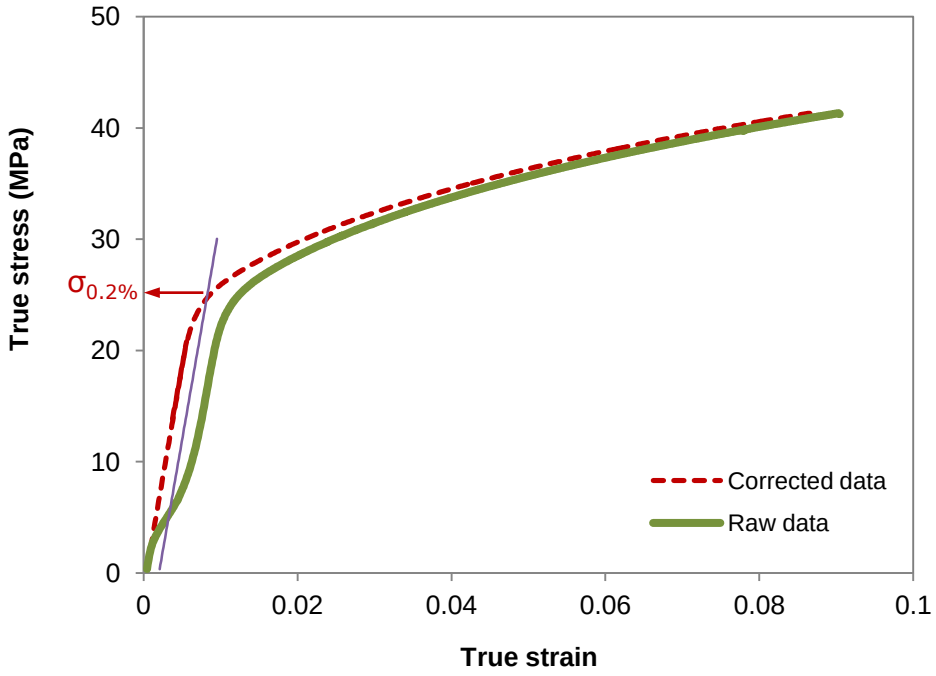

Figure 5.6: Original and corrected flow curves under room temperature

The plastic strain energy absorbed to reach the strain of 6% is estimated for the six constant loading temperatures under the same strain rate of 0.0001/s using Equation (5-10). For the temperature of 125°C, the strain rate of 0.0003/s is selected due to the availability of the experimental data.

$$W \approx \frac{1}{2} \cdot (\sigma_{0.2\%} + \sigma_{6\%}) \cdot \varepsilon_{=0.06} \tag{5-8}$$

The results are listed in Table 5.1.

Table 5.1: Strain energy density for 5N aluminium wire under different temperatures

Temperature (°C)	$\sigma_{0.2\%}$ (MPa)	$\sigma_{6\%}$ (MPa)	Strain energy density ($\times 10^5$ J/m^3)
-55	27.14	48.42	22.67
0	25.04	41.18	19.87
25	24.72	37.91	18.79
90	21.45	30.13	15.47
125	19.73	28.04	14.33
190	12.57	18.12	9.21

5.2.5 Simulation of damage under isothermal tension loading conditions

5.2.5.1 Extraction of constitutive model

In the damage model discussed in Chapter 4, the estimation of incremental damage in the wire material is based on crack propagation along the bonding interface corresponding to cyclic temperature loading conditions.

Damage accumulation term — Damage removal term

$$\delta D(y,\Delta t) = G_0 \exp\left(-\frac{y-l}{\sqrt{LW}\left|\varepsilon_p\right|}\right)\cdot\left(1+\alpha_H D^{\beta_H}\right)\cdot\left(\frac{T_{eq}}{T}\right)^{\beta_T}\cdot\left|\delta\varepsilon_d\right| - D\cdot k_2^{'}\exp\left(-\frac{Q}{RT}\right)\delta t$$

Strain distribution function — Constitutive functions

In this section, the damage parameter is to be compared to strain energy which is a material property characterized under mechanical loading. The damage

model is based on crack propagation and cannot be employed straightaway to derive the damage values. Alternatively, the embedded constitutive relation is extracted from the fracture mechanics-based damage model. This is explained in the following paragraphs.

In the proposed damage model, the damage accumulation term consists of a strain distribution function and strain-driven constitutive functions. The strain distribution function represents bond geometry and the strain-driven constitutive functions include a work hardening term and a temperature hardening term with a strain expression that describes how materials respond to various loadings.

A constitutive model (Equation 5-9) is extracted to represent the cumulative damage under mechanical loading conditions so that the corresponding damage values can be compared to strain energy that is experimentally derived from mechanical tests.

$$\delta D(t) = \left[1 + \alpha_H D^{\beta_H}\right] \cdot \left(\frac{T_{eq}}{T}\right)^{\beta_T} \cdot |\delta\varepsilon_d| - D \cdot k_2' exp\left(-\frac{Q}{RT}\right)\delta t \tag{5-9}$$

5.2.5.2 Displacement strain

In the crack propagation model, damage is driven by displacement strain ε_d which is induced due to mismatched CTE between the bond wire material and semiconductor device (equation 4-9). In the process of tensile tests, the wire samples are strained under mechanical stress and the strain is cumulative at a constant strain rate. In the last section, the plastic strain energy was estimated for the strain of 6% under the same strain rate of 0.0001/s. Correspondingly the displacement strain term ε_d is replaced by a linear function of time with the constant rate of 0.0001/s to simulate the cumulative strain and damage is estimated at each time step until the strain accumulates to the final value of 6%.

5.2.5.3 Discussion

The values of strain energy density absorbed to reach the strain of 6% for the different temperatures (Table 5.1) are demonstrated in Figure 5.7 marked with blue solid diamond shape which has shown a linear distribution (blue broken trend line).

The constitutive model (Equation 5-9) was operated for a wide range of constant temperatures ranging from -55°C to 190°C. A series of damage values corresponding to 6% strain are calculated and shown in Figure 5.7 by dotted lines. The red and green dotted lines correspond to two different values of temperature hardening exponent β_T=0.6 and β_T=1 respectively. They both show a power law distribution which is determined by the power relation between damage and temperature, i.e. temperature hardening function $f(T) = \left(\frac{T_{eq}}{T}\right)^{\beta_T}$. Although changing the scaling of exponent β_T varies the power of the temperature effect, a linear fit (with the experimental data) is still impossible with this temperature hardening function in its current form.

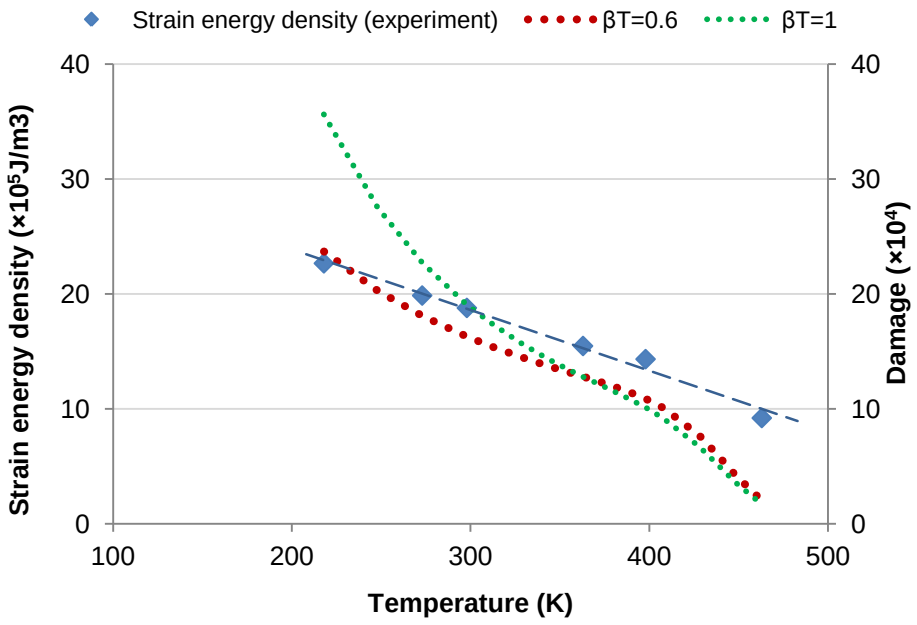

Figure 5.7: Comparison between the experimentally derived strain energy density and modelled damage for 5N aluminium bond wires

5.2.6 Modification to the temperature hardening function

The temperature hardening term in the damage model is to describe the dependency of damage accumulation in the wire material on the loading temperature. The expression was created to show that temperatures lower than the equilibrium temperature have a cumulative effect on damage and those higher than the equilibrium temperature have a damage annihilating effect. Therefore, the form of this term is modified to a linear relation, in keeping with the experimentally obtained results, whilst keeping the original principle.

$$f(T) = \alpha_T\left[1 - \beta_T\left(T - T_{eq}\right)\right] \tag{5-10}$$

Thus replacing Equation (5-9) with Equation (5-10), we now have:

$$\delta D(t) = \left[1 + \alpha_H D^{\beta_H}\right] \cdot \alpha_T\left[1 - \beta_T\left(T - T_{eq}\right)\right] \cdot |\delta\varepsilon_d| - D \cdot k_2' exp\left(-\frac{Q}{RT}\right)\delta t \tag{5-11}$$

Simulation of this new form of the model was performed in MATLAB for temperatures ranging from -55°C to 190°C. Model parameters including work hardening coefficient (α_H), work hardening exponent (β_H), temperature hardening exponent (β_T) and the new included temperature hardening coefficient (α_T), were tuned to fit the experimentally derived strain energy density values. The values of these model parameters applied in the simulation are listed in Table 5.2.

Table 5.2: The values of the model parameters employed in the simulation under isothermal tensile test conditions

Variables		Constants	
α_H	40	T_{eq}	90 °C
β_H	0.5	R	8.31447
α_T	3.5	Q	84000J/mol
β_T	1.8×10^{-3}		
k_2'	3×10^{3}		

The constitutive modelling program to calculate the damage value is shown below in Figure 5.8.

```
Teq=90+273;

Q=84000;R=8.31447;
alphaH=40; betaH=0.5 ;alphaT=3.5; betaT=1.8e-3;k2=3e3;


T=25;                              % (temperature)
TK=T+273;

strain_rate=0.0001;                % (strain rate)

t=0:1:600;                         % (time)
strain_disp=strain_rate*t;         % (displacement strain)


delta_t=1; ;                        % (time step)
damage(1)=0;

for i=2:600

 damage(i)=damage(i-1)*(1-k2*exp(-
Q/R/TK)*delta_t)+(alphaH*damage(i-1)^betaH+1)*(alphaT*(1-
betaT*(TK-Teq)))*strain_disp(i);

end

damage(600)
```

Figure 5.8: Constitutive modelling algorithm

A series of damage values corresponding to 6% strain for the temperatures are calculated and shown in Figure 5.9 by a red dotted line. The comparison between these two parameters shows a good agreement which confirms that (i) it is appropriate to replace the power relation between damage and temperature by the linear relation (ii) the 'damage' parameter can be quantitatively linked to strain energy density.

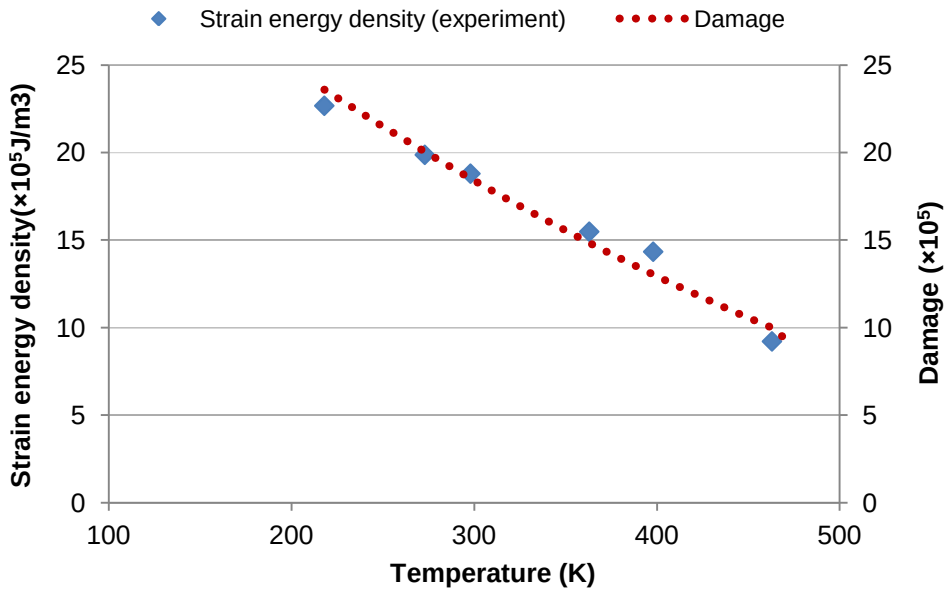

Figure 5.9: Comparison between the experimentally derived strain energy density and modelled damage with modified temperature hardening function

5.3 MODEL PARAMETER CALIBRATION

Now that the appropriate form of the model has been determined, this section concerns parameter calibration for the crack propagation part of the model. Model calibration is a task of adjusting the parameters of the model by reference to actual experimental input-output pairs in an attempt to optimize the agreement between model predictions and experimental observations.

In this section, model parameters are calibrated against four sets of shear force data for wire bonds under passive thermal cycling tests. Bond wear-out rate is obtained by the experimental data corresponding to these temperature profiles. Meanwhile, simulation is operated to predict bond shear strength degradation rate via evaluation of the damage in the wire material under the same loading conditions. Parameters are adjusted until the model outputs for the four temperature profiles all match the actual experimental data.

5.3.1 Shear force degradation data from thermal cycling tests

The existing shear force data are from the wire bond samples subjected to passive thermal cycling tests. The bond samples were fabricated with 99.999% (5N) aluminium wires, 375μm in diameter, ultrasonically bonded at room temperature to silicon dies coated with a 5μm thick aluminium top metallisation and bonded onto DBC substrate tiles, which were provided by Dynex Semiconductors Ltd. The bonded wires were then subjected to passive thermal cycling with four different ranges, namely -40°C to 190°C, -60°C to 170°C, -35°C to 145°C and -55°C C to 125°C. Four thermal cycling profile recorded from a thermocouple (attached to a substrate tile) are presented in Figure 5.9; these show that the specimens experienced a constant ramp rate of 11°C per minute during heating and 6°C per minute during cooling.

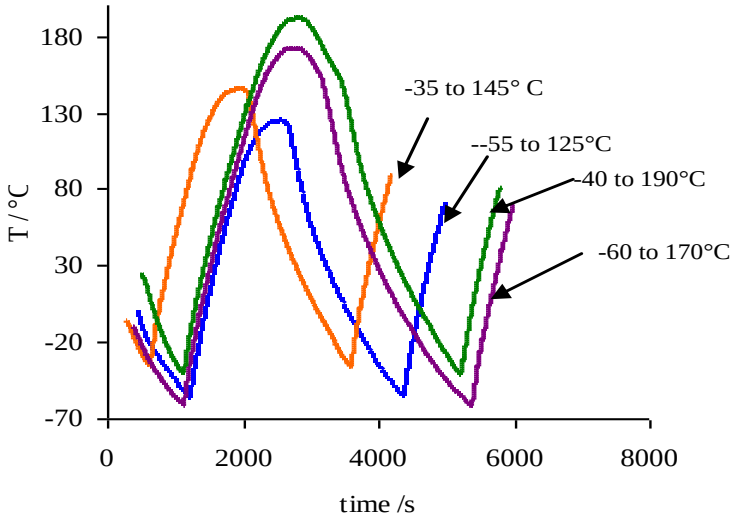

Figure 5.9: Passive thermal cycling profiles [118]

The degradation behaviour of the wire bonds was evaluated by means of bond shear force measurements at regular cycling intervals. The average values of shear force data and corresponding equations of trend lines were presented in Figure 5.10. Here the unit of shear force F_s is centi-Newton (cN).

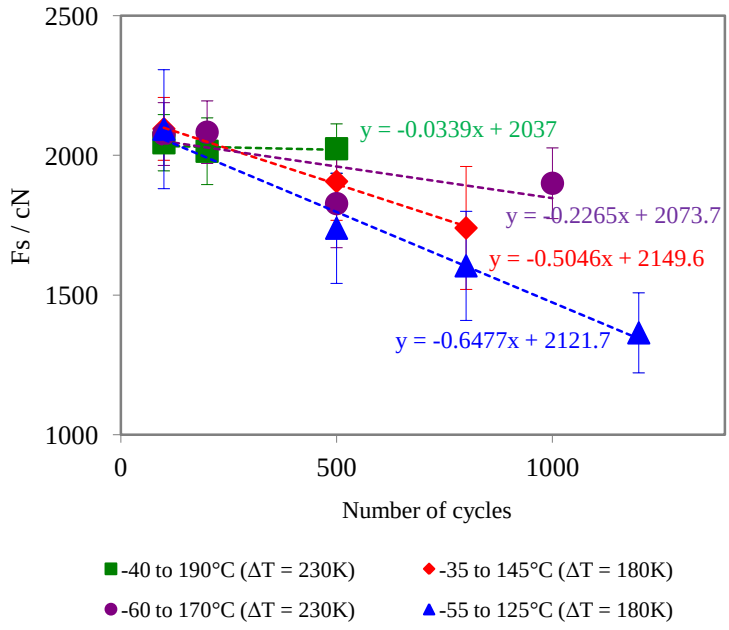

Figure 5.10: Development of bond shear force under passive thermal cycling [17]

During thermal cycling exposure, the experimental development of bond shear force can be expressed as:

$$F_s = F_0(1 - \beta \times n) \tag{5-12}$$

Where:

F_0	is the initial shear force
F_s	is the shear force after *n* cycles
β	is the shear strength degradation rate

Therefore the values of bond wear-out rate can be estimated from the slope of the trend lines as below:

Development of bond shear force: $F_s = F_0 - (F_0 \cdot \beta) \cdot n$

Trend line equation: $y = -m \cdot x + C$

In the trend line equations shown in Figure 5.10, variables *y* and *x* represents F_s and *n* respectively. The *C* value represents the initial bond shear force and the value of slope (*m*) corresponds to the production of "$F_0 \times \beta$". The values of β that indicates shear force degradation rate are calculated for the four temperature conditions on a per cycle basis and are listed in Table 5.3.

Table 5.3: Bond shear force degradation rate under four thermal cycling ranges

Temperature profile				**Shear force degradation rate**
Tmax (°C)	Tmin (°C)	ΔT (°C)	Cycling time (Sec)	β
-55	125	180	2800	-3.05×10^{-4}
-35	145	180	2800	-2.35×10^{-4}
-60	170	230	3600	-1.09×10^{-4}
-40	190	230	3600	-1.66×10^{-5}

5.3.2 Simulation of the development of bond shear force

Evolution of bond shear force is simulated by the operation of the damage-based crack propagation model under these four temperature loading conditions. The five variables in the model, i.e. G_0, α_H, β_H, β_T, k_2' are varied to identify their individual influence on the development of damage and thus the bond wear-out rate. These can be summarized as follows.

The work hardening term shapes the interface damage evolution curve. The extent of damage within the plastic zone governs the bond degradation rate and crack growth rate. Work hardening parameters α_H and β_H both influence the final damage value by means of multiplication and power relation respectively. α_H varies the time it takes to reach saturation and β_H varies the damage swing range during heating and cooling. The effect of loading temperature on the rate of damage accumulation is determined by temperature hardening exponent β_T. A change in damage coefficient G_0 has an overall effect on the scale of the bonding interface damage. In the annealing term, the value of k_2' influences the proportion of the damage annealed out during each time interval. In the last section, four parameters in the constitutive functions, i.e.: α_H, β_H, α_T, and β_T have been calibrated by the mechanical properties of the aluminium bond wires derived from isothermal tensile tests. The calibrated values of these parameters are applied to the crack propagation model.

Compared to isothermal tensile test, the annealing effect on the removal of the build-up strain is thought to be much more significant in under non-isothermal conditions, so the damage removal might be greater. Therefore in the case of passive thermal cycling the annealing coefficient k_2' is increased from 3×10^3 to 5.5×10^7.

The other model parameters are optimized against the experimental data to obtain the best fit. Bear the function of these parameters on the final value of total damage in mind, and due to the very fast simulation time it takes, the model parameters can be tuned through trial-and-fit method. Optimal values of all the model parameters and constants are listed in Table 5.4.

Table 5.4: The values of the model parameters employed in the simulation

Variables		Constants	
G_0	10	α_{Al}	23 µm/m/°C
α_H	40	α_{Si}	2.6 µm/m/°C
β_H	0.5	T_{eq}	90 °C
α_T	3.5	R	8.31447
β_T	1.8×10^{-3}	Q	84000J/mol
$k_2^{'}$	5.5×10^{7}	L	1000 µm
		W	375 µm

From Figure 5.10, it can be seen that the average initial shear force is approximately 2000cN for the bonded substrate samples. To obtain a comparison on the shear force degradation rate, the same initial value (2000cN) is employed in the implementation of the shear strength degradation model. Simulation results of the shear force degradation lines are shown in Figure 5.11, which is based on the time unit (second).

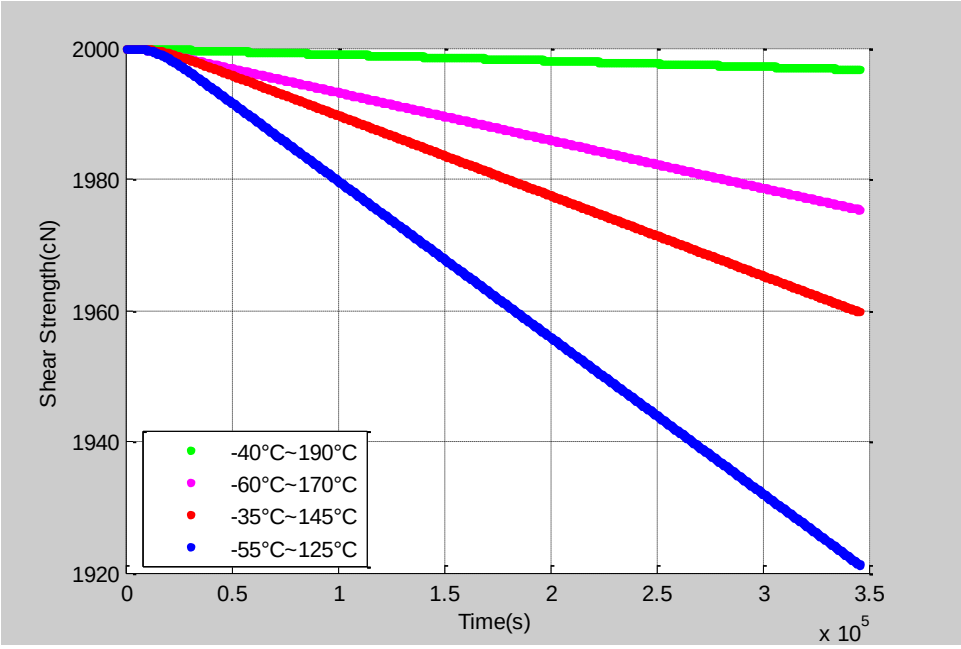

Figure 5.11: Simulation of the shear force degradation of Al wire bonds subjected to four temperature ranges

To obtain a comparison with the experimental data, the simulation values were converted into the unit of per cycle instead of per second and the results are listed in Table 5.5. The good agreement between the experimental data and simulation results implies that calibration of both the numerical representation and the model parameters has been accomplished.

Table 5.5: Comparison of bond shear force degradation rate between experimental data and simulation results

Temperature range	**Rate of shear force degradation** (per cycle)	
	Experimental data	Simulation results
-55°C ~ 125°C	-3.05×10^{-4}	-3.71×10^{-4}
-35°C ~ 145°C	-2.35×10^{-4}	-2.27×10^{-4}
-60°C ~ 170°C	-1.09×10^{-4}	-1.07×10^{-4}
-40°C ~ 190°C	-1.66×10^{-5}	-1.95×10^{-5}

5.4 SUMMARY

This chapter concerns the verification and calibration of the proposed damage-based crack propagation model. In the first part, the model is verified by quantitatively linking the damage parameter to plastic strain energy derived from the isothermal tensile tests which were performed for pure aluminium (99.999%) bond wires under various temperatures and strain rates. Plastic strain energy was evaluated from the corresponding flow curves. The constitutive material representation is extracted from the crack propagation model and the temperature hardening function is modified by comparisons between simulated strain-induced damage and experimentally derived strain energy density. The power law relationship of accumulated damage with loading temperature is replaced by a linear relation to fit the linear distribution of the strain energy values obtained experimentally.

In the subsequent section, the adjusted constitutive model was put back in the crack propagation model. Then the whole model was calibrated against the bond wear-out data collected from passive thermal cycling experiments under four different temperature profiles. The bond degradation rates were estimated via the damage-based crack propagation model and the values of the model parameters were determined by optimally curve fitting the experimental results.

CHAPTER 6

SIMULATION OF BOND DEGRADATION BEHAVIOUR AND LIFETIME PREDICTIONS

6. 1 INTRODUCTION

In order to relate model parameters to physically quantifiable properties, isothermal uniaxial tensile tests have been carried out to characterize the fundamental mechanical properties of bond wire materials. The details of the test procedure and experimental results have been presented in Chapter 5. A quantitative link is made between parameter damage and strain energy density and the form of the model functions have been adjusted accordingly. Meanwhile the parameters in the damage-based crack propagation model have been calibrated by the existing data of wire bond shear force degradation rates collected from accelerated passive thermal cycling tests under four temperature ranges.

The major advantage of the proposed time-domain model over cycle-based lifetime models for wire bonds is that it is able to more accurately reflect the influence of high maximum loading temperatures and the corresponding temperature-time effects on the wear-out behavior of wire bonds. The predictions on lifetime and wear-out rate made by simulation are supposed to be able to represent these advantages.

In this chapter, the damage-based crack propagation model is operated to simulate the evolution of damage in the aluminum bond wires during thermal cycling. Predictions on lifetime and wear-out rate are made under various

temperature loads to examine the performance of the model.

6.2 SIMULATION ON THE EVOLUTION OF TOTAL INTERFACE DAMAGE AND BOND DEGRADATION

6.2.1 Effect of time-at-temperature on damage accumulation

In the proposed time-domain damage-based model, bond degradation rate is the combined result of damage accumulation and damage removal. The balance between damage accumulation and damage removal will be determined by the time spent at temperature and not just by the temperature range or the maximum temperature. The most fundamental expectation from the model is that it is able to more accurately reflect the temperature-time effects on bond degradation rate.

Therefore, in the simulations three temperature loads are defined with different time features which can be achieved by either including dwell at peak temperatures or changing ramp rate of heating/cooling stages. The definitions of the three profiles, namely A, B and C, are listed in Table 6.1.

Table 6.1: Temperature profiles with different time features

Temperature amplitude	Cycling time	Ramp rate	Dwelling time
A: -55°C ~ 125°C	1800 seconds	12°C/minute	No dwell
B: -55°C ~ 125°C	3600 seconds	6°C/minute	No dwell
C: -55°C ~ 125°C	4350 seconds	6°C/minute	750 seconds*

*Dwelling at 125°C for 750 seconds.

In Figure 6.1 ~ 6.3, the three temperature profiles and the evolution of total interface damage corresponding to these temperatures are illustrated. It can be seen that the rate of change of damage and the saturation values vary under these three temperature loads due to the time effect.

Slower heating and cooling rate means longer exposure duration at temperatures, and this determines the extent of annealing and hence the annihilation of the damage.

Load B has lower frequency than load A thus damage removal effect is more significant under load B. It can be seen that the damage accumulation and removal processes during cooling and heating regimes are different between the two loads. And the saturation value of total interface damage induced by load B is smaller than the damage value under load A. Furthermore, the predicted wear-out rate under load B should be slower than the one under load A. In like manner also, introduction of the dwell times at maximum temperatures means the exposure time at high temperature is prolonged. As the result, load C that has 750 seconds soaking time at T_{max} (125°C), would induce less net damage and slower wear-out rate compared with load B.

According to the analysis on the evolution of damage, the bond shear force degradation rates under load C, B and A should be in a descending order. Figure 6.4 shows the simulation results for the rate of shear force degradation under the three loads. It clearly demonstrates the descending order for load C, B and A.

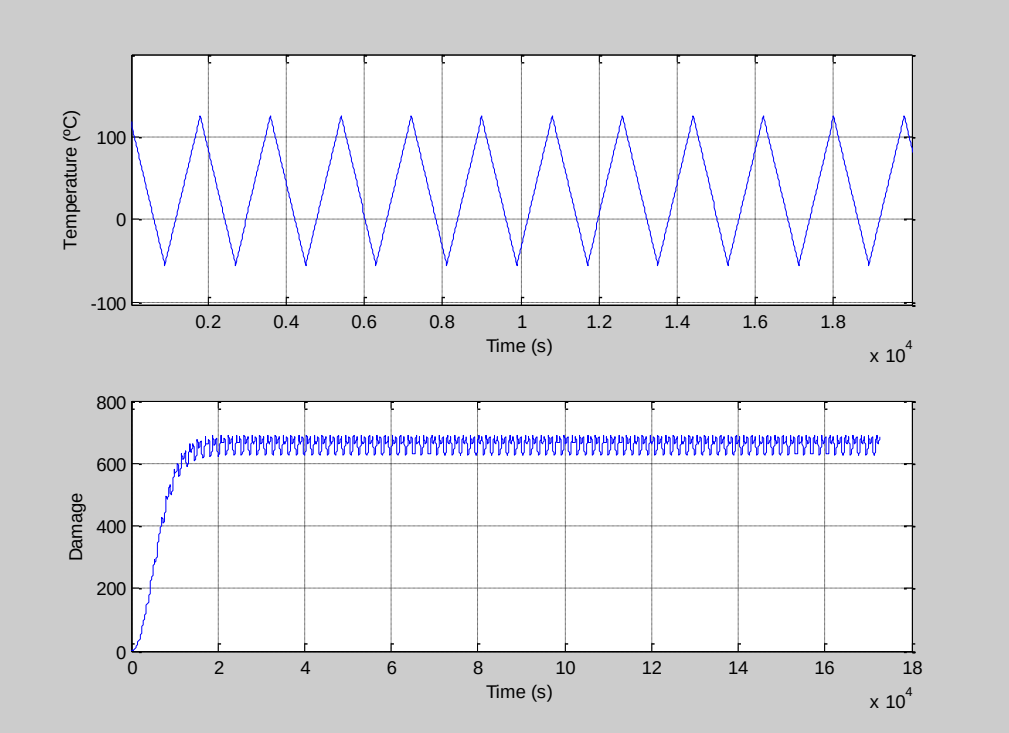

Figure 6.1: Temperature profile of load A and the evolution of total interface damage

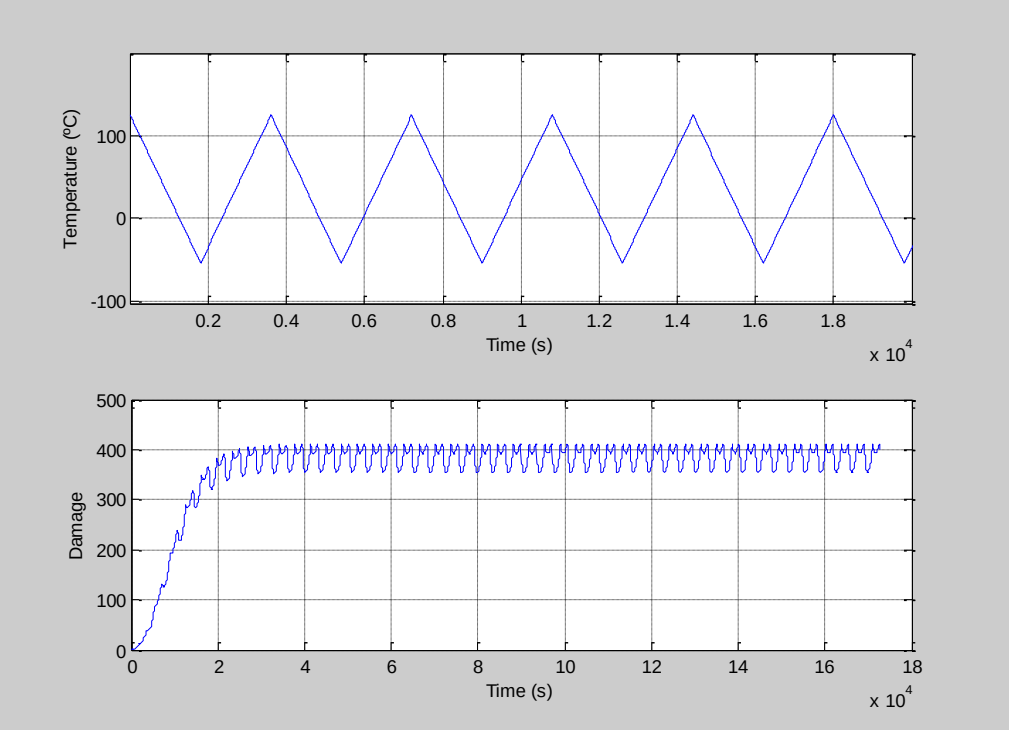

Figure 6.2: Temperature profile of load B and the evolution of total interface damage

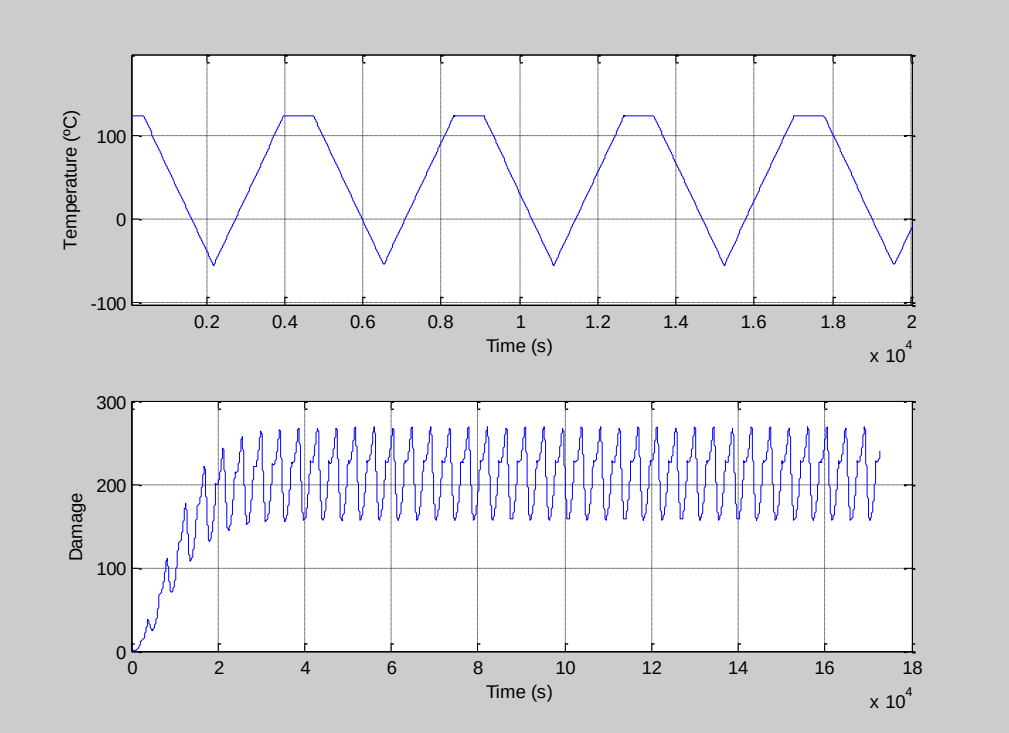

Figure 6.3: Temperature profile of load C and the evolution of total interface damage

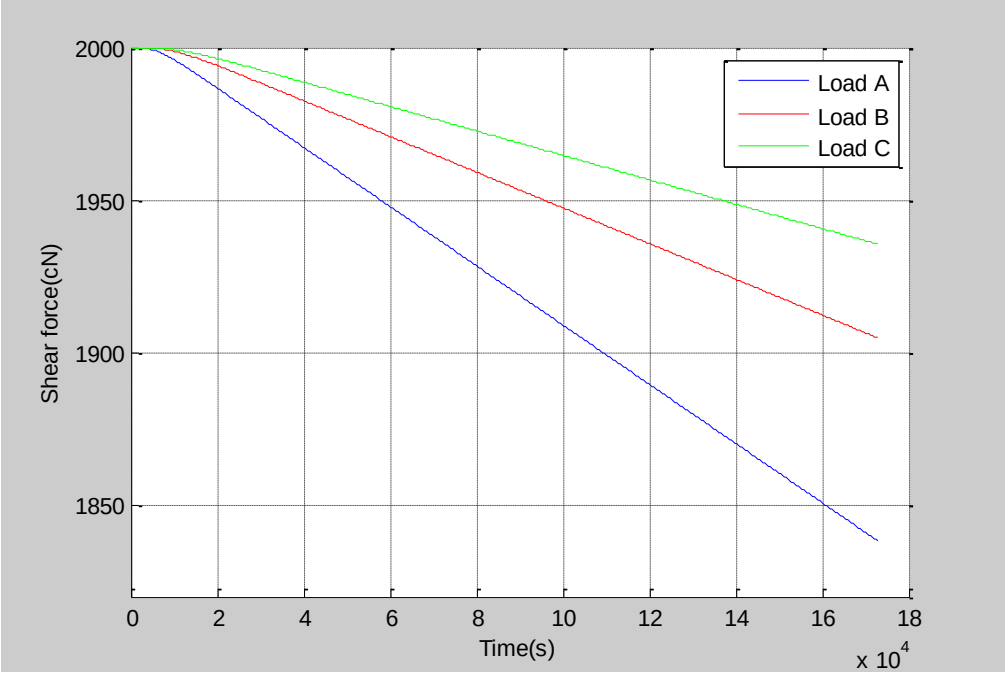

Figure 6.4: Degradation of the shear force under Load A, B and C

6.2.2 Influence of maximum temperature

The onward development of the time-domain model is motivated by reference to some unusual observations from both our own experiments and those reported in the literature. The common point in these experimental works is that in the case when the maximum temperatures are relatively high, the exposure to these higher temperatures does not necessarily lead to faster degradation despite that the higher maximum temperatures lead to larger temperature ranges.

Further investigations on the evolution of the microstructure of the wire bonds during thermo exposures have revealed that significant annealing occurs during thermal cycling regimes with high T_{max} values. These thermally activated processes which take place within wire bonds of high purity aluminum at elevated temperatures lead to the removal of some of the build-up damage and a consequent reduction in the rate of crack propagation which is beneficial in terms of their reliability.

In the new time-domain model, this damage removal effect related to high temperatures is taken into account. This section concerns the simulation predictions from this point of view by varying T_{max} values whilst fixing the T_{min} value. It's well known that engineering materials creep become significant at homologous temperatures equal to or greater than 0.3. Homologous temperature is defined as the ratio of the absolute temperature to its absolute melting temperature. The equilibrium temperature is selected as 90°C whose homologous temperature is 0.4 for pure aluminum. Three different T_{max} (above 90°C) is set up for the simulations whist minimum temperature keeps the same value. The definitions of the three profiles, namely D, E and F, are listed in Table 6.2.

Table 6.2: Temperature profiles with different T_{max}

Temperature amplitude	Cycling time	Ramp rate	Dwelling time
D: -55°C ~ 90°C	2900 seconds	6°C/minute	No dwell
E: -55°C ~ 140°C	3900 seconds	6°C/minute	No dwell
F: -55°C ~ 160°C	4300 seconds	6°C/minute	No dwell

Exposure to the higher maximum peak temperature brings about more significant damage removal during thermal cycling due to annealing processes, resulting in slower wear-out rate of the wire bonds. The three temperature profiles defined in Table 6.2 and the evolution of the total interface damage corresponding to these temperatures are shown in Figure 6.5 ~ Figure 6.7. It can be seen that the evolution of the total interface damage and the saturation values of total damage are different from each other for the three loads. Obviously, the saturation value of damage under loading temperature with the higher T_{max} is smaller despite the fact that the amplitude of fluctuation of damage under larger temperature range (ΔT) is wider.

As the result, the rate of shear force degradation decreases as the T_{max} increases. The predictions of the degradation of the shear force under these three temperature loads are presented in Figure 6.8.

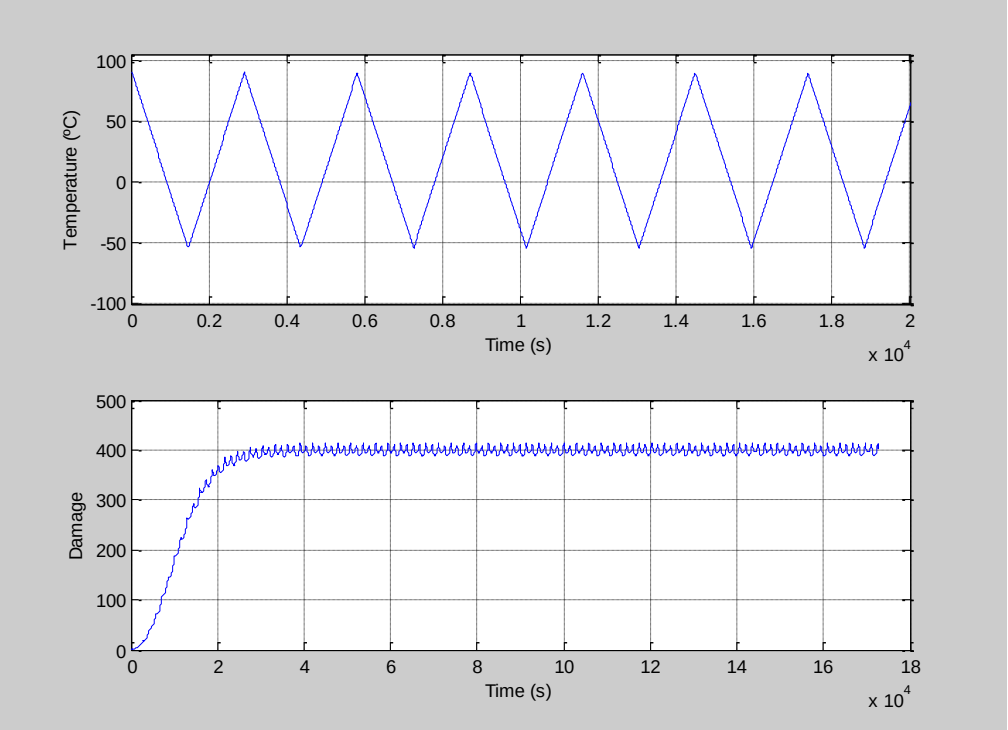

Figure 6.5: Temperature profile of load D and the evolution of total interface damage

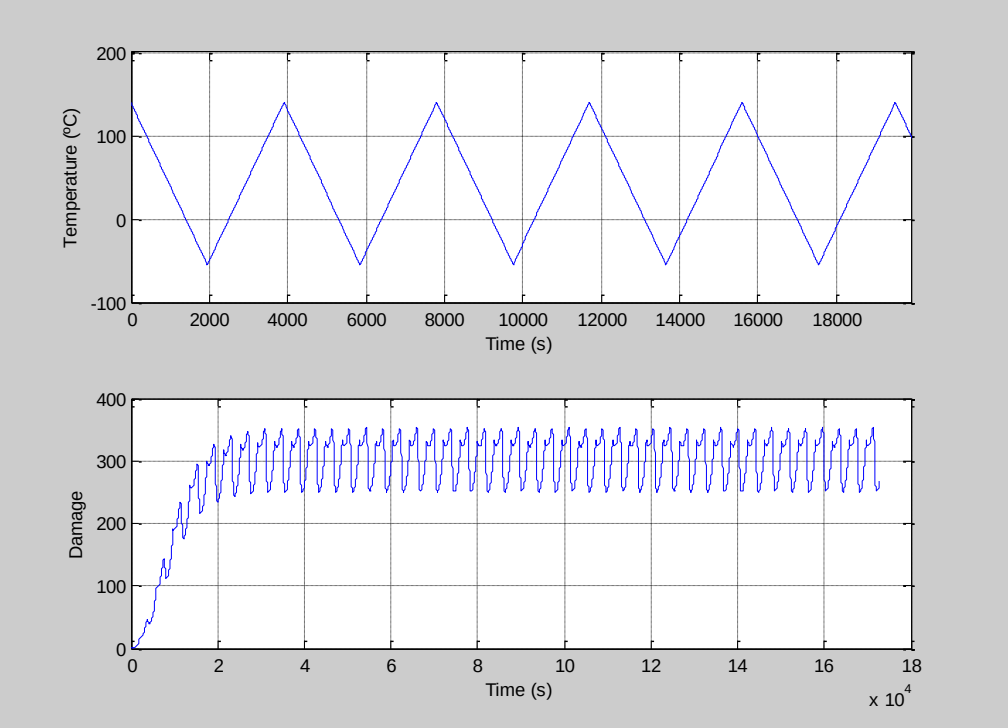

Figure 6.6: Temperature profile of load E and the evolution of total interface damage

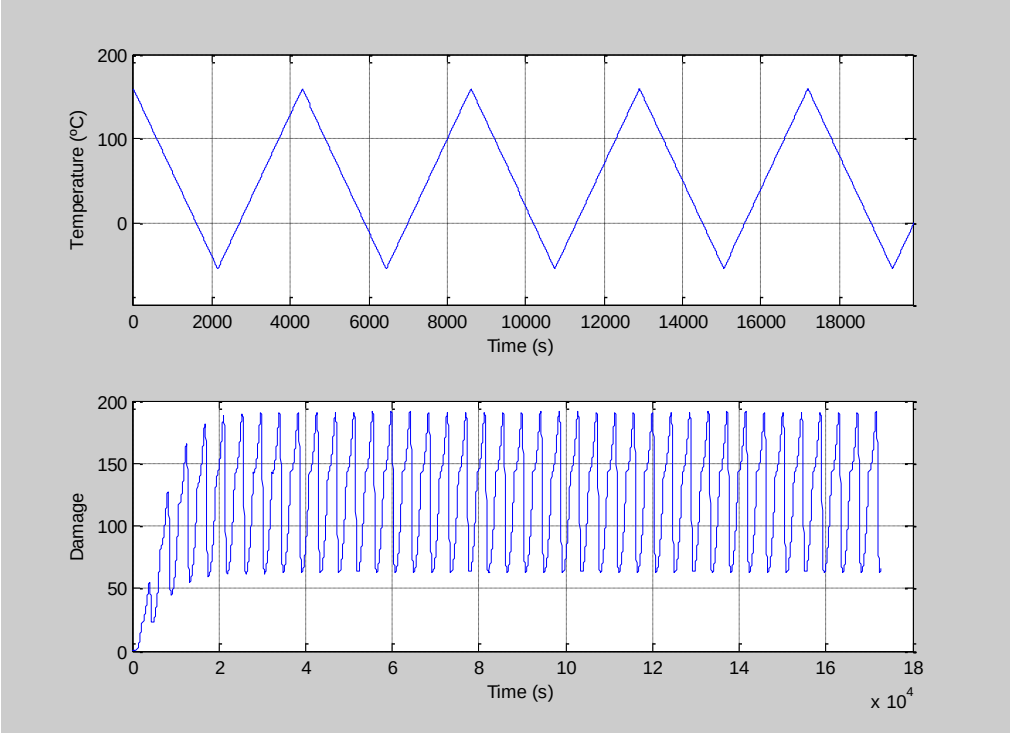

Figure 6.7: Temperature profile of load F and the evolution of total interface damage

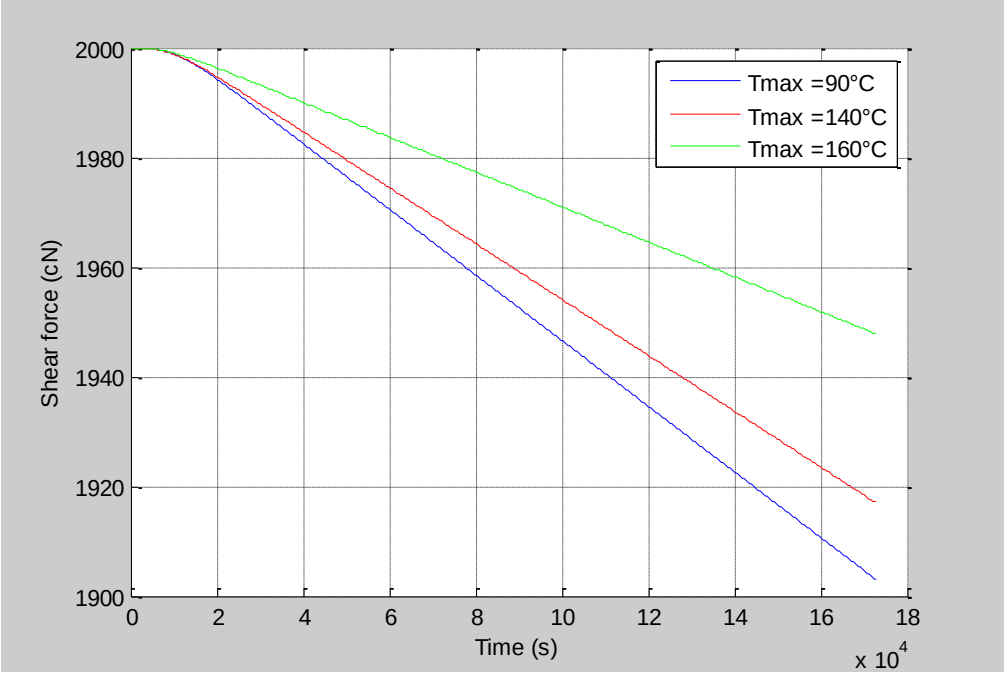

Figure 6.8: Degradation of the shear force under Load D, E and F

6.2.3 Influence of minimum temperature

Prior to thermal cycling, bonded wires contain a certain amount of damage that is brought about by deformation-induced work hardening as a result of the ultrasonic energy and force during bond formation. Under thermal cycling, damage builds up in the wire material adjacent to the bonding interface. The extent of damage is affected by the minimum temperature to which the bonds are subjected. On the other side, the process of grain recovery and recrystallization is thermo dynamically driven. The rate and degree of the damage removal also depends on the amount of damage that already exists in the material. Damage is related to dislocation density; bonds experience a degree of 'cold work' during the low temperature phase of a cycle, especially one which involves sub-ambient temperatures (thereby increasing dislocation density and thus damage). Minimum temperature is therefore an important factor that determines the amount of damage as well as the rate of accumulation of damage in the wire material during thermal cycling.

In the proposed model, the influence of the temperature on work hardening is accounted for by the temperature hardening function in damage accumulation term; and in the damage removal term the existing damage is one of the factors making up the annealing function. Therefore the damage-based model should be able to represent the effect of T_{min} on the bond shear force degradation rate. This is accomplished by varying the values of T_{min} whilst fixing the T_{max} value.

Accordingly three profiles are defined and listed in Table 6.3., namely G, H and I.

Table 6.3: Temperature profiles with different T_{min}

Temperature amplitude	Cycling time	Ramp rate	Dwelling time
G: -20°C ~ 125°C	2900 seconds	6°C/minute	No dwell
H: 10°C ~ 125°C	2300 seconds	6°C/minute	No dwell
I: 40°C ~ 125°C	1700 seconds	6°C/minute	No dwell

It is expected that the bonds exposed to lower minimum temperature exhibit more amount of accumulated damage and hence faster wear-out rate. It can be seen from Figure 6.9 ~ 6.11 that the saturation value of damage decreases as T_{min} increases. Figure 6.12 shows that the bonds subjected to higher T_{min} degrades more slowly.

Also evident from Figure 6.9 ~ 6.11 is that there are no wide fluctuations in the change of damage during temperature cycling under the above three conditions. This is because the maximum temperature of 125°C is not quite high enough for a significant annealing effect.

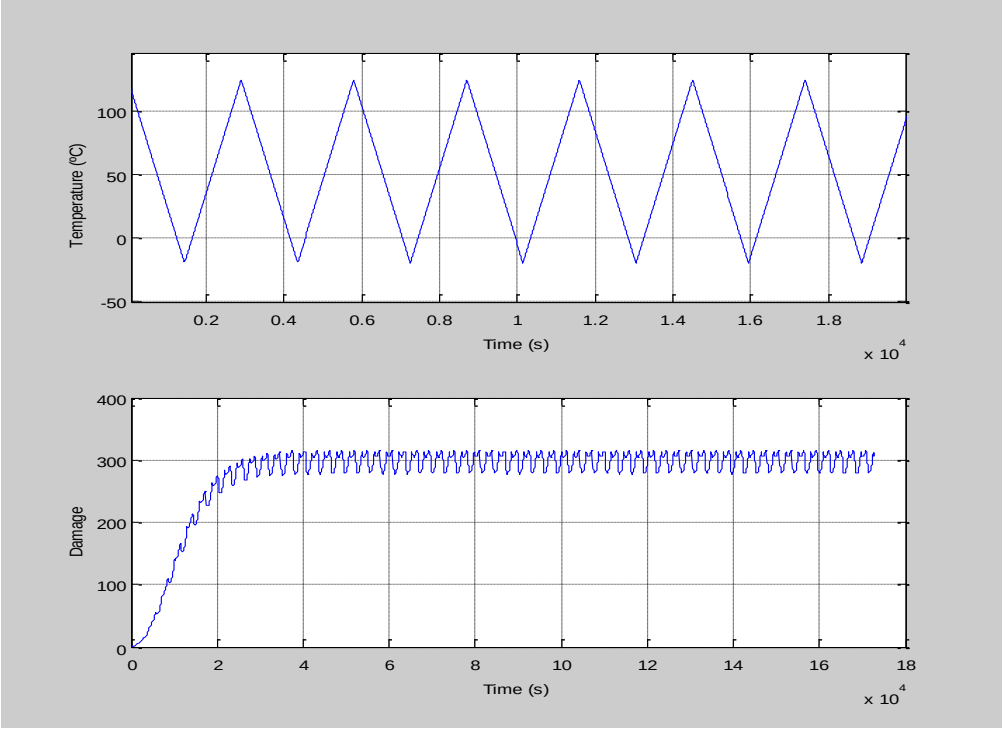

Figure 6.9: Temperature profile of load G and the evolution of total interface damage

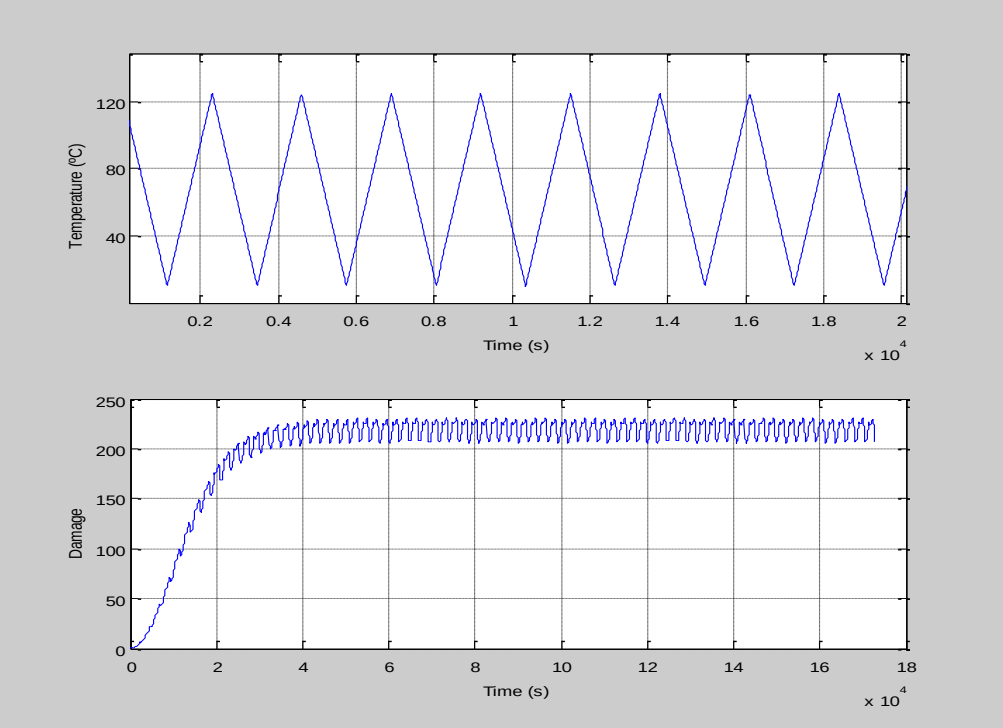

Figure 6.10: Temperature profile of load H and the evolution of total interface damage

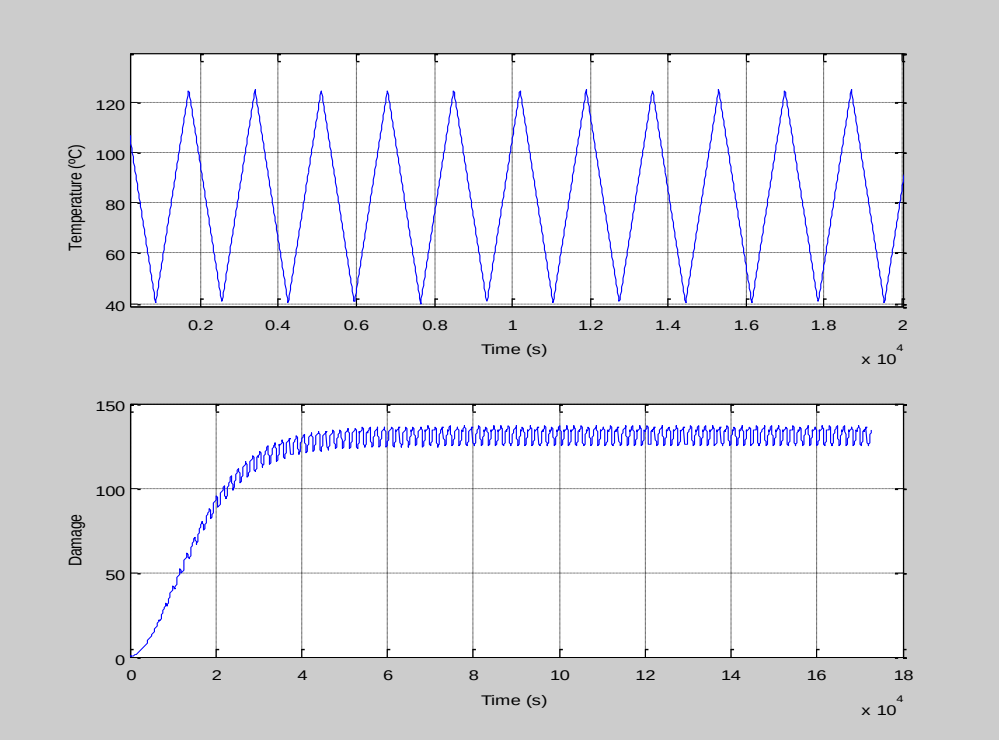

Figure 6.11: Temperature profile of load I and the evolution of total interface damage

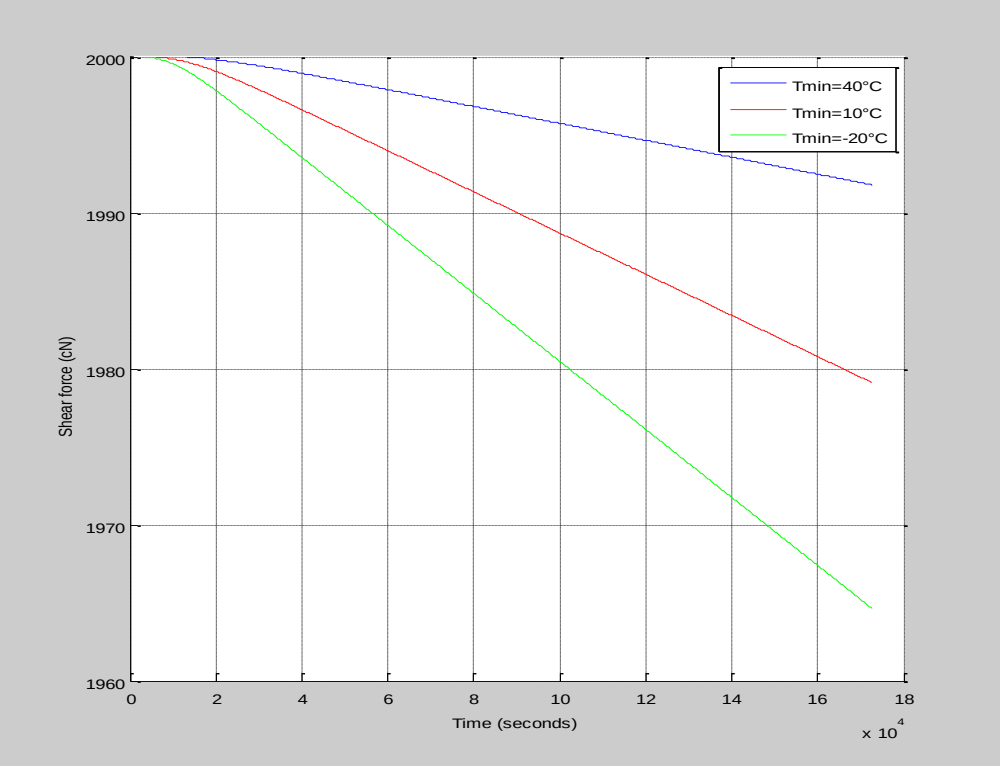

Figure 6.12: Degradation of the shear force under Load G, H and I

6.3 LIFETIME PREDICTION

In Chapter 5, the unusual observations in the wear-out of high-purity aluminum wire bonds under extended range passive thermal cycling was discussed by means of shear strength degradation. The corresponding experimental lifetime data was provided in [118]. It was shown that the number of cycles to failure (N_f) increases when ΔT is above a certain value. However, according to Coffin-Manson based models such as Equation (3-4) and Equation (3-5), N_f decreases as ΔT increases. Obviously, by simply employing Coffin-Manson law, it is not able to predict these unusual lifetime observations under larger ΔT.

In this section, lifetime prediction is being made for thermal cycling conditions under various temperature ranges which are obtained by varying the maximum temperature with a fixed value of -55°C for minimum temperature. The damage-based crack propagation model is operated and the development of the shear force versus time can be simulated. If a 50% decrease of the shear force

is applied as the failure criterion, the time to failure under a certain temperature load can be predicted.

The simulation results are shown in Figure 6.13. It can be seen that under small temperature ranges, or in other words, when the maximum temperature is relatively low, the lifetime falls as the temperature difference ΔT increases as creep processes are not dominant in these temperature regimes thus the damage removal effect is negligible. Fatigue is the primary wear-out mechanism so temperature amplitude plays the main role in determining lifetime.

Under the extended temperature ranges that correspond to higher maximum temperatures, the predicted lifetimes present an ascending trend which agrees with the high-temperature related and aforementioned apparently anomalous experimental observations. Furthermore, it can be seen that there is a threshold value of ΔT (approximately 180K) above which the effect of damage removal phenomena on the lifetime start to become significant and consequently increasing ΔT results in increase in N_f. .

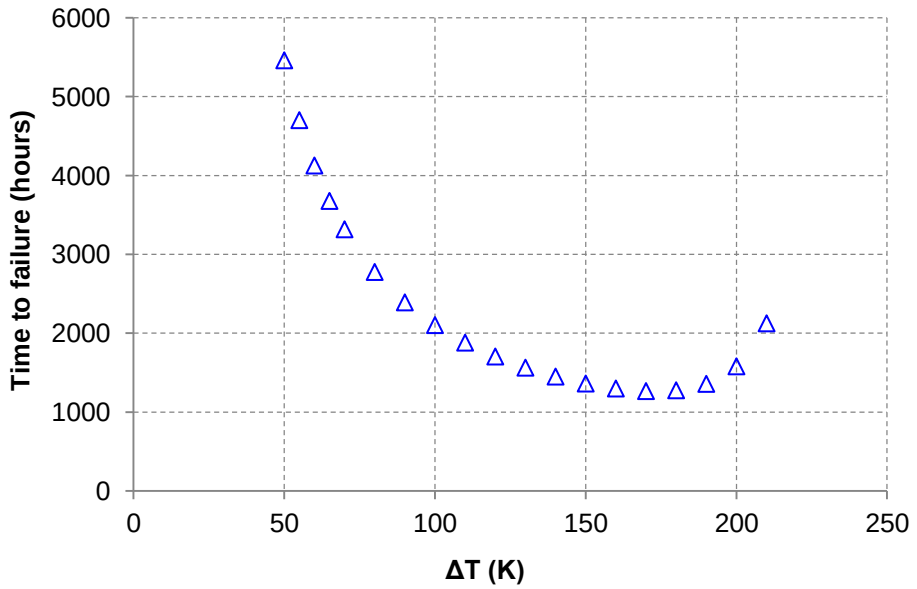

Figure 6.13: Lifetime prediction for thermal cycling with fixed T_{min}=-55°C

6.4 SUMMARY

In this chapter, the proposed time-domain model has been operated in MATLAB environment to check the performance of the model mainly from two aspects: the influence of maximum temperature and the time at temperatures. These effects are achieved by defining a variety of loading temperature profiles including changing the time feature of the profile and varying the maximum temperatures. The simulation has been carried out on the total interface damage model and evolution of the shear force under specific loading temperatures. The results have shown that the damage model can demonstrate both the damage accumulation and damage removal processes corresponding to the low temperature and high temperature regimes. And the model is also able to reflect the temperature-time impact and related high temperature effects on the shear force degradation rate.

At the end, the lifetime prediction has been made for extended temperature ranges via the evaluation of shear force wear-out rate by the damage-based crack propagation model. A series of temperature ranges are obtained by varying maximum temperature with the minimum temperature fixed at -55°C. The simulation results have demonstrated that the proposed model is able to represent the lifetime performance under both conventional temperature loads and also high temperature regimes and they are in agreement with the high temperature related experimental observations.

Above all, the simulation results have shown that the model can perform as anticipated. In next chapter, the crack propagation model is validated by passive thermal cycling data. Frequently employed accelerated testing approaches to reliability assessment of power electronic devices are introduced and the ongoing experimental work is described including the purpose, design and implementation procedures. The experiment result and validation are analyzed as well.

CHAPTER 7

MODEL VALIDATION BY ACCLERATED TESTS

7. 1 INTRODUCTION

Model validation is the essential part in the process of model development. Once satisfactory estimation of the parameters for the model has been obtained, the model must be checked to assure that they adequately perform the functions for which they are intended. This process aims to validate whether the model is a reasonable representation of the actual fact. Meanwhile it allows quantification of the accuracy of the model prediction through comparisons between experimental data and simulation outcomes from the computer model. Through this step, a better understanding can be achieved on the model's capability and limitations that enables to address a range of important issues.

In Chapter 6, the damage-based crack propagation model has been implemented in MATLAB to predict the wire bond shear force degradation rate under different loading temperatures. A variety of temperature profiles are defined to characterize the impact of T_{max}, T_{min} and time-at-temperatures. The simulation results have shown that the proposed time-domain model can reflect the influence of temperature extremes as well as the time features of the loading temperatures on the bond wear-out rate.

This chapter concerns model validation which requires comparing the experimentally obtained wear-out rates to the simulated results under the same loading conditions. To this end, accelerated tests need to be carried out to get

wear out information and lifetime data for the wire bond samples.

In the sections that follow, relevant accelerated tests that are frequently used for the reliability assessment of power electronic modules are introduced. Design and setups of the accelerated tests are described in details. The available experimental data and validation results are also discussed.

7.2 ACCELERATED TESTS

Accelerated stress testing has been recognized to be a valuable method to assess reliability and validate model predictions in a timely manner. The tests are often carried out under increased or exaggerated environmental conditions to enhance the damage accumulation rate due to any physical or environmental phenomena in the product.

Temperature is so far the most common stress applied to age power module packaging assemblies for the degradation or failure characterization of devices and interconnections. It is well accepted that fluctuating temperature is the primary attribution to the thermo mechanical stresses at joining interfaces due to mismatched thermal expansion coefficient of the packaging materials between adjacent layers and eventually leads to fatigue failure. Therefore the wear-out performance of the packaging materials under accelerated cycling between two temperature extremes provides a direct relationship to reliability over time. Passive thermal cycling and active power cycling are the most frequently used methods to introduce temperature variations.

During thermal cycling tests, the samples are placed in an environment chamber and cycled through two temperature extremes at an accelerated rate with desired temperature profiles. Tested samples are taken out in the intermediate stage of the cycles and the physical parameters such as shear strength, crack length or material properties can be measured to record the degradation behavior wear-out rate of the bonds and investigate the evolution of the material microstructure.

Failure acceleration due to temperature cycling depends on three following factors: the magnitude of the high and low peak temperatures; the transfer time between the two temperatures; and the soaking times at the peak temperatures. Definition of the thermal profile includes the temperature extremes, ramp rate and dwell times. Figure 7.1 demonstrates the definition of a typical temperature profile from thermal cycling chamber.

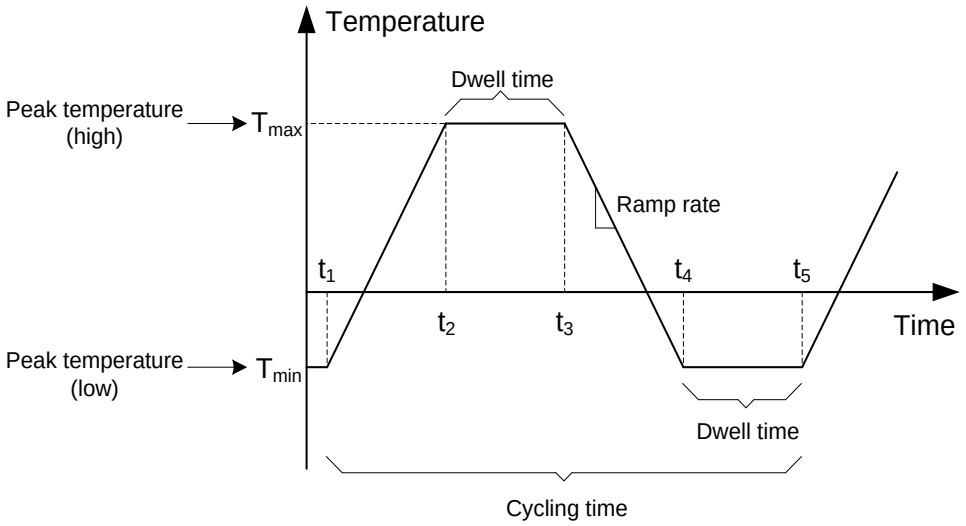

Figure 7.1: An example of thermal cycling temperature profile

A big advantage of thermal cycling test is that loading temperature profile can be easily shaped as required. And the upper and lower temperature boundaries are comparatively broad in contrast to power cycling tests. Also the tested devices do not need to be electrically functional during thermal cycling so this kind of accelerated testing can be used for the assembly parts reliability assessment. However thermal cycling testing is a time consuming procedure. The unit of one cycle usually counts with tens of minutes. Obvious failures can only be quantified after more than one thousand cycles. Consequently for one testing temperature profile it takes a few months in order to achieve sufficient data.

Active power cycling test is fundamentally different from passive thermal cycling test. It is performed by actively conducting current through power devices and the devices under test are mounted on a heat sink as in a real application. Figure 7.2 gives an example of operating conditions of power cycling tests. Devices heat up and cool down through alternatively switching on and off the current.

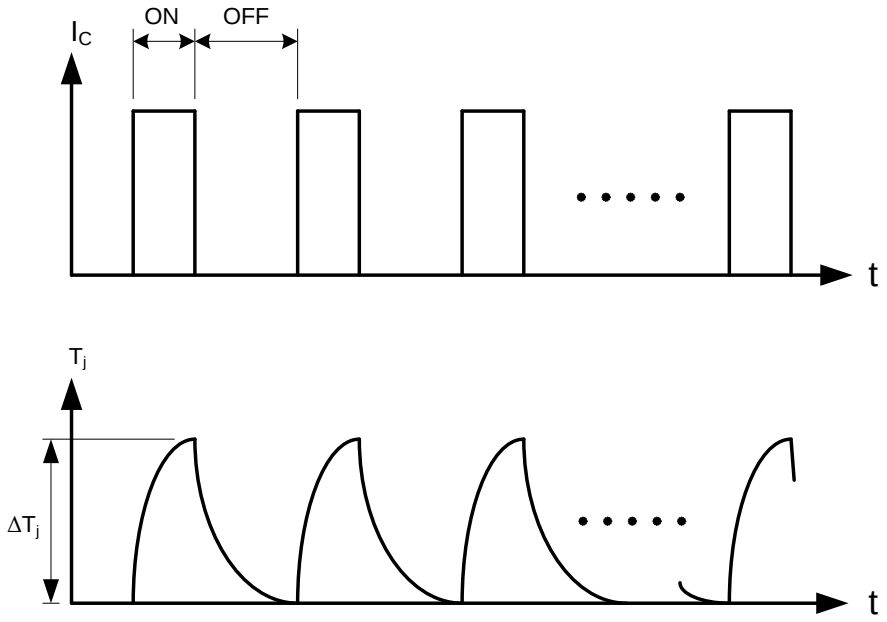

Figure 7.2: Operating conditions of power cycling tests

The devices are heated by the power losses generated in semiconductor chips and sometimes temperature sensors are used to monitor the temperature information. When the maximum target temperature in a chip is reached, the load current is switched off until the device cools down to a minimum temperature. The reaching of the minimum temperature completes the cycle and the next cycle begins by switching on the load current again. This cycling is repeated until the device fails. The electrical parameters such as on-state voltage/current, forward voltage and gate threshold voltage are continuously monitored or periodically measured during power cycling as the aging

indicator. Thermal resistance can be calculated by these values. The failure criterion is defined by the change of these parameters. Usually, a sudden leap in the forward voltage of the tested devices indicates a single bond lift-off and progressive increase of thermal resistance is a sign of solder fatigue.

Power cycling is more approximate to the real operational conditions for power devices. And in contrast to thermal cycling it takes much shorter time to obtain lifetime data as the period of one cycle in power cycling test is around a few seconds.

However, the temperature boundaries, especially the lower value is rather limited. Therefore the temperature variations provided by power cycling tests are relatively small compared with thermal cycling tests. And as the loading temperatures are controlled by switching on/off the current on the device, the shape of the temperature profiles are relatively monotonous. In other words, it is not easy to specify the ramp rate between two temperature extremes or include particular dwell times.

Alternatively, accelerated mechanical stress test is also an approach to reliability evaluation. They sometimes are performed to simulate the thermo mechanical strain generated by temperature fluctuation. In this case, mechanical stress was applied by cyclic lateral displacement of one bonding foot while fixing the other. This can shorten the duration of the testing time by overcoming the limitation of the testing frequency of power cycling. However, this is an inadequate representation of the actual loading conditions for power electronic modules during operation. In other instances, pure mechanical tests are needed to study the package endurance against handling damage, drop shock with the increase use of the mobile electronic products [116]. In this kind of tests, a cyclic mechanical load such as bending, twisting or vibration, is applied on the specimen to produce mechanical fatigue failures.

In this work, thermal cycling and power cycling tests are mainly concerned to characterize the wear-out behavior and obtain lifetime data of the wire bonds.

7.3 MODEL VALIDATION USING PASSIVE THERMAL CYCLING RESULTS

7.3.1 Experiment setup

7.3.1.1 Overview

In this work, there are three main tasks to be accomplished by accelerated thermal cycling tests.

- Validate the proposed model, i.e. whether the predictions on the lifetime and degradation rate made by the model are able to agree with the experimental results.
- Investigate the reliability behaviour of the wire bonds under various temperature loads.
- Investigate the influence of thermally activated processes and temperature-time effect on the wear-out rate of the wire bond interconnects.

During the tests, wire bond samples are subjected to specific temperature loads in an environmental chamber. Destructive bond shear testing was performed to measure the strength of the bonds in regular intervals throughout thermal cycling.

The wear-out rate of the wire bonds can be obtained by the shear force data and then be used to compare with the simulation predictions. In the meantime, part of the cyclic stressed bond samples will be undertaken FIB imaging and nanoindentation hardness analysis to further characterize the evolution of microstructure during thermo mechanical exposure and its influence on reliability. The flow diagram of the thermal cycling test procedure is shown in Figure 7.3.

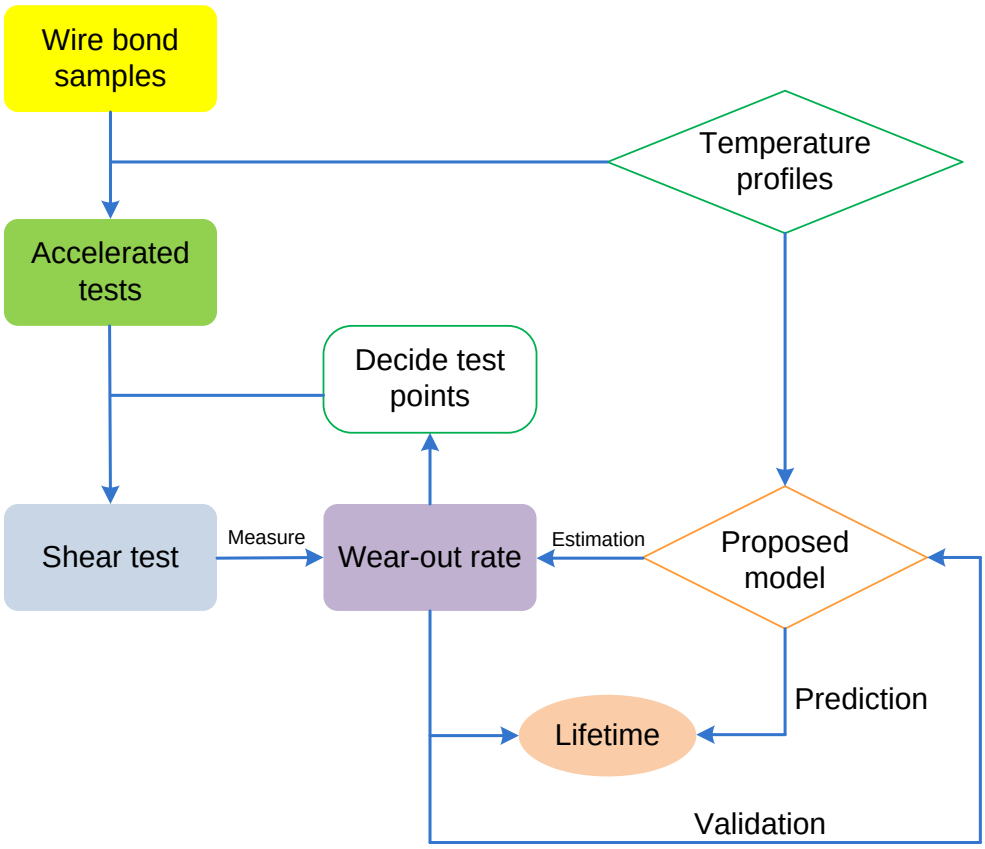

Figure 7.3: Flow diagram of the thermal cycling test procedure

7.3.1.2 Wire bond samples

99.999% (5N) pure aluminum wires, 375µm in diameter, ultrasonically bonded at room temperature to silicon dies coated with a 5µm thick aluminum top metallization and bonded onto DBC substrate tiles (AlN) were provided by Dynex Semiconductors Ltd.

On each substrate, there are four silicon dies with ten sets of wedge bonds on each die. One set of bonds include ten first bonds and ten stitch bonds on one silicon chip, as well as ten substrate bonds on the DBC substrate. The positions corresponding to each type of bonds are marked in Figure 7.4. Each substrate was cut into halves to get twenty bonds on one test specimen. At the determined points, one half-substrate is taken out. Sixteen bonds were shear tested and the other four bonds underwent indentation hardness measurements

and microstructure investigation.

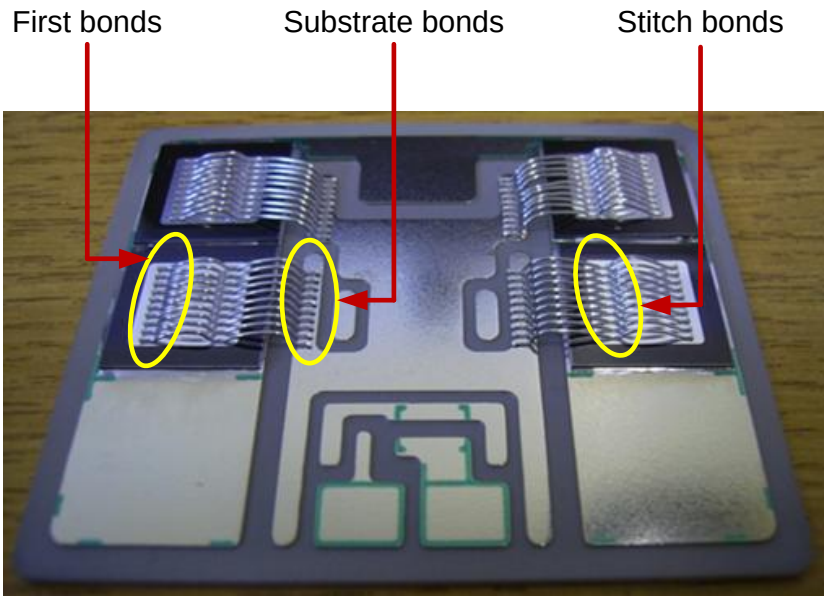

Figure 7.4: Photo of a substrate with wire bonds

7.3.1.3 Shear test

Bond shear force is used as the physical indicator to assess the bond degradation rate, which is usually measured by destructive bond shear test. When conducting shear test, the chisel-shaped shearing tool is positioned manually beside the bond to be tested. Once positioned, the unit proceeds automatically to perform the testing operation. The shearing arm moves the tool to a defined height above the bonding interface and horizontally shears through the bond. The force needed to shear the bond off its bonded pad, known as the bond shear force is then measured by the bond shear tester. The schematic diagram in Figure 7.5 has shown the principle of shear testing.

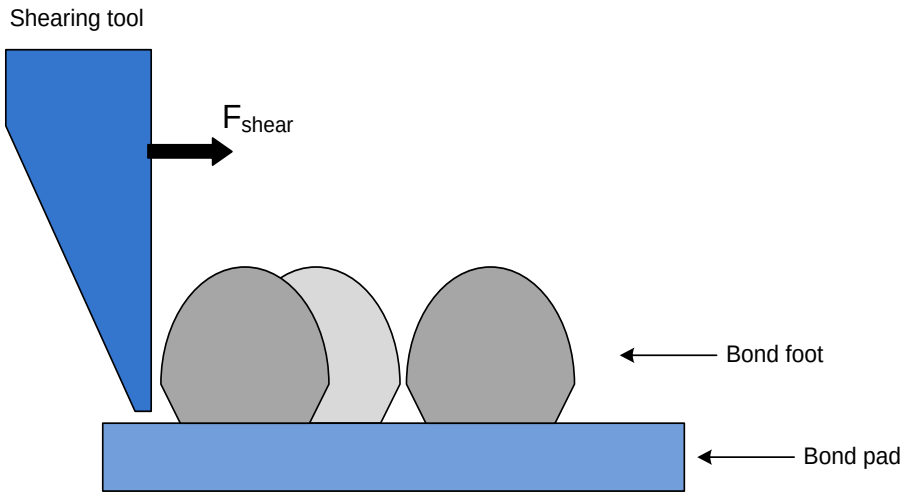

Figure 7.5: principle of shear test

Using the model that we have calibrated against the existing experimental data, the total projected time for the testing can be worked out. The estimated wear-out rate by the simulation can provide a reference of the points at which the samples are taken out for shear test. Experimental wear-out rate of the wire bonds corresponding to each temperature loads is obtained by the measured shear force data and then can be used to validate the proposed model.

In this work, shear tests are carried out with the Pull / Shear tester 5600 from F&K Delvotec. The shear testing parameter setup is shown in Figure 7.6.

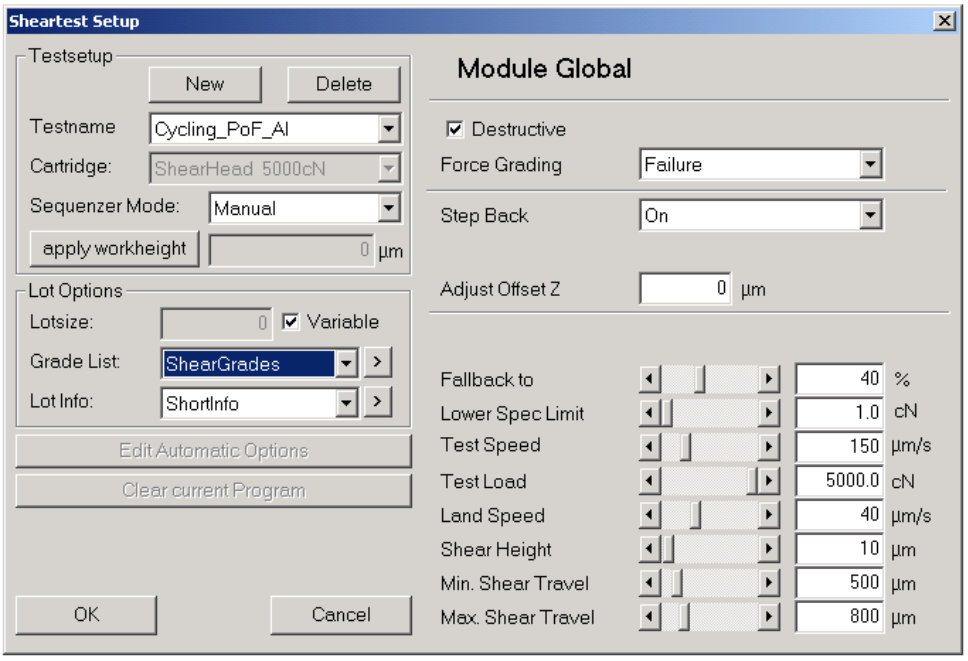

Figure 7.6: Shear testing parameters

7.3.2 Design of the temperature profiles

Thermal cycling tests have been carried out in the University of Nottingham by using Eurotherm Environmental Chamber which allows maximum and minimum temperatures at 400 °C and -70 °C respectively. Temperature cycles were programmed via Eurotherm itools software.

One thermocouple was connected to the substrate to monitor the chip temperature and the other one was exposed to the air inside the chamber. The bond samples were placed on the shelf in the middle of the chamber closely around the thermocouples. Photos of the environmental chamber and the experiment setup are shown in Appendix D.

Thermal cycling tests are time consuming and very expensive so the cycling temperature profiles need to be carefully designed in order to achieve the most efficient lifetime data within limited time and make the most use of the existing experimental data for more comparisons.

The existing experimental data were from four passive thermal cycling ranges, namely -40°C to 190°C, -60°C to 170°C, -35°C to 145°C and -55°C to 125°C with a constant ramp rate of 11°C per minute during heating and 6°C per minute during cooling. The temperature profiles of these and the corresponding degradation rate by means of shear force measurement under the four temperature loads were presented in Table 5.2.

Basically, the proposed model is intended to predict the wear-out rate of the bond samples under any temperature loads provided that the temperature profile is known. From this point of view, the degradation data from all sorts of temperature ranges can be used for model validation. Therefore the temperature design is focused mainly on the investigation of the factors that influence the degree of the damage removal effect including (i) maximum temperature which determines the probability for diffusion to occur; (ii) the minimum temperature which has impact on the amount of build-up damage in the wire material and the existing damage has influence on the rate of the recrystallization (iii) the time spent at high temperature regimes which determines the degree of the microstructure restoration.

Accordingly, three groups of temperature profiles are designed.

7.3.2.1 Variation of maximum temperatures

Table 7.1: Temperature profiles designed to investigate the effect of T_{max}

No.	T_{min}	T_{max}	ΔT
A	-55°C	60°C	115°C
B	-55°C	90°C	145°C
C	-55°C	200°C	255°C

For an active diffusion to occur, the temperature should be high enough to overcome energy barriers. In proposed model, it is assumed that the

equilibrium temperature for aluminum wire is 90°C, which means that annealing phenomena become significant only when T_{max} is at least above this temperature. For comparability, maximum peak temperature is varied whilst keeping the same minimum temperature extreme. The bond shear force degradation rate obtained from these three tests can be compared to the existing data under -55°C ~ 125°C. Furthermore -55°C ~ 200°C is an extreme loading condition with very high T_{max} and extremely large temperature amplitude (ΔT). The experiment output can further elucidate the effects of high T_{max} and larger ΔT on the bond wear-out rate. It is expected to provide a strong evidence to prove that relating lifetime of wire bond interconnects solely to damage accumulation is inadequate and the influence of thermally activated processes must be taken into account.

7.3.2.2 Variation of minimum temperatures

Table 7.2: Temperature profiles designed to investigate the effect of T_{min}

No.	T_{min}	T_{max}	ΔT
D	10°C	125°C	115°C
E	-20°C	125°C	145°C

Strain hardening is caused by plastic deformation at temperatures low enough that atoms cannot arrange themselves. The extent of plastic deformation (damage) is affected by the minimum temperature to which the bonds are subjected. On the other side, the process of grain recovery and recrystallization is thermal dynamic. The rate and degree of the damage removal also depends on the amount of damage that already exists in the material.

Therefore the effect of T_{min} and thus the existing accumulated damage on the bond shear force degradation rate can be studied by the corresponding experimental results out of the above temperature loads as well as the existing

data under -55°C ~ 125°C. In addition, temperature profile D has the same ΔT as A and E has the same ΔT as B, but with different medium temperatures. These comparisons can provide information about the influence of temperature amplitude and medium temperature on the wear-out behavior.

7.3.2.3 Variation of time at temperatures

Table 7.3: Temperature profiles designed to introduce temperature-time effects

No.	T_{min}	T_{max}	ΔT	Dwelling time at T_{max}
F	-55°C	145°C	200°C	No dwell
G	-55°C	145°C	200°C	10 minutes
H	-55°C	145°C	200°C	20 minutes

Cycle based lifetime prediction models do not take into account of the time effect on the degradation rate and only the amplitude of the loading temperature play a part. They would result in the same lifetime prediction for these temperature loads as they have the same temperature amplitude and extremes.

One major advantage the proposed time-domain model has over cycle based lifetime models is that it is able to reflect the temperature-time effect on the wire bond degradation rate. In order to validate the model from this point of view, it is important to include temperature-time effect in the loading profiles, which can be achieved by including dwell times at maximum peak temperature or setting up different heating/cooling ramp rate between the same temperature extremes.

From the simulation results presented in Chapter 6, it is known that thermally activated processes start to make significant influence on the bond degradation only when T_{max} is above 125°C. So the temperature range of -55°C to 145°C is selected. The bond shear force degradation rate under load F can also be

compared to the shear data out of -35°C to 145°C. Since the ramp rate is more difficult to control for an environment chamber, temperature-time effects are presented by including dwell times at maximum peak temperatures. Ten minutes and twenty minutes of dwell times are included at 145°C.

The experiment results out of these tests can further elucidate the time-temperature effect on the bond wear-out behavior and prove the limitations of the cycle based lifetime prediction models.

7.3.3 Experiment results

So far, three temperature cycling tests have been performed due to the time being and availability of the equipment. In the following paragraphs, the experiment results are presented and discussed.

(1) -55°C ~ 60°C

Passive thermal cycling test under this temperature load was carried out in the University of Nottingham by using Eurotherm Environmental Chamber which allows maximum and minimum temperatures at 400°C and -70°C respectively. Temperature cycles were programmed via Eurotherm itools software. One thermocouple was connected to the substrate to monitor the chip temperature and the other one was exposed to the air inside the chamber.

An example of a programmed thermal cycling profile plotted alongside a profile recorded from a thermocouple (attached to a substrate tile) are presented in Figure 7.7; these show that one cycle takes 1800 seconds and the specimens experienced a constant ramp rate of 7°C per minute during heating and 7°C per minute during cooling.

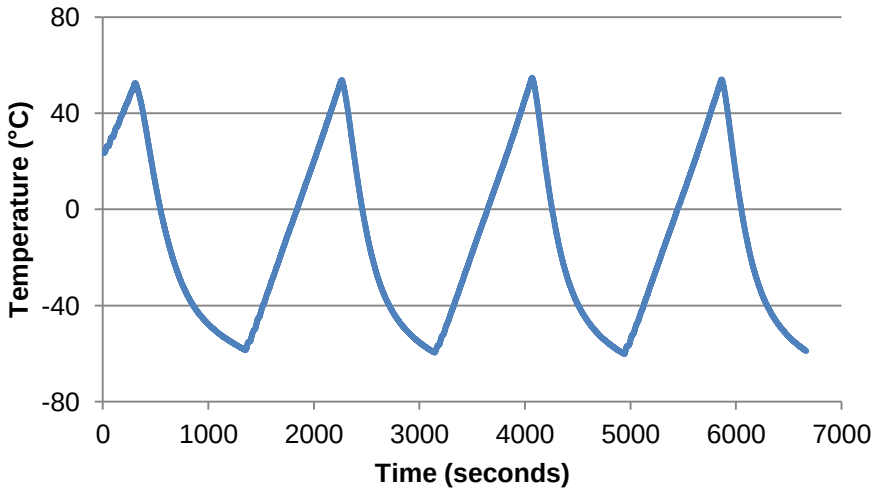

Figure 7.7: Experimental passive thermal profile for -55°C to 60°C

Four half-substrates were put in the chamber at the start of cycling. One sample was taken out at 600, 1000, 1500 and 2000 cycles respectively. Sixteen bonds were undertaken shear test for each specific number of cycles.

In Figure 7.8, shear test measurements for the first bonds and stitch bonds are presented which show the change in average shear force with increasing number of cycles, along with linear least means squares fits. Standard deviation error bars are also shown to represent the overall distribution of the group of shear force data points for one specific number of cycles. Dispersion of the values of shear force measurement might be due to the different wear-out rate of each bond or human factors in process of manual operation on shear testing.

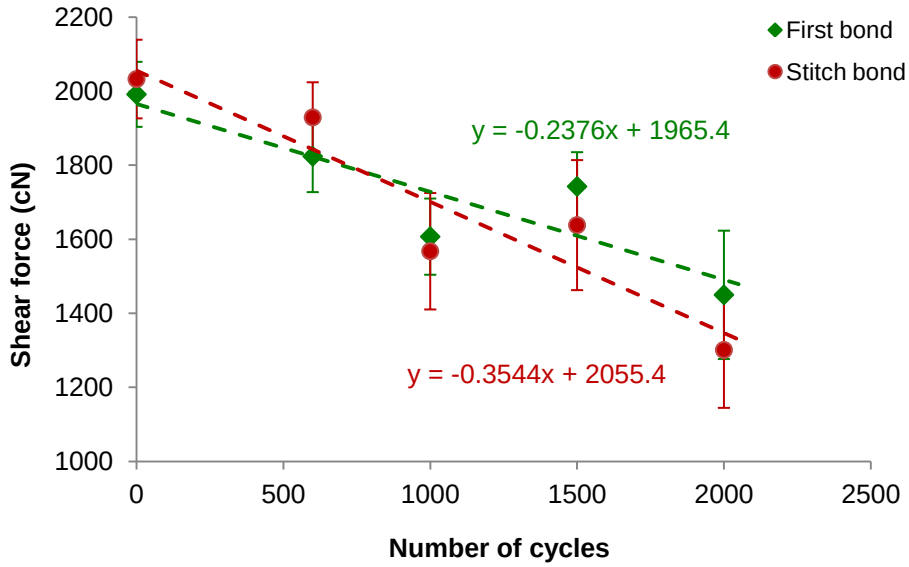

Figure 7.8: Rate of shear force degradation of pure Al wire bond subjected to passive thermal cycling in the range -55°C to 60°C

It can be seen that stitch bonds appear to wear out faster than first bonds. This may be due to the fact that stitch bonds tend to contain two as-bonded cracks which occur during loop formation, whereas first bonds often contain only one pre-exposure crack.

(2) 10°C ~ 125°C

Passive thermal cycling test under this temperature load was carried out using the same environmental chamber. The experimental temperature profile recorded from a thermocouple (attached to a substrate tile) is presented in Figure 7.9; these show that one cycle takes 1440 seconds and the specimens experienced a constant ramp rate of 7°C per minute during heating and 21°C per minute during cooling.

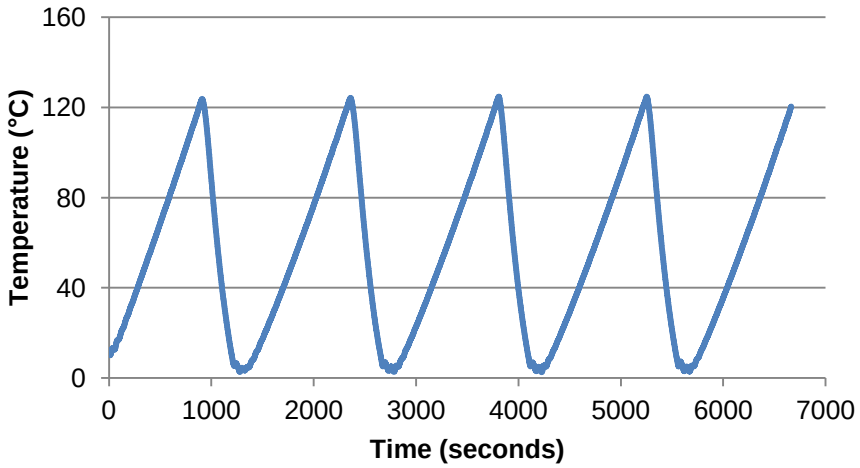

Figure 7.9: Experimental passive thermal profile for 10°C to 125°C

Three half-substrates with twenty wire bonds were put in the chamber at the start of cycling. One of the samples was taken out at 780, 1500 and 2500 cycles respectively. Sixteen bonds were undertaken shear test for each specific number of cycles. In Figure 7.10, mean values of sixteen bond shear force data and standard deviation error bars are plotted against number of cycles along with linear least means square fits.

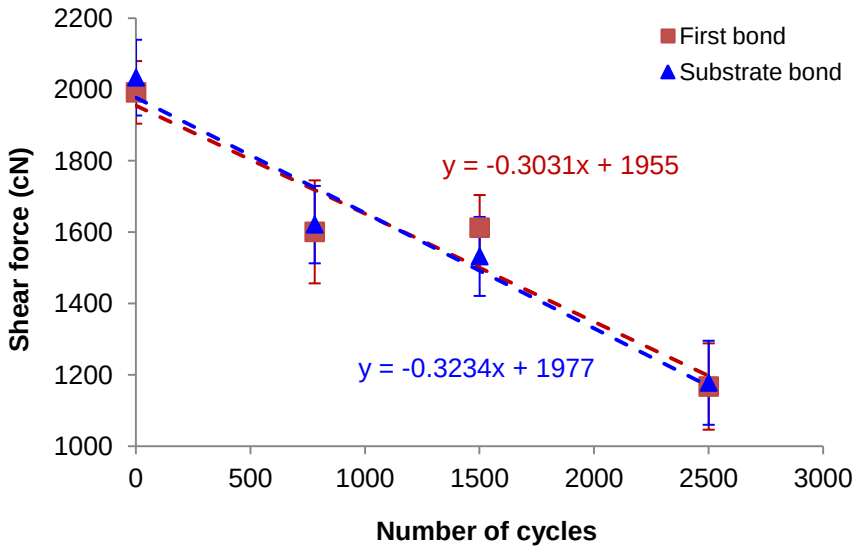

Figure 7.10: Rate of shear force degradation of pure Al wire bond subjected to passive thermal cycling in the range 10°C to 125°C

(3) -60°C ~ 200°C

Dynex Semiconductor Ltd., in Lincoln, U.K., kindly offered to perform a rapid cyclic temperature shock test ranging from -60°C to 200°C.

The tests were carried out in Vötsch thermal shock test chamber that is integrated of three temperature chambers in a vertical arrangement providing hot zone, middle zone and cold zone respectively. The temperature of the middle zone was set to the medium value of the two peak temperatures, i.e. 60°C. The tested samples are transferred between hot zone and cold zone through middle zone. The transfer time between hot and cold test zone was set to 2 minutes and the soak times in both zones are set to 10 minutes.

However, after 500 cycles, obvious substrate delaminating is observed (see Figure 7.11).

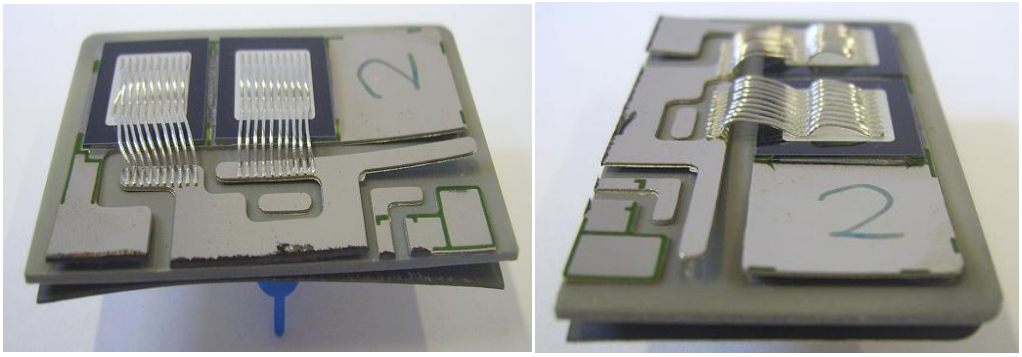

Figure 7.11: Substrate delaminating after 500 cycles during thermal shock test ranging from -60°C to 200°C

In the thermal shock test, the rates of heating up and cooling down are extremely faster than the rates in passive thermal cycling. The tested bond samples are based on the DBC aluminum nitride (AlN) ceramic substrates which have relatively low fracture toughness. Copper layer and the AlN ceramic tile expand and contract much more rapid than they do under thermal cycling conditions. Consequently, thermo mechanical strain induced by this

CTE mismatch generates more stress between the two layers. Therefore under this temperature range (-60°C to 200°C) in the thermal shock condition, substrate delaminating has been the primary failure mode. The measurement of bond shear force is not reliable anymore and cannot be used in the characterization of the bond wear-out behavior.

7.3.4 Discussion

In Figure 7.12, the rates of reduction in average shear force are compared for wires subjected to three thermal cycling regimes, namely -55°C ~60 °C, 10°C ~ 125°C and -55°C ~125°C.

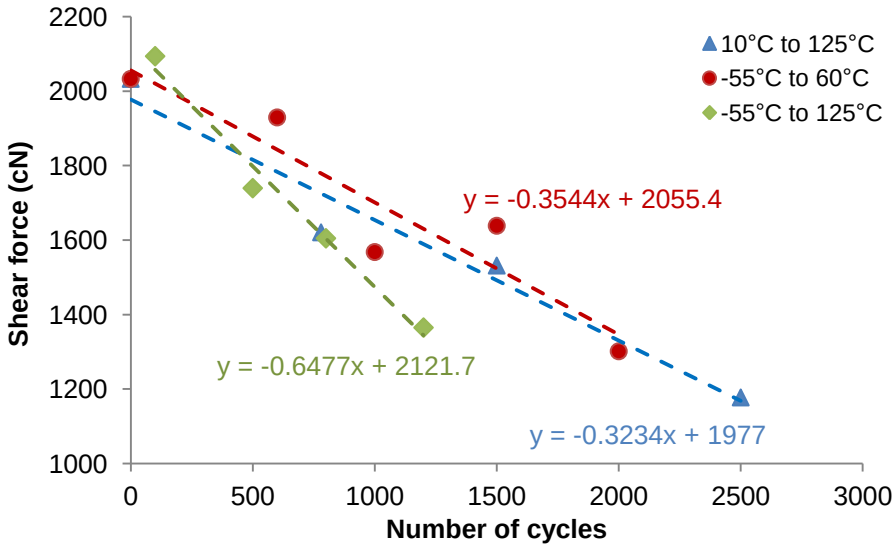

Figure 7.12: The rate of shear force degradation under three temperature regimes

Shear force degradation rates are calculated from the slope of the trend line and are listed in Table 7.4. It can be seen that the bonds exposed to load (a) and (b) exhibits similar wear-out rate. The shear force degradation rate under load (c) is faster than the rate under both load (a) and (b).

Table 7.4: Experimental results of shear force degradation rate under thermal cycling tests

Temperature profile				Shear force degradation rate
No.	Tmax (°C)	Tmin (°C)	ΔT (°C)	β
(a)	-55	60	115	-1.72×10^{-4}
(b)	10	125	115	-1.64×10^{-4}
(c)	-55	125	180	-3.05×10^{-4}

For these three thermal cycles, maximum temperature is not very high and there are no dwelling times at maximum temperatures. The extent of annealing will not be sufficient to generate significant damage removal effect. Under this condition, fatigue generated by temperature difference plays a main role during thermal exposure. This agrees with the simulation results in Chapter 6. In the section 6.3, simulation of the damage evolution during thermal cycling with T_{max} above 125°C showed extensive fluctuation and narrow fluctuation for the cycling with T_{max} below 125°C. Lifetime prediction (Figure 6.13) also showed that only when T_{max} is above 125°C, the effect of thermally activated processes on the lifetime starts to become significant.

Furthermore, load (a) and (b) has the different medium temperature but the bonds subjected to these two loads exhibits the similar wear-out rate. This would indicate that shear force degradation rate was mostly dependent on the amplitude of the temperature cycling and the effect arising from different medium temperatures is not significant.

7.3.5 Model validation

The calibrated time-domain damage based crack propagation model is operated in MATLAB with the corresponding three experimental temperature profiles as the input. The shear force degradation rates are evaluated accordingly and the results are presented in Table 7.5.

Table 7.5: Comparison of bond shear force degradation rate between experimental data and simulation results

		(a)	(b)	(c)
Temperature profile	T_{max}	-55°C	10°C	-55°C
	T_{min}	60°C	125°C	125°C
	ΔT	115°C	115°C	180°C
	Cycling time (seconds)	1800	1440	2800
	Heating rate (°C/minute)	7	7	11
	Cooling rate (°C/minute)	8	18	6
Wear-out rate	Predicted results	2.12×10^{-4}	1.39×10^{-4}	3.71×10^{-4}
	Experimental data	1.72×10^{-4}	1.64×10^{-4}	3.05×10^{-4}

Comparisons of shear force degradation rate show a good agreement between predicted results and experimental data. So far the proposed time-domain damage based crack propagation model has made correct predictions on the bond wear-out rate for six different temperature ranges under passive thermal cycling conditions.

7.4 MODEL VALIDATION USING ACTIVE POWER CYCLING RESULTS

7.4.1 Overview

The primary failure mechanisms in a wire bonded power semiconductor module that is subjected to active power cycling are bond wire lift-off and solder joint fatigue failure. Wire bond lifting is regarded as the dominant failure mechanism because it usually occurs before the thermal fatigue of solder joints [48, 94, 117]. And the observed lift-off during the tests is mostly the result of crack propagation along the bonding interface. The micrograph in Figure 7.13 shows a crack growing through the bond subjected to power cycling.

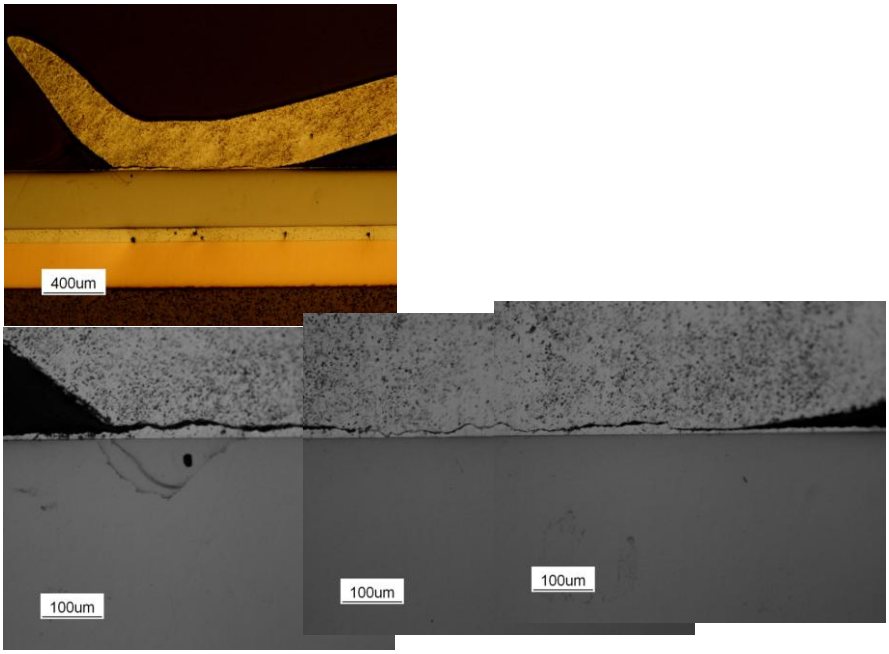

Figure 7.13: Crack propagation through a stitch bond after power cycling

A percentage of increase in the forward voltage is often used as the indicator of bond lift-off. Figure 7.14 and 7.15 shows an experimental example of the relationship between the forward voltage across the IGBT devices and the degradation of mean shear strength of a group of bonds. The tested devices were subjected to passive thermal cycling under temperature range from -55°C to 125°C. At regular number of cycles, one of the devices that were undertaking thermal cycling was taken out of the environmental chamber and the forward voltage was measured with 200A forward current. The voltage values are demonstrated in Figure 7.15. Then the bond shear force was measured; the values are shown in Figure 7.14 corresponding to the number of cycles. It can be seen that a 20% increase in device forward voltage occurs after 2900 cycles. However 50% of initial shear strength is reached after less than 1000 cycles and wires start to lift at 1500 cycles. From the two figures, it can be deduced that after 2900 cycles when V_f increases by 20%, majority of the wires have lifted off.

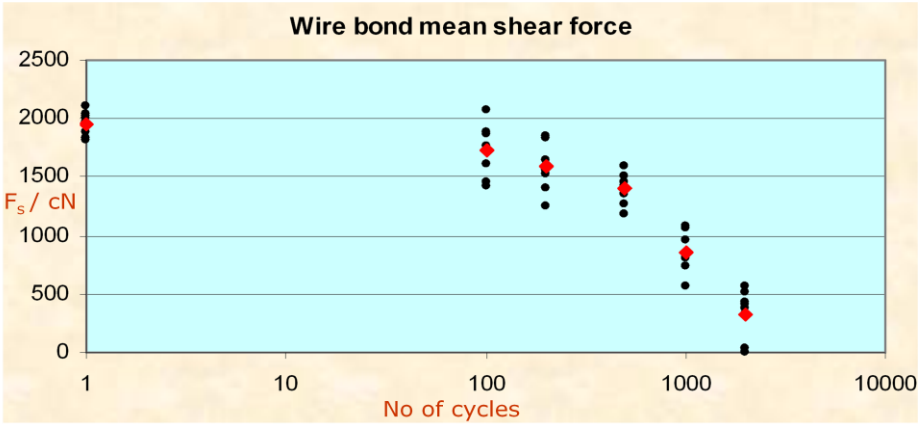

Figure 7.14: Wire bond mean shear force during thermal cycling tests under -55°C~125°C

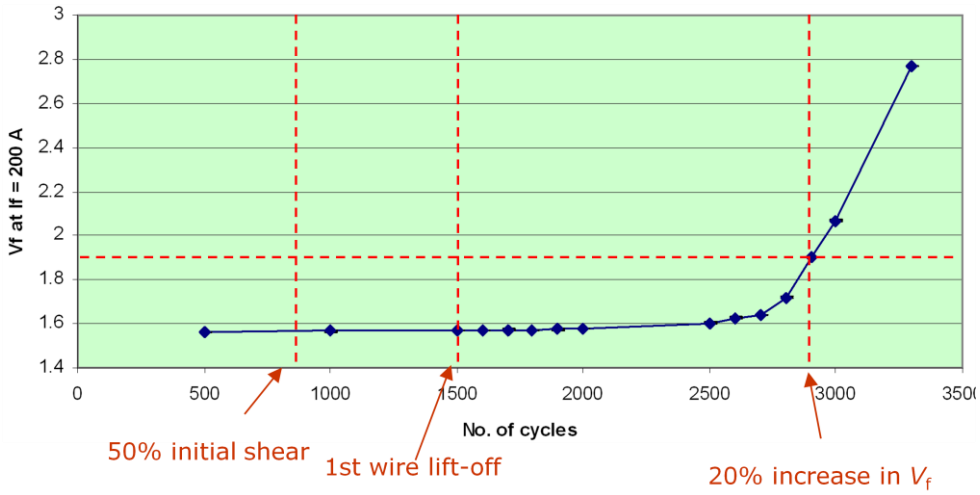

Figure 7.15: Increase in forward voltage corresponding to the drop of shear strength

In accelerated active power cycling tests, the failure of each bond in the tested device is indicated by a step wise increase of the forward voltage (V_f) across the device. In contrast with passive thermal cycling test where there is no acceleration of wire lift and bonds wear out at a relatively steady rate, power cycling accelerates wire lift because current flows through less number of wires as the consequence of bond lift-off and this aggravates stress on remaining wires leading to a steep increase in the gradient of the forward voltage across the tested devices. Therefore this segment in a plot of forward voltage against time from a real power cycling test, the slope is steeper than the one shown in Figure 7.15.

The number of cycles to failure (N_f) is usually defined by this steep increase in the forward voltage which will only occur when the majority of wire bonds have lifted off, as illustrated in Figure 7.16 (a) and the test terminates at this point. Indeed this might correspond to all of the wires having lifted.

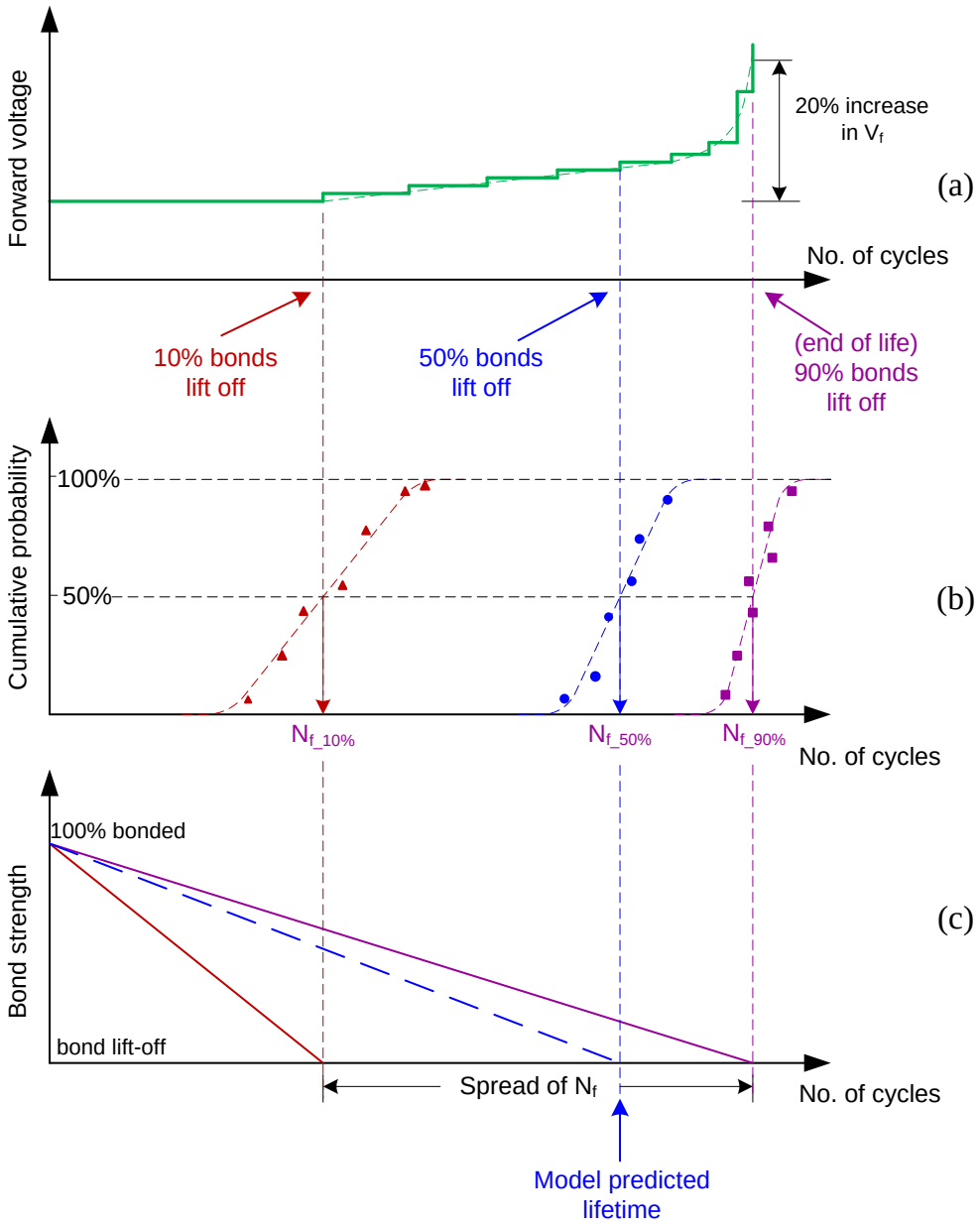

Figure 7.16: Schematic plots of (a) increase of the forward voltage during power cycling (b) statistic analysis on groups of N_f data points (c) a spread of N_f corresponding to different proportion of wire lift-off

However, the evaluation on N_f made by this single failure criterion is incomplete. Comparing the power cycling results for N_f with those obtained from the model or from shear test data thus needs some care since the model and shear test data will predict the average bond wire life. It is, therefore, necessary to obtain a measure of the spread of lifetime, as shown in Figure 7.16 (b) which schematically plots the cumulative probability for each data point of N_f with regard to a specified proportion of wire lift-off ranging from 10% (N_{f_10}) to 90% (N_{f_90}). In some cases this can be estimated from the power cycling data by observing the steps in forward voltage and relating these to individual wire lifts. The 10%, 50% and 90% values (for example) can then be determined for a large number of power cycling samples to build up the statistical picture shown in Figure 7.16 (b). A comparative rate for wire lifting can then be estimated from the mean value of the 50% (N_{f_50}) as illustrated in Figure 7.16 (c).

7.4.2 Experiment setup

Power cycling test rig is composed of eight channels. Each channel mainly contains four tested power diodes connected in series and the corresponding bypass circuit made up of two parallel MOSFETs. An infrared temperature sensor ranging from -40°C to 400°C is mounted on the top of each device to measure the junction temperature of the power diode. The real-time temperature values are sampled by DSP and converted into scaled voltage. Gate signals for MOSFETs are generated by a FPGA card to activate and deactivate bypass circuit. Each power diode is made by soldering a diode die on a DBC substrate tile (AlN ceramic) which in turn is connected with the top terminal of the die through ten ultrasonically bonded pure aluminium wires (99.999%), 375μm in diameter. The tested power diodes were provided by Dynex Semiconductors Ltd. Four power diode devices are mounted on a water cooling heat sink.

50A constant current passes through the four tested diodes. Once the upper temperature limit of any one diode is reached, bypass MOSFETs are activated and the load current is diverted by the corresponding bypass circuit. Then the temperature of this diode starts to decrease. When the lower temperature limit is reached, the by-pass device is switched off and current goes through the device again. This process is repeated until the tested power diodes fail. The schematic diagram in Figure 7.17 demonstrates the design for the one channel of the power cycling test rig. Eight channels are to be built.

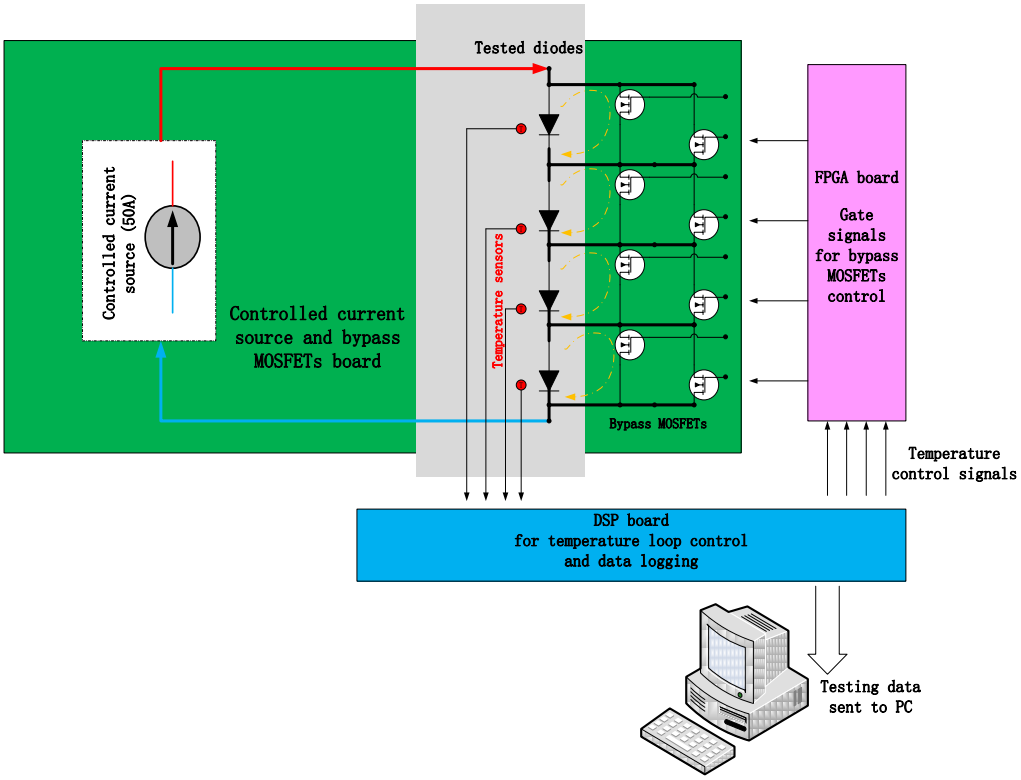

Figure 7.17: Design of the power cycling test rig

The forward voltage V_f crossing the diodes are continuously monitored. The normal value of V_f is between 2 ~ 2.1V and the increase of V_f to 2.5V is defined as failure limits.

7.4.3 Experiment results

The power diode samples were provided by Dynex Ltd. with standard loop height and bond parameters. So far three samples were operated to failure under the temperature ranging from 40°C to 120°C. The cycling time was approximately 6 seconds for all three samples. Figure 7.18 is showing a real-time temperature profile loaded on one of the diodes.

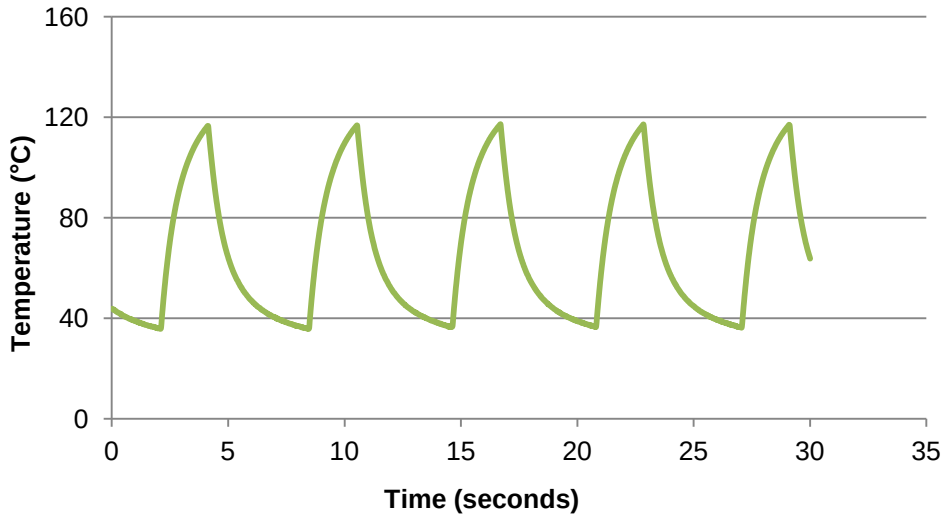

Figure 7.18: An experimental power cycling temperature profile

Raw V_f data from the accelerated power cycling life tests are depicted below in two graphs. Figure 7.19 shows the overall view of the V_f from the start to the end of the test. It can be seen that after approximately 120000 cycles, V_f starts to increase at a relatively flat gradient and a steep increase follows. Shortly after this significant increase, when V_f nearly reaches 2.5V, the device is regarded as failure and the test terminates. This number of cycles to failure corresponds to N_{f_90}. They are 145140, 151580 and 179380 cycles respectively for the three tested devices.

The segment of V_f curves from the V_f starting to change to the end of life is enlarged and shown in Figure 7.20. Number of cycles to 50% bond lifting (N_{f_50}) is estimated by counting the fourth step of increase in V_f since there are 8 wires bonded on each diode die. The approximate numbers for the three devices are listed in Table 7.6.

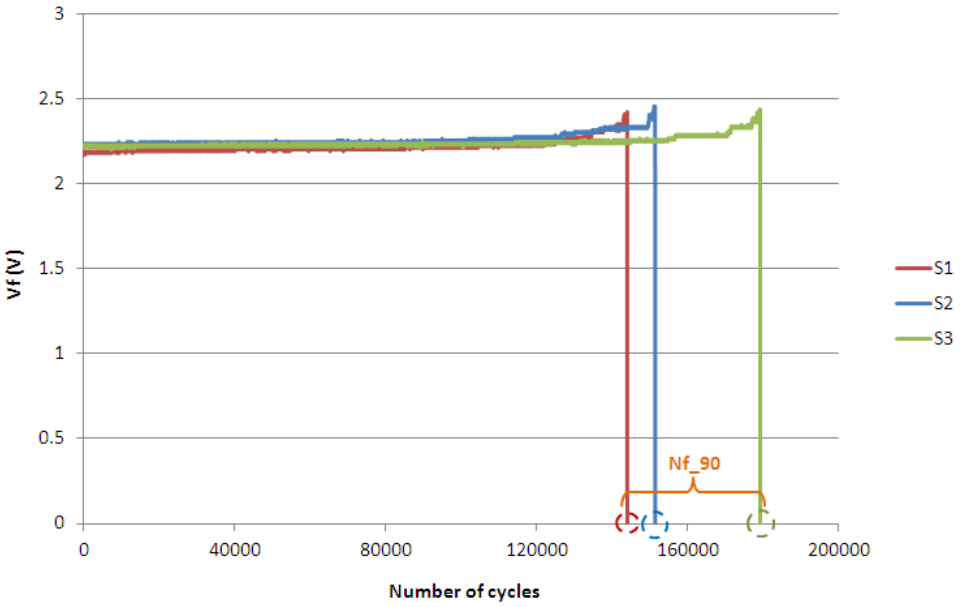

Figure 7.19: Measurement of V_f across three power diodes during power cycling

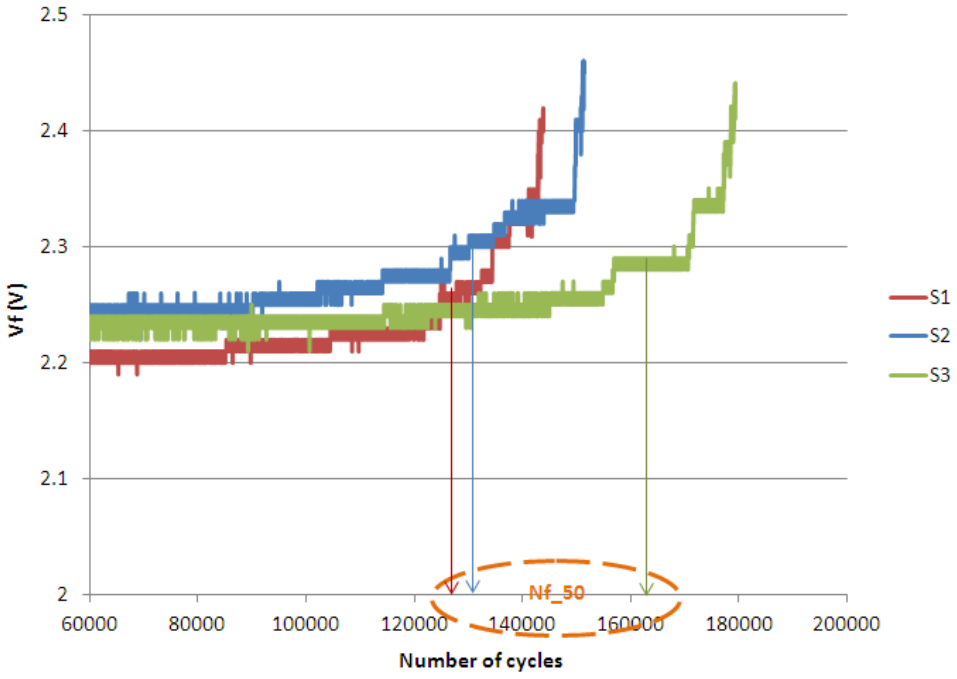

Figure 7.20: Enlarged segment of V_f after significant change starts

Table 7.6: Experimental lifetime data and loading condition in power cycling tests

Temperature range	40°C ~120°C			
Cycling time	6 seconds			
Sample	S1	S2	S3	Mean value
N_{f_90}	145,140	151,580	179,380	158,700
N_{f_50} (approximate)	128,000	132,000	163,000	141,000

7.4.4 Model prediction

Then the calibrated damage-based crack propagation model was performed under the temperature range of 40°C ~ 120°C with the cycling time of 6 seconds. The wear-out rate of the bond strength was estimated as 6×10^{-6} per cycle; the lifetime predicted by the model is 166,670 cycles.

Model predicts the mean lifetime which corresponds to 50% of wire lifting. However from the predicted result it can be seen that the model seems to have overestimated the lifetime despite that the power of the magnitude is in the same order as the experimental data.

Obviously, three experimental data points are very limited amount for model validation. A proper statistic analysis can only be performed by ample lifetime data under various loading conditions to provide more confident information.

7.5 Summary

The accelerated tests are widely used in electronic community to perform design validation and reliability assessment. Passive thermal cycling tests and active power cycling tests are the most frequently adopted methods. For the purpose of validation of the onward development of the time-domain models and further characterization on the bond wear-out behavior under various temperature loads, both thermal cycling and power cycling are carried out to capture wire bond degradation information and lifetime data. The intention and design of the experiments are presented in this chapter. Due to the time being, only two thermal cycling temperature profiles have been performed. The experimental results of bond shear force degradation rate under these two loads are illustrated. Bond shear force degradation rates have been predicted by the damage based model corresponding to the temperature loads simulated for both thermal cycling and power cycling conditions. Agreement of the comparisons between experimental data and simulation results has provided good validations on the model.

Meanwhile three lifetime data points of the power diodes undertaken power cycling are obtained. Discussion has been launched on the distinction between the number of cycles to failure indicated by V_f and that is predicted by lifetime models thus the need of a spread of lifetime under accelerated power cycling tests is highlighted.

CHAPTER 8

CONCLUSIONS AND FUTURE WORK

8.1 CONCLUSIONS

The principle aim of the work presented in this thesis has been to propose, calibrate and validate a novel physics-of-failure model for the lifetime prediction of wire bond interconnects in a time domain representation.

Existing lifetime models are usually developed under the assumption that the bond wire is subjected to regular cyclic loading. Lifetime is generally accounted for by the loading amplitude alone, although this is represented in various forms. They share the common view that wire bond failure is the outcome solely of damage accumulation during repeated heating and cooling which lead to a common result that the number of cycles to failure decreases as the loading temperature range increases.

In reality, however, power modules are usually subjected to irregular time varying loads, either as a consequence of environmental changes or load cycling. Although the Rainflow counting method can be used to convert irregular time series into a sequence of cycles, this counting algorithm uses just the extreme points of the loads.

Furthermore, some unusual experimental observations have shown that when maximum peak temperature is high enough, the consequent diffusion-driven mechanisms such as annealing and creep have significant effect on the wear-

our behaviour of the wire bonds. These thermally activated processes are believed to be able to remove some of the build-up damage in the wire material. For these high-temperature related phenomena, the time spent on the processes is a crucial factor. It determines the extension of dynamic recovery of the strained material. However in the commonly adopted cycle-based modelling methods, neither damage removal processes nor time-at-temperature effect is taken into account or appropriately represented, leading to erroneous and indeed risky predictions.

These considerations have motivated the intention to develop a lifetime prediction modelling methodology in time-domain representation. A damage-based crack propagation model is at the very core of the overall modelling perception by which the damage condition in wire materials along the bonding interface is estimated at regular time intervals as the result of the balance between damage accumulation and damage removal described by two terms respectively.

Damage in the wire material is driven by displacement strain induced by mismatched CTE between wire and semiconductor device material. The damage accumulation term consists of a strain distribution function and strain-driven constitutive functions. Damage distribution at the bonding interface is determined by a spatial plastic strain weighting function which also defines the geometry of the bond foot. Other underlying factors which influence the build-up of damage and vary for different materials are taken into account implicitly by the incorporation of a work hardening term and temperature hardening term as well as a displacement strain expression.

Damage removal is represented by an annealing term accounting for the effect of material dependent thermally activated processes. The amount of annihilated damage is determined by the existing damage and exposure time. Thus the impact of time at temperature and other rate sensitive processes on the bond degradation rate can be accurately represented.

The accumulated damage leads to the growth of the cracks and hence the decrease of bond strength. Therefore bond shear force is estimated via crack

length which in turn is estimated as a function of total damage and the rate of change of damage. In this way the damage parameter is related to a measurable indicator of the bond degradation.

Uniaxial tensile tests were performed for pure aluminium bonding wires under various conditions and strain energy has been derived from the corresponding stress-strain curves. As one of the essential steps for model development, the form of the constituent functions has been adjusted through quantitatively linking damage parameter to plastic strain energy density. Then all the model parameters were justified by the experimental data of shear force degradation rate resulting from accelerated thermal cycling tests under four temperature ranges.

The last part of the thesis concerns the design of the accelerated tests for the purpose of the model validation. A full list of desired temperature profiles for the operation of passive thermal cycling tests have been provided with the detailed explanation on the reasons and aims. For the time being and due to the availability of the equipment, only two of them have been completed. The corresponding bond strength degradation rate was obtained by means of shear testing. The experimental results were presented and discussed. In the mean time, simulation of the development of bond shear force was performed by the calibrated damage based crack propagation model. Agreement between experimental data and predicted results has validated the model. In addition, the active power cycling tests were performed on power diodes which produced three lifetime data points. Failure was indicated by 20% increase in forward voltage (V_f) across the device. Discussion has been launched on the distinction between the number of cycles to failure indicated by V_f and that is predicted by lifetime models thus the need of a spread of lifetime under accelerated power cycling tests is highlighted.

At this stage, it can be summarized that the new time-domain model for the lifetime prediction of wire bond interconnects is believed to be able to overcome the limitations of the existing cycle-dependent models. It not only includes the high-temperature related damage removal processes and also can more accurately reflect the temperature-time effects on the wear-out behaviour.

8.2 FUTURE WORK

Response of the wire material to various loading conditions needs to be further investigated so that all the model parameters can be properly related to physically quantifiable properties such as work hardening and creep behaviour.

It is also necessary to more accurately justify each term that constitute the model so that it is able to represent both fundamental material constitutive characteristics and degradation behaviour under accelerate thermal cycling test conditions.

In the presented work, the model parameter ‘damage’ is quantitatively linked to experimentally derived parameter strain energy. In the damage based crack propagation model, crack growth rate is defined as a function of total damage and the rate of change of damage. Reasonably, a link between crack length and strain energy, which are both measurable physical quantities, is expected to be made. Therefore the function describing the relation of crack growth rate and strain energy needs to be determined by means of experimental work.

One major advantage the proposed model has over cycle-based models is that it is able to more accurately reflect the temperature-time effects. Accelerated passive thermal cycling tests including time effect in the temperature profiles need to be stressed. Comparisons between prediction made simulation and experimental results of the bond degradation rate can further investigate the performance of the model.

Model validation can only be achieved through large amount of lifetime data by accelerated tests. More tests are required for collecting the lifetime data as well as to further characterize the time-at-temperature effect and the influence of the high maximum temperature on the wear-out behaviour of the wire bonds during temperature fluctuation. Statistic analysis on the existing shear force data from the thermal cycling tests need to be performed and a spread of lifetime data out of power cycling tests is necessary in order to provide more comprehensive information.

At last, so far the model parameters are justified as for pure aluminium bond wire and silicon device. It is preferable to check the model performance for different materials which needs more experimental work. Furthermore, at this stage the model is developed for wire bond interconnects, but the methodology is meant to extend to other crack propagating interface.

REFERENCES

[1] J. D. Van Wyk, H. C. Skudelny, and A. Muller-Hellmann, "Power electronics, control of the electromechanical energy conversion process and some applications," IEE Proceedings B. Electric Power Applications, vol. 133, pp. 369- 99, 1986.

[2] C. T. Leonard and M. G. Pecht, "Improved techniques for cost effective electronics," in Proc. Reliability Maintainability Symp., Jan. 29–31, 1991, pp. 174–182.

[3] C. C. Chan, K. T. Chau, "An Overview of Power Electronics in Electric Vehicles" , IEEE Transactions on Industrial Electronics, vol.44, no.1, Feb. 1997, pp.3-13.

[4] A. F. Zobaa and B. K. Bose, "Renewable Energy, Global Warming Problem and Impact of Power Electronics (Invited Paper)", ICPEPQ'11, Spain, April 13th to 15th, 2011

[5] M. Ohring, "Reliability and failure of electronic materials and devices", Academic Press, USA, 1998, ISBN 0-12-524985-3

[6] B. Foucher, J. Boulli, B. Meslet, D. Das, "A review of reliability prediction methods for electronic devices", Microelectronics Reliability 2002; 42(8): 1155–1162

[7] "Guidelines to Understanding Reliability Prediction", *http://www.epsma.org/pdf/MTBF_Report_24_June_2005.pdf*

[8] IEEE Guide for Selecting and Using Reliability Predictions Based on IEEE 1413™", IEEE Standards Coordinating Committee 37 on Reliability Prediction, IEEE, New York, 19th February, 2003

[9] M. Pecht and A. Dasgupta, "Physics-of-Failure: An Approach to Reliable Product Development", Journal of the Institute of Environmental Sciences, September/October 1995, Vol. 38, pp. 30-34

[10] A. Dasgupta, and M. Pecht, "Material failure mechanisms and damage models," *IEEE Transactions on Reliability*, Vol. 40, Issue 5, December 1991, pp: 531-536

[11] M. Pecht, B. Tuchband, N. Vichare, and Q. J. Ying, 'Prognostics and Health Monitoring of Electronics', International Conference on Thermal, Mechanical and Multi-Physics Simulation Experiments in Microelectronics and Micro-Systems 2007, EuroSime 2007, pp.1-8

[12] M. Musallam, C. M. Johnson, C. Y. Yin, H. Lu, C. Bailey, , "Real-Time Life Expectancy Estimation in Power Modules", Proc of the 2nd Electronics System-Integration Technology Conf; London, UK, September 2008, pp. 231-236

[13] A.T. Bryant, P. A. Mawby, P. R. Palmer, E. Santi, J. L. Hudgins, "Exploration of Power Device Reliability Using Compact Device Models and Fast Electrothermal Simulation", IEEE Transactions on Industry Applications, 2008, vol. 44, No. 3, pp.894-903

[14] T. Matsunaga, Y. Uegai, "Thermal Fatigue Life Evaluation of Aluminium Wire Bonds", IEEE, 2006 Electronics System Integration Technology Conference, Dresden, Germany, pp.726-732

[15] P. A. Agyakwa, W. S. Loh, M. R. Corfield, E. Liotti, S. C. Hogg, C. M. Johnson, "Anomalous Reliability Behaviour of 99.99% and 99.999% Pure Aluminium Wire Bonds under Thermal Cycling", IMAPS 2008,41st International Symposium on Microelectronics, Rhode Island, Providence, USA.

[16] Y. Yamada, Y. Takaku, Y. Yagi, I. Nakagawa, T. Atsumi, M. Shirai, I. Ohnuma, "Reliability of Wire-Bonding and Solder Joint for High Temperature Operation of Power Semiconductor Device", Microelectronics Reliability, 47(2007), pp.2147–2151

[17] P.A. Agyakwa, M.R. Corfield, L. Yang, J.F. Li, V.M.F. Marques, C. M. Johnson, "Microstructural evolution of ultrasonically bonded high purity Al wire during extended range thermal cycling", Microelectronics Reliability 51(2), 2011, pp.406-415

[18] B. Reinhold, "Advanced packaging yields higher performance and reliability in power electronics," *Microelectronics Reliability*, vol. 50, pp. 1715-1719.

[19] T. Yamada, G. Majumdar, S. Mori, H. Hagino, H. Kondoh, "Next Generation Power Module – An Evolutionary Change from "Discrete Semiconductor" to System Semiconductor", Proc. of the 6th International Symposium on Power Semiconductor Devices & IC's Davos, Switzerland, May 31-June 2, 1994, pp.3-8

[20] T. Stockmeier, "From Packaging to "Un"-Packaging - Trends in Power Semiconductor Modules ", Power Semiconductor Devices and IC's, 2008. ISPSD '08, 20th International Symposium on, 18-22 May 2008, pp.12-19

[21] C. M. Johnson, A. Castellazzi, R. Skuriat, P.Evans, J. F. Li and P. Agyakwa, "Integrated High Power Modules", CIPS 2012, March 6-8, 2012, Nuremberg, Germany

[22] L.M. Tolbert, B. Ozpineci, S. K. Islam, M. Chinthavali, "Wide Bandgap Semiconductors for Utility Applications," IASTED International Conference

on Power and Energy Systems (2003), February 24-26, 2003, Palm Springs, CA, pp. 317-321.

[23] V. Cimalla, J. Pezoldt, O. Ambacher. "Group III nitride and SiC based MEMS and NEMS: materials properties, technology and applications", Journal of Physics D: Applied Physics 40(2007), pp.6386–6434.

[24] J. L. Hudgins, G. S. Simin, E. Santi, M. A. Khan, "An Assessment of Wide Bandgap Semiconductors for Power Devices", IEEE Transactions on Power Electronics, Vol. 18, No. 3, May 2003, pp.907-914

[25] B. Ozpineci, L.M. Tolbert, "Comparison of Wide-bandgap Semiconductors for power electronics applications", Oak Ridge National Laboratory

[26] M. J. Palmer, R. W. Johnson, T. Autry, R. Aguirre, V. Lee, J. D. Scofield, "Silicon Carbide Power Modules for High-Temperature Applications", IEEE Transactions on Components, Packaging and Manufacturing Technology, Vol. 2, No. 2, February 2012

[27] R.J. Ikujeniya, "Microstructural Investigation of Ultrasonically Bonded Heavy Gauge Aluminium Wire", Master of Science Project Dissertation, IPTME, Loughborough University, 2007.

[28] J. Onuki, M. Suwa, Y. Koubuchi and O. Asai, "Development of Corrosion-Resistance Aluminium Alloy Wire", IEEE Transactions on Components, Hybrids and Manufacturing Technology, Vol. CHMT-8, No. 4, December 1985

[29] D. Siepe, R. Bayerer, R. Roth, "The Future of Wire Bonding Is? Wire Bonding!", CIPS 2010, March 16-18, Nuremberg/Germany

[30] L. Pryor, R. Schlobohm, B. Brownell, "A Comparison of Aluminium Vs. Copper as Used in Electrical Equipment", *http://www.geindustrial.com/Newsletter/Aluminum_vs_Copper.pdf*

[31] TUB, "Analysis of the Current Status of European Lead- Free Soldering 2004," Germany, Jan. 2005.

[32] A. Syed, "Accumulated Creep Strain and Energy Density Based Thermal Fatigue Life Prediction Models for SnAgCu Solder Joints", IEEE 2004 Electronic Components and Technology Conference, pp. 737~746

[33] R. Coyle et.al, "the Influence of the Pb-free Solder Alloy Composition and Processing Parameters on Thermal Fatigue Performance of a Ceramic Chip Resistor", IEEE 2009, Electronic Components and Technology Conference, pp.423-430

[34] H. L.Ning, J. S Ma, F. X. Huang, Y. G. Wang, Q. Q. Li, X. Y. Li, "Preoxidation of the Cu Layer in Direct Bonding Technology", Applied Surface Science 211 (2003), pp.250-258

[35] J. Schulz-Harder and K. Exel, “Recent Development of Direct Bonded Copper Substrates for Power Modules”, IEEE, Electronic Packaging Technology Proceedings, ICEPT 2003, October 2003, pp. 491-496

[36] X. R. Xu, et.al, “Direct Bonding Copper to Aluminum Nitride Substrate”, Journal of Inorganic Materials, 2003, 18(4), pp.837-842

[37] D. J. Sharar, N. R. Jankowski and B. Morgan, “Thermal Performance of Direct-Bond-Copper Aluminum Nitride Manifold-Microchannel Cooler”, 26th IEEE SEMI-THERM Symposium, 2010, pp.68-74

[38] F. D. Barlow III, “Electronic Packaging Strategies for High Current DC to DC Converters”, PhD thesis: Virginia Polytechnic Institute and State University, 1999

[39] N. Y. A. Shammas, "Present problems of power module packaging technology", Microelectronics Reliability, Vol. 43, Issue 4 (2003), pp. 519-527

[40] H. Ye, M. H. Lin, C. Basaran, “Failure Modes and FEM Analysis of Power Electronic Packaging”, Finite Elements in Analysis and Design 38 (2002), pp.601-612

[41] R. R. Tummala, “Fundamentals of Microsystems Packaging”, McGraw-Hill: New York, 2001

[42] G. Harman, “Wire Bonding in Microelectronics: Materials, Processes, Reliability and Yield”, McGraw-Hill: 1997

[43] D. Rooney, D. Nager, D. Geiger, and D. Shanguan, “Evaluation of wire bonding performance, process conditions, and metallurgical integrity of chip on board wire bonds,” Microelectronics and Reliability, vol. 45, Feb. 2005, pp. 379-390.

[44] H. Xu, C. Q. Liu, V.Siberschmidt and Z. Chen, “The Role of Bonding Duration in Wire Bond Formation: A Study of Footprints of Thermosonic Gold Wire on Aluminum Pad”, Microelectronics International, Vol. 27, No. 1, 2010, pp.11-16

[45] I. Lum, M. Mayer and Y. Zhou, “Footprint Study of Ultrasonic Wedge-Bonding with Aluminum Wire on Copper Substrate”, Journal of Electronic Materials, Vol. 35, No. 3, 2006, pp.433 to 442

[46] T. Komiyama, Y. Chonan, J. Onuki, M. Koizumi and T. Shigemura, “High-Temperature Thick Al Wire Bonding Technology for High-Power Modules”, Japan Society of Applied Physics, Vol. 41 (2002), pp.5030-5033

[47] S. Ramminger, P. Türkes, and G. Wachutka, "Crack Mechanism in Wire Bonding Joints", ESREF '98, Copenhagen, Denmark; in Microelectronics and Reliability, Vol. 38, No. 6-8, June-August 1998, pp.1301-1305

[48] M-H. Pooch, K. J. Dittmer, D. Gabisch, “Investigations on the damage mechanism of aluminium wire bonds used for high power applications”, Proceedings of the EUPAC 96; 1996. pp. 128–131.

[49] H. Lu, W.-S. Loh, C. Bailey, C. M. Johnson, “Computer Modelling Analysis of Globtop’s Effects on Aluminium Wirebond Reliability”, IEEE 2008, 2nd Electronics Systemintegration Technology Conference, Greenwich UK, pp. 1369-1373

[50] A. Hamidi, N. Beck, K. Thomas, E. Herr, “Reliability and Lifetime Evaluation of Different Wire Bonding Technologies for High Power IGBT Modules”, Microelectronics Reliability 39 (1999), pp. 1153-1158

[51] J. S. Hwang, R. M. Vargas, (1990) "Solder Joint Reliability—Can Solder Creep?", Soldering & Surface Mount Technology, Vol. 2, Issue 2, pp.38 – 45

[52] S. Wiese, E. Meusel, K.-J. Wolter, “Microstructural Dependence of Constitutive Properties of Eutectic SnAg and SnAgCu Solders”, IEEE 2003 Electronic Components and Technology Conference, pp.197-206

[53] R. R. Chomrik, D. N. Wang, A. Shugar, L. Limata, M. R. Notis, , R. P. Vinci, “Mechanical Properties of Intermetallic Compounds in the Au-Sn System”, Journal of Materials Researcj, Vol. 20, issue. 8, 2005, pp. 2161-2172

[54] J. H. Harris, E. Rubel, “The Role of Interfacial Compound Formation on Packaging Reliability”, Feature Article: Advancing Microelectronics (IMAPS), Vol. 35, No. 4, Jul/Aug 2008, pp. 20-27

[55] M. Günther, K. J. Wolter, M. Rittner, W. Nüthter, “Failure Mechanisms of Direct Copper Bonding Substrates”, Proceedings of Electronics System integration Technology Conference (ESTC), Dresden, Germany; 2006, pp.714–718

[56] Y. Yuichi, H. Ohtsu and T. Shibata, “Thermally Induced Failure of Copper-Bonded Alumina Substrates for Electronic Packaging”, Journal of the American Ceramic Society, Vol. 75, Issue 12, December 1992, pp. 3353-3357.

[57] S. Pietranico, S. Pommier, S. Lefebvre, Z. Khatir, S. Bontemps, “Characterisation of Power Module Ceramic Substrate for Reliability Aspects”, Microelectronics Reliability 49 (2009), pp.1260-1266

[58] M. G. Pecht and F. R. Nash, “Predicting the Reliability of Electronic Equipment”, Proceedings of the IEEE, Vol. 82, No. 7, July 1994, pp.992-1004

[59] IEEE Standard 1413-1998, “IEEE Standard Methodology for Reliability Prediction and Assessment for Electronic Systems and Equipment,” IEEE, December 1998.

[60] MIL-HDBK-217F - Military Handbook: Reliability Prediction of Electronic Equipment, December 02, 1991

[61] M. Pecht, “Why the Traditional Reliability Prediction Models Do Not Work - Is There an Alternative?”, Electronics Cooling, Vol. 2, pp. 10-12, January 1996

[62] J. A. Mclinn, “Constant failure rate—a paradigm in transition?” Quality and Reliability Engineering International, vol. 6, pp. 237–241, 1990

[63] T. Stadterman, M. Cushing, B. Hum, A. Malhotra, M. Pecht, “The Transition from Statistical- Field Failure Models to Physics of Failure based Models for Reliability Assessment of Electronic Packages”, Proceedings of the INTERpack’95, Lahina, Maui, HI, March 26-30, 1995, pp. 619-625.

[64] M. Pecht, A. Dasgupta, D. Barker, C. T. Leonard, “The reliability physics approach to failure prediction modelling,” Quality and Reliability Engineering International, Vol. 6, Issue 4, pp: 267-273, September/October 1990

[65] K. Chatterjee, M. Modarres and J. B. Bernstein, “Fifty Years of Physics of Failure”, Journal of the Reliability Information Analysis Center, January 2012

[66] K. Upadhyayula and A. Dasgupta, “Physics-of-Failure Guidelines for Accelerated Qualification of Electronic Systems”, Quality and Reliability Engineering International, Vol. 14, Issue 6, (1998), pp.433-447

[67] M. J. Cushing, D. E. Mortin, T. J. Stadterman, Anupam Malhotra, “Comparison of Electronics-Reliability Assessment Approaches”, IEEE Transactions on Reliability, Vol. 42, 1993 December, pp.542-546

[68] S. Yang, D. Xiang, A. Bryant, P. Mawby, L. Ran, and P. Tavner, "Condition Monitoring for Device Reliability in Power Electronic Converters: A Review," *Power Electronics, IEEE Transactions on*, Vol. 25, pp. 2734-2752.

[69] S. Mishra and M. Pecht, “*In-situ* sensors for product reliability monitoring”, in *Proc. SPIE*, vol. 4755, 2002, pp. 10–19.

[70] J. Evans, M. J. Cushing, P. Lall, R. Bauernschub, “A Physics-of Failure (POF) Approach to Address Device Reliability in Accelerated Testing of MCMS”, Proceedings of IEEE: Multi-Chip Module Conference, 1995

[71] C. Bailey, T. Tilford and H. Lu, "Reliability Analysis for Power Electronics Modules", Electronics Technology Conference, 30th ISSE 2007, IEEE, pp.12-17

[72] M. Pecht, A. Dasgupta and P. Lall, “A Failure Prediction Model for Wire Bonds”, Proc. of ISHM, October 17-19, 1989, Baltimore, MD, pp. 607-613

[73] L. F. Coffin, Jr., “A study of the effects of cyclic thermal stresses on a ductile metal”, Trans. ASME 76, pp.931-950, 1954

[74] S. S. Manson, “Behaviour of Materials under Conditions of Thermal Stress”, NACA Report, No. 1170, 1954

[75] H. L. L. Pang, T. L. Tan, J. F. Leonard, Y. S. Chen, “Reliability Assessment of A Wirebond Chip-on-Board Package Subjected to Accelerated Thermal Cycling Loading”, 1997 IEEE/CPMT Electronic Packaging Technology Conference, pp.93-97.

[76] N. V. Chidambaram, “A Numerical and Experimental Study of Temperature Cycle Wire Bond Failure”, 41st ECTE 1991, pp. 877-882

[77] K. N. Meyyappan, P. Hansen, “Wire Fatigue Model for Power Electronic Modules”, Proceedings of IMECE, Washington, D.C., November 15-21, 2003

[78] S. Ramminger, N. Seliger and G. Wachutka, "Reliability Model for Al Wire Bonds subjected to Heel Crack Failures”, Microelectronics Reliability 40 (2000), pp.1521-1525

[79] L. Merkle, T. Kaden, M. Sonner, A. Gademann, J. Turki, C. Dresbach, M. Petzold, “Mechanical Fatigue Properties of Heavy Aluminum Wire Bonds for Power Applications”, 2008 IEEE, 2nd Electronics System Integration Technology Conference, Greenwich, UK, pp. 1363-1368

[80] G. Khatibi, M. Lederer, B. Weiss, T. Licht, J. Bernardi, H. Danninger, “ Accelerated Mechanical Fatigue Testing and Lifetime of Interconnects in Microelectronics”, Procedia Engineering 2, Fatigue 2010, pp.511-519

[81] Jeroen Bielen, Jan-Joris Gommans, Frank Theunis, “Prediction of high cycle fatigue in aluminium bond wires: A physics of failure approach combining experiments and multi-physics simulations”, 7th International Conference on Thermal, Mechanical and Multiphysics Simulation and Experiments in Micro-Electronics and Micro-Systems, EuroSime 2006, Italy, pp. 1-7.

[82] J. M. Hu, M. Pecht, “A Probabilistic Approach for Predicting Thermal Fatigue Life of Wire Bonding in Microelectronics”, Journal of Electronic Packaging, 1991, Vol.113, pp275-285

[83] H. Lu, C. Bailey, C. Y. Yin, “Design for Reliability of Power Electronic Modules”, Microelectronics Reliability 49 (2009), pp.1250-1255

[84] M. Ciappa “Selected Failure Mechanisms of Modern Power Modules”, Microelectronics Reliability 42 (2002) pp.653-667

[85] M. Ciappa and W. Fichtner, “Lifetime Prediction of IGBT Modules for Traction Applications”, IEEE 38th Annual International Reliability Physics Symposium, San Jose, Califonia, 2000, pp.210-216

[86] J. Goehre, M. S.-R., U. Geiβler, K.-D. Lang, “Interface Degradation of Al Heavy Wire Bonds on Power Semiconductors during Active Power Cycling measured by the Shear Test”, CIPS 2010, March, 16-18, Nuremberg/Germany

[87] J. Onuki, M. Koizumi, and M. Suwa, “Reliability of Thick Al Wire Bonds in IGBT Modules for Traction Motor Drives”, IEEE Transactions on Advanced Packaging, Vol. 23, No. 1, February 2000, pp.108-112.

[88] M. Ishiko, M. Usui, T. Ohuchi, M. Shirai, “Design Concept for Wire-bonding Reliability Improvement by Optimizing Position in Power Devices”, Microelectronics Journal, Vol. 37 (2006), pp. 262-268

[89] M. Held, P. Jacob, G. Nicoletti, P. Scacco, M. H. Poech, “Fast Power Cycling Test for IGBT Modules in Traction Application”, International Journal Electronics, Vol. 86, No.10 (1999), pp. 1193-1204.

[90] U. Scheuermann, U. Hecht, “Power Cycling Lifetime of Advanced Power Modules for Different Temperature Swings”, Proc. of PCIM 2002, Nürnberg, pp.59~64

[91] R. Amro, J. Lutz, “Power Cycling with High Temperature Swing of Discrete Components based on Different Technologies”, Proc. of IEEE Power Electronics Specialists Conference 2004 (PESC’04), Aachen, Germany , pp. 2593-2598

[92] R. Amro, J. Lutz, J. Rudzki, R. Sitting, M. Thoben, “Power Cycling at High Temperature Swings of Modules with Low Temperature Joining Technique”, Proceedings of the 18th International Symposium on Power Semiconductor Devices &IC’s, June 4-8, 2006 Naples, Italy

[93] T. Matsunaga, Y. Uegai, “Thermal Fatigue Life Evaluation of Aluminium Wire Bonds”, IEEE, 2006 Electronics System Integration Technology Conference, Dresden, Germany, pp.726-732

[94] W. C. Wu, M. Held, P. Jacob, P. Scacco, A. Birolini, "Investigation on the Long Term Reliability of Power IGBT Modules", Proceedings of 1995 International Symposium on Power Semiconductor Devices & ICs, Yokohama, pp.443-448

[95] M. Glavanovics, T. Detzel, K.Weber, “Impact of thermal overload operation on wirebond and metallization reliability in smart power devices”, Solid-State Device Research conference, 2004, Proceeding of the 34th European, pp. 273-276

[96] D. O. Harris, R. A. Sire, “Fracture Mechanics Life Prediction for Microscale Components-With Application to Wire Bonding”, IEEE/IRPS 1991, PP. 35-43.

[97] K. Sasaki and N. Iwasa, “Thermal and Structural Simulation Techniques for Estimating Fatigue Life of an IGBT Module”, Proceedings of the 20th International Symposium on Power Semiconductor Devices & IC’s, May 18~22, 2008 Orlando, pp.181~184.

[98] V. Mehrotra, J. He, M. S. Dadkhah, K. Rugg, M. C. Shaw, "Wirebond Reliability in IGBT-Power Modules: Application of High Resolution Strain and Temperature Mapping", IEEE 1999, pp. 113-117.

[99] M. C. Shaw, D. B. Marshall, B. J. Dalgleish, M. S. Dadkhah, M. Y. He, and A. G. Evans, "Fatigue Crack Growth and Stress Redistribution at Interfaces", Acta. Metall. Mater., Vol. 42, 1994, pp. 4091-4099

[100] Y. Celnikier, L. Benabou, L. Dupont, G. Coquery, "Investigation of the heel crack mechanism in Al connections for power electronics modules", Microelectronics Reliability 51 (2011), pp.965-974

[101] N. Murdeshwar, J. E. Krzanowski, "A Microstructural Study of Dislocation Substructures Formed in Metal Foil Substrates during Ultrasonic Wire Bonding", Metallurgical and Materials Transactions A, Vol. 28A (1997), pp. 2663-2671

[102] G. Konig, W. Blum, "Comparison between the Cell Structures Produced in Aluminium by Cycling and by Monotonic Creep" Acta Metallurgica, Vol. 28, No.4, (1980) pp. 519-537

[103] ASTME-1049, Standard Practices for Cycle Counting in Fatigue Analysis.

[104] C.Y. Yu, P.L. Sun, P.W. Kao, C.P. Chang, "Evolution of Microstructure during Annealing of a Severely Deformed Aluminium", Materials Science and Engineering: Vol. 366, Issue 2, 15 February 2004, pp. 310–317

[105] G. Konig, W. Blum, "Comparison between the Cell Structures Produced in Aluminium by Cycling and by Monotonic Creep" Acta Metallurgica, Vol. 28, No..4 (1980), pp. 519-537

[106] C.E. Feltner, C. Laird, "Cyclic Stress-Strain Response of f.c.c. Metals and Alloys – I: Phenomenological Experiments", Acta Metallurgica, Vol.15 (1967) pp.1621-1632.

[107] C.E. Feltner, C. Laird, "Cyclic Stress-Strain Response of f.c.c. Metals and Alloys – II: Dislocation Structures and Mechanisms", Acta Metallurgica, vol.15 (1967) pp.1633-1653.

[108] L. R. Botvina, G. V. Klevtsov, Yu. S. Gladilov, "Zones of Plastic Deformation under the Surface of Impact Fracture", Problems of Strength (10) 1982, pp.55-59

[109] G. V. Klevtsov, L. R. Botvina, N. A. Klevtsova, "Plastic Zones Formation under Different Types of Loading Conditions", ISIJ International (36**)** 1996, pp.215-221

[110] J. D. Verhoeven, *Fundamentals of Physical Metallurgy*, Wiley, New York, 1975, pp. 326

[111] Y. T Cheng, C. M. Cheng, “What is indentation hardness?”, Surface Coat Technology 2000; Vol.133–134, November 2000, pp. 417–424.

[112] F. J. Humphreys, “Recrystallization and Related Annealing Phenomena” Elsevier Science Ltd, Oxford, UK, 1996.

[113] N. Q. Chinh, P. Szommera, T. Csanadi, T.G. Langdon, “Flow processes at low temperatures in ultrafine-grained aluminium”, Materials Science and Engineering, vol. A 434, pp. 326–334, 2006.

[114] J. D. Morrow, “Cyclic plastic strain energy and fatigue of metals”, in: Internal Friction, Damping, and Cyclic Plasticity, 1965, ASTM STP (378), pp.45–87

[115] R. P. Skelton, T. Vilhelmsen and G. A. Webster, “Energy criteria and cumulative damage during fatigue crack growth”, International Journal of Fatigue, Vol.20, (1998) pp.641–649

[116] I. Kim and S.-B. Lee, “Reliability and Failure Analysis of Lead-Free Solder Joints for PBGA Package Under a Cyclic Bending Load”, IEEE Transactions on Components and Packaging Technologies, Vol. 31, No. 2, June 2008, pp. 478~484

[117] M. Ciappa, M. Malberti, R. Cattomio, "A Thermomechanical Failure Mode of IGBT Multichip Modules," Proc. ESREF 95, pp. 493-499, 1995

[118] P. A. Agyakwa, M. R. Corfield, J. F. Li, “Unusual Observations in the Wear-Out of High-Purity Aluminum Wire Bonds Under Extended Range Passive Thermal Cycling”, IEEE Transactions on Device and Material Reliability, Vol.10, No.2, June 2012, pp.254-263

[119] L. Merkle, T. Kadent, M. Sonner, A. Gademannt, J. Turki, C. Oresbach, and M. Petzold, “Mechanical fatigue properties of heavy aluminium wire bonds for power applications,” in *Proc. 2nd Electron. Syst. Integr. Technol. Conf.*, Greenwich, U.K., 2008, pp. 1363–1368.

[120] J. H. Hollomon, *Trans. Metall. Soc*. AIME 162 (1945), 268-276

[121] Randall J. LeVeque, “Finite Difference Methods for Ordinary and Partial Differential Equations”, SIAM, Philadelphia, ISBN 978-0-898716-29-0, July 2007

APPENDEX A

MATLAB PROGRAMS FOR THE POSITION-DEPENDENT DAMAGE MODEL

```
clear all

clc



Definition of model parameters

w=375;l=1000;
CTEAl=23;CTESi=2.6;
dmax=(CTEAl-CTESi)*250*sqrt(l*w)*0.000001;
G0=10;
Teq=90+273;
L0=0.02;
ldx=(log(dmax)-log(L0))/19;
alphaH=20; betaH=0.5 ;betaT=3;
k2=8e7;Q=84000;R=8.31447;



Definition of temperature profiles

t=0:18:9000;     (19000)
Tmax=125;
Tmin=-55;
a=Tmax+Tmin;
b=Tmax-Tmin;
P=3600;
f=1/P;
T=a/2+(b/2)*sawtooth(2*pi*f*t+pi,0.5);
T_c=diag([T]);

TK=T+273;
TK_c=diag([TK]);
edisp=(TK-Teq)*(CTEAl-CTESi)*0.000001;      (displacement strain)



Calculation of displacement strain

dedisp(1)=0;
for j=2:501    %(1001)
    dedisp(j)=edisp(j)-edisp(j-1);
end
dedisp_c=diag([dedisp]);  % (incremental displacement strain)
```

Definition of plastic zone

```
AK(1)=1;AL(1)=0;AM(1)=0;AN(1)=0;AO(1)=0;AP(1)=0;AQ(1)=0;

for j=1:501    %(1001)
    AR(j)=0;
    AS(j)=0;
end

for j=2:501    %(1001)

    if dedisp(j)*AL(j-1)<0
        AK(j)=AK(j-1)+1;
    elseif (AL(j-1)+dedisp(j)+AM(j-1))*AL(j-1)<0 & abs(AL(j-
1)+dedisp(j)+AM(j-1))>1e-10
        AK(j)=AK(j-1);
    elseif AK(j-1)>2
        AK(j)=AK(j-1)-2;
    elseif AK(j-1)==2
        AK(j)=AK(j-1)-1;
    else AK(j)=AK(j-1);
    end

    if dedisp(j)*AL(j-1)<0
        AL(j)=dedisp(j);
    elseif (AL(j-1)+dedisp(j)+AM(j-1))*AL(j-1)<0 & abs(AL(j-
1)+dedisp(j)+AM(j-1))>1e-10
        AL(j)=AL(j-1)+dedisp(j);
    elseif AK(j-1)<=2
        AL(j)=AL(j-1)+dedisp(j);
    else AL(j)=AN(j-1);
    end

    if dedisp(j)*AL(j-1)<0
        AM(j)=AL(j-1);
    elseif (AL(j-1)+dedisp(j)+AM(j-1))*AL(j-1)<0 & abs(AL(j-
1)+dedisp(j)+AM(j-1))>1e-10
        AM(j)=AM(j-1);
    elseif AK(j-1)>2
        AM(j)=AO(j-1);
    else AM(j)=0;
    end

    if dedisp(j)*AL(j-1)<0
        AN(j)=AM(j-1);
    elseif (AL(j-1)+dedisp(j)+AM(j-1))*AL(j-1)<0 & abs(AL(j-
1)+dedisp(j)+AM(j-1))>1e-10
        AN(j)=AN(j-1);
    elseif AK(j-1)>2
        AN(j)=AP(j-1);
    else AN(j)=0;
    end

    if dedisp(j)*AL(j-1)<0
        AO(j)=AN(j-1);
    elseif (AL(j-1)+dedisp(j)+AM(j-1))*AL(j-1)<0 & abs(AL(j-
1)+dedisp(j)+AM(j-1))>1e-10
        AO(j)=AO(j-1);
```

```
    elseif AK(j-1)>2
        AO(j)=AQ(j-1);
    else AO(j)=0;
    end

    if dedisp(j)*AL(j-1)<0
        AP(j)=AO(j-1);
    elseif (AL(j-1)+dedisp(j)+AM(j-1))*AL(j-1)<0 & abs(AL(j-
1)+dedisp(j)+AM(j-1))>1e-10
        AP(j)=AP(j-1);
    elseif AK(j-1)>2
        AP(j)=AR(j-1);
    else AP(j)=0;
    end

    if dedisp(j)*AL(j-1)<0
        AQ(j)=AP(j-1);
    elseif (AL(j-1)+dedisp(j)+AM(j-1))*AL(j-1)<0 & abs(AL(j-
1)+dedisp(j)+AM(j-1))>1e-10
        AQ(j)=AQ(j-1);
    elseif AK(j-1)>2
        AQ(j)=AS(j-1);
    else AQ(j)=0;
    end

end

Plrange(1)=0;
for j=2:501   %(1001)
    Plrange(j)=sqrt(w*l)*abs(AL(j));    % plastic range
end

Plrange_c=diag([Plrange]);

for m=1:26
Lnstep(1,1)=0;Lnstep(2,2)=0;step(1,1)=0;
Lnstep(m+2,m+2)=Lnstep(m+1,m+1)+ldx;
step(m+1,m+1)=step(m,m)+L0*exp(Lnstep(m+1,m+1));

end
```

Definition of interface step length

```
for n=1:24
cell(1,1)=0.5*(step(2,2)-step(1,1));
cell(n+1,n+1)=0.5*(step(n+2,n+2)-step(n,n));
end

damage(1,24)=0;deltaL(1,24)=0;length(1,24)=0;
for i=2:501   %(1001)
 for j=1:23
  Xref(i,j)=step(j,j)+deltaL(i-1,i-1);
  for rr=1:23
   if Xref(i,j)>=step(rr,rr) & Xref(i,j)<step(rr+1,rr+1)
      found(i,j)=rr;
```

```
   end
  end
```

Calculation of position-dependent interface damage

```
frac1(i,j)=(Xref(i,j)-
step(found(i,j),found(i,j)))/(step(found(i,j)+1,found(i,j)+1)-
step(found(i,j),found(i,j)));
 Ref_damage(i,j)=damage(i-1,found(i,j))+frac1(i,j)*(damage(i-
1,found(i,j)+1)-damage(i-1,found(i,j)));
 damage(i,j)=Ref_damage(i,j)*(1-k2*exp(-
Q/R/TK_c(i,i))*30)+(Ref_damage(i,j)^0.5*20+1)*G0*exp(-
step(j,j)/(L0+Plrange_c(i,i)))*(Teq/TK_c(i,i))^3*abs(dedisp_c(i
,i));

  for pp=1:23
    if damage(i,1)<1
        deltaL(i,i)=0;
    elseif damage(i,pp)>1 & damage(i,pp+1)<1
        index(i,i)=pp;
        frac2(i,i)=(damage(i,index(i,i))-
1)/(damage(i,index(i,i))-damage(i,index(i,i)+1));

deltaL(i,i)=step(index(i,i),index(i,i))+frac2(i,i)*(step(index(
i,i)+1,index(i,i)+1)-step(index(i,i),index(i,i)));
    end
  end
  length(i,i)=length(i-1,i-1)+deltaL(i,i);
  Length=diag(length);
  damage_product(i,j)=damage(i,j)*cell(j,j);

 end
end


total_damage=sum(damage_product,2);
```

Plot

```
subplot(2,1,1),
plotyy(t,T,t,Length)
subplot(2,1,2),
plotyy(t,T,t,total_damage)

%mesh(damage)
```

APPENDEX B

MATLAB PROGRAMS FOR THE INTEGATED DAMAGE MODEL

```
clear all

clc



Definition of model parameters

w=375;l=1000;              %Define wire dimension
CTEAl=23;CTESi=2.6;
G0=10;
Teq=90+273;
L0=0.02;
alphaH=20; betaH=0.5; betaT=3;
k2=3e7;Q=84000;R=8.31447;



Definition of temperature profiles



t=0:18:172782;             % (17262)

Tmax=125;
Tmin=-55;
P=3600;                    %cycling time
f=1/P;                     %frequency

a=Tmax+Tmin;
b=Tmax-Tmin;

T=a/2+(b/2)*sawtooth(2*pi*f*t+pi,0.5);



Calculation of displacement strain

TK=T+273;

edisp=(TK-Teq)*(CTEAl-CTESi)*0.000001;      (displacement strain)

dedisp(1)=0;
for j=2:9600
    dedisp(j)=edisp(j)-edisp(j-1);
                                        (incremental displacement strain)
end
```

Definition of plastic zone

```
AK(1)=1;AL(1)=0;AM(1)=0;AN(1)=0;AO(1)=0;AP(1)=0;AQ(1)=0;

for j=1:9600
    AR(j)=0;
    AS(j)=0;
end

for j=2:9600

    if dedisp(j)*AL(j-1)<0
        AK(j)=AK(j-1)+1;
    elseif (AL(j-1)+dedisp(j)+AM(j-1))*AL(j-1)<0 & abs(AL(j-
1)+dedisp(j)+AM(j-1))>1e-10
        AK(j)=AK(j-1);
    elseif AK(j-1)>2
        AK(j)=AK(j-1)-2;
    elseif AK(j-1)==2
        AK(j)=AK(j-1)-1;
    else AK(j)=AK(j-1);
    end

    if dedisp(j)*AL(j-1)<0
        AL(j)=dedisp(j);
    elseif (AL(j-1)+dedisp(j)+AM(j-1))*AL(j-1)<0 & abs(AL(j-
1)+dedisp(j)+AM(j-1))>1e-10
        AL(j)=AL(j-1)+dedisp(j);
    elseif AK(j-1)<=2
        AL(j)=AL(j-1)+dedisp(j);
    else AL(j)=AN(j-1);
    end

    if dedisp(j)*AL(j-1)<0
        AM(j)=AL(j-1);
    elseif (AL(j-1)+dedisp(j)+AM(j-1))*AL(j-1)<0 & abs(AL(j-
1)+dedisp(j)+AM(j-1))>1e-10
        AM(j)=AM(j-1);
    elseif AK(j-1)>2
        AM(j)=AO(j-1);
    else AM(j)=0;
    end

    if dedisp(j)*AL(j-1)<0
        AN(j)=AM(j-1);
    elseif (AL(j-1)+dedisp(j)+AM(j-1))*AL(j-1)<0 & abs(AL(j-
1)+dedisp(j)+AM(j-1))>1e-10
        AN(j)=AN(j-1);
    elseif AK(j-1)>2
        AN(j)=AP(j-1);
    else AN(j)=0;
    end

    if dedisp(j)*AL(j-1)<0
        AO(j)=AN(j-1);
    elseif (AL(j-1)+dedisp(j)+AM(j-1))*AL(j-1)<0 & abs(AL(j-
1)+dedisp(j)+AM(j-1))>1e-10
        AO(j)=AO(j-1);
```

```
    elseif AK(j-1)>2
        AO(j)=AQ(j-1);
    else AO(j)=0;
    end

    if dedisp(j)*AL(j-1)<0
        AP(j)=AO(j-1);
    elseif (AL(j-1)+dedisp(j)+AM(j-1))*AL(j-1)<0 & abs(AL(j-
1)+dedisp(j)+AM(j-1))>1e-10
        AP(j)=AP(j-1);
    elseif AK(j-1)>2
        AP(j)=AR(j-1);
    else AP(j)=0;
    end

    if dedisp(j)*AL(j-1)<0
        AQ(j)=AP(j-1);
    elseif (AL(j-1)+dedisp(j)+AM(j-1))*AL(j-1)<0 & abs(AL(j-
1)+dedisp(j)+AM(j-1))>1e-10
        AQ(j)=AQ(j-1);
    elseif AK(j-1)>2
        AQ(j)=AS(j-1);
    else AQ(j)=0;
    end

end

Plrange(1)=0;
for j=2:9600
    Plrange(j)=sqrt(w*l)*abs(AL(j));    %plastic range
end


Dth=1;
damage(1)=0;deltaL(1)=0;Length(1)=0;F0=2000;Fs(1)=F0;




Calculation of total interface damage


for i=2:9600

 damage(i)=damage(i-1)*(1-k2*exp(-Q/R/TK(i))*18)+(damage(i-
1)^betaH*alphaH+1)*G0*(L0+Plrange(i))*(1-exp(-
4))*(Teq/TK(i))^betaT*abs(dedisp(i))-0.5*deltaL(i-1)*damage(i-
1);                                                  %Total damage

 if damage(i)<Dth
 deltaL(i)=0;
 else deltaL(i)=0.00001*damage(i)*18+0.000001*(damage(i)-
damage(i-1));
end

Length(i)=Length(i-1)+deltaL(i);                  %crack length
```

```
Fs(i)=F0*(1-Length(i)/l);                          %shear force
 end


%wear_out_rate=-(1-Fs(9600)/F0)/172782;  %per second

wear_out_rate=-(1-Fs(9600)/F0)/(172782/P);  %per cycle


Plot figures

subplot(2,1,1),plot(t,T)
grid on
xlabel('Time(s)')
ylabel('Temperature')
subplot(2,1,2),plot(t,damage)
grid on
xlabel('Time(s)')
ylabel('Damage')



%subplot(2,1,1)
%plotyy(t,T,t,Length)
%[AX,H1,H2]=plotyy(t,T,t,Length);
%set(get(AX(1),'ylabel'),'string','Temperature')
%set(get(AX(2),'ylabel'),'string','Crack Length')
%xlabel('Time (s)')

%subplot(2,1,2)
%plotyy(t,T,t,damage)
%[AX,H1,H2]=plotyy(t,T,t,damage);
%set(get(AX(1),'ylabel'),'string','Temperature')
%set(get(AX(2),'ylabel'),'string','Damage')
%xlabel('Time (s)')
```

APPENDEX C

DEFINITIONS OF TEMPERATUR PROFILES

For the damage model, temperature profile is an important input representing different loading conditions to which the power modules are subjected. In this section, the MATLAB programs are provided to shape various temperature profiles in terms of with or without dwelling time at temperature extremes, and define these profiles in different ways such as fixing cycling time or fixing heating/cooling rate.

Given cycling time

(1) without dwells

```
t=0:18:172782;

Tmax=125;
Tmin=-55;
t_p=3600;                    %cycling time
f=1/t_p;                     %frequency

a=Tmax+Tmin;
b=Tmax-Tmin;

T=a/2+(b/2)*sawtooth(2*pi*f*t+pi,0.5);      Temperature profile
```

(2) with dwells

```
t=0:18:172782;

Tmax_tg=125;            %peak temperature at dwells
Tmin_tg=-55;
t_p=3600;                 %cycling time
f=1/t_p;                  %frequency
t_dw=300;               %dwelling time

%peak temperatures for the corresponding sawtooth function
%dwell at both maximum and minimum peak temperature
Tmax=((t_p-t_dw)*Tmax_tg-t_dw*Tmin_tg)/(t_p-2*t_dw);
Tmin=((t_p-t_dw)*Tmin_tg-t_dw*Tmax_tg)/(t_p-2*t_dw);
```

```
%dwell only at maximum peak temperature
%Tmax=(t_p*Tmax_tg-t_dw*Tmin_tg)/(t_p-t_dw);
%Tmin=Tmin_tg;

a=Tmax+Tmin;
b=Tmax-Tmin;

T_base=a/2+(b/2)*sawtooth(2*pi*f*t+pi,0.5);  %sawtooth function


%Trapezoid temperature profile
for i=1:9600
if T_base(i)>Tmax_tg
    T(i)=Tmax_tg;

elseif T_base(i)<Tmin_tg
    T(i)=Tmin_tg;

else T(i)=T_base(i);

end
end
```

Given ramp rate

(1) without dwells

```
t=0:18:172782;

Tmax=125;
Tmin=-55;
ramp_rate=1/10;                    %(degree per second)
P=2*(Tmax-Tmin_tg)/ramp_rate;     %period of a cycle
f=1/P;                             %frequency

a=Tmax+Tmin;
b=Tmax-Tmin;

T=a/2+(b/2)*sawtooth(2*pi*f*t+pi,0.5);      Temperature profile
```

(2) with dwells

```
t=0:18:172782;

Tmax_tg=125;           %peak temperature at dwells
Tmin_tg=-55;

t_dw=750;                          %dwelling time
ramp_rate=1/10;                    %(degree per second)


%peak temperatures for the corresponding sawtooth function
%dwell only at maximum peak temperature
t_p=2*(Tmax-Tmin_tg)/ramp_rate+t_dw;    %period of a cycle
```

```
f=1/t_p;                                    %frequency
%Tmax=(t_p*Tmax_tg-t_dw*Tmin_tg)/(t_p-t_dw);
%Tmin=Tmin_tg;

%dwell at both maximum and minimum peak temperature

t_p=2*(Tmax-Tmin_tg)/ramp_rate+2*t_dw;    %period of a cycle
f=1/t_p;                                    %frequency

Tmax=((t_p-t_dw)*Tmax_tg-t_dw*Tmin_tg)/(t_p-2*t_dw);
Tmin=((t_p-t_dw)*Tmin_tg-t_dw*Tmax_tg)/(t_p-2*t_dw);


a=Tmax+Tmin;
b=Tmax-Tmin;

T_base=a/2+(b/2)*sawtooth(2*pi*f*t+pi,0.5);  %sawtooth function


%Trapezoid temperature profile
for i=1:9600
if T_base(i)>Tmax_tg
    T(i)=Tmax_tg;

elseif T_base(i)<Tmin_tg
    T(i)=Tmin_tg;

else T(i)=T_base(i);

end
end
```

APPENDEX D

EXPERIMENTAL SETUP FOR ACCELERATED PASSIVE THERMAL CYCLING TEST

Environment chamber

Inside the chamber

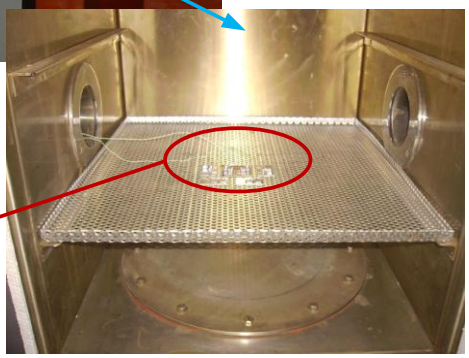

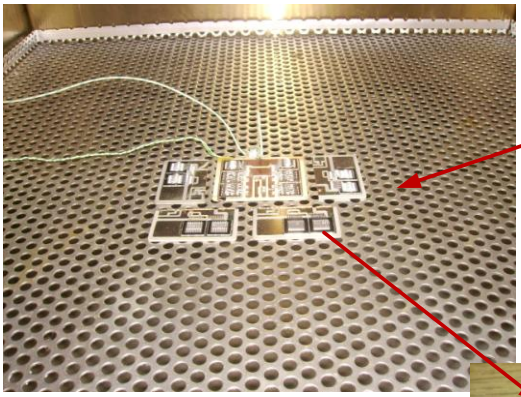

The samples are located in the middle of the chamber

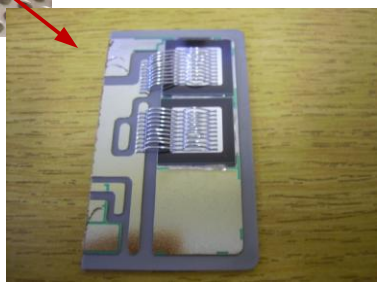

Tested samples (half substrate)